TIME-AVERAGED MODEL FOR LONGSHORE CURRENT AND SEDIMENT TRANSPORT IN THE SURF AND SWASH ZONES

by

Arpit Agarwal

A thesis submitted to the Faculty of the University of Delaware in partial fulfillment of the requirements for the degree of Master of Civil Engineering

Summer 2005

© 2005 Arpit Agarwal
All Rights Reserved

UMI Number: 1428092

UMI®

UMI Microform 1428092

Copyright 2005 by ProQuest Information and Learning Company.
All rights reserved. This microform edition is protected against
unauthorized copying under Title 17, United States Code.

ProQuest Information and Learning Company
300 North Zeeb Road
P.O. Box 1346
Ann Arbor, MI 48106-1346

TIME-AVERAGED MODEL FOR LONGSHORE CURRENT AND SEDIMENT TRANSPORT IN THE SURF AND SWASH ZONES

by

Arpit Agarwal

Approved: _____
Nobuhisa Kobayashi, Ph.D.
Professor in charge of thesis

Approved: _____
Michael J. Chajes, Ph.D.
Chair of the Department of Civil and Environmental Engineering

Approved: _____
Eric W. Kaler, Ph.D.
Dean of the College of Engineering

Approved: _____
Conrado M. Gempesaw II, Ph.D.
Vice Provost for Academic and International Programs

ACKNOWLEDGEMENTS

It is my great pleasure to express my sense of gratitude and indebtness towards Dr.Nobuhisa Kobayashi, my advisor without whose help and able guidance this thesis would have never been completed. His ever accommodating nature, ready to meet and hear doubts whenever I went to him, helped me to work on this research work at a smooth pace. It was my cherished privilege to work under him.

I would also like to express my unfeigned gratitude to Entin Karjadi for providing me the field data files and to Bradley Johnson and Ernest Smith for providing the extensive laboratory data and by promptly answering any doubts that I had regarding the laboratory datasets.

I would like to thank the National Oceanic and Atmospheric Administration as this study was supported by the National Oceanic and Atmospheric Administration Office of Sea Grant, Department of Commerce, under Grant No. NA85AA-D-SG033 (Projects R/OE-33 and R/ETE-7).

This is indeed devoid of gist, if I do not mention my friends Shubhra, Wenting and Manika who introduced me to the fantastic world of LaTeX, Lizbeth and Paco who cleared my doubts regarding the plotting of figures and Rosalie for all her help.

This thesis is dedicated to my parents who have always stood by me in all the ups and downs of my life and have always encouraged and supported me to achieve the best.

TABLE OF CONTENTS

LIST OF FIGURES . . . . . **v**
LIST OF TABLES . . . . . **x**
ABSTRACT . . . . . **xi**

Chapter

1 INTRODUCTION **1**
2 TIME-AVERAGED NUMERICAL MODEL **4**

2.1 Governing Equations 5
2.2 Finite Difference Method 11

3 COMPARISONS WITH FIELD DATA **13**

3.1 Comparisons with February 5 Data 14
3.2 Comparisons with February 6 Data 24

4 COMPARISONS WITH LABORATORY DATA **29**

4.1 Spilling Wave Data Analysis 31
4.2 Plunging Wave Data Analysis 46
4.3 Comparisons with Spilling Wave Data 56
4.4 Comparisons with Plunging Wave Data 72

5 LONGSHORE SUSPENDED SEDIMENT TRANSPORT RATE 86
6 CONCLUSIONS **91**
REFERENCES **93**

LIST OF FIGURES

2.1 Obliquely incident irregular waves on a straight shoreline. 4

3.1 Measured and computed (by time-dependent model RBREAK and time-averaged model with IROLL = 0 and 1) cross-shore variations of the mean $\bar{\eta}$ and standard deviation σ_η of the free surface elevation above the bottom profile z_b on February 5. 15

3.2 Computed dimensionless function G_{by}, longshore radiation stress $S_{xy} = \rho g S^*_{xy}$ and bottom shear stress $\tau_{by} = \rho g \tau^*_{by}$ for February 5. . . 17

3.3 Dimensionless function G_{by} calculated by Eq. 2.34 and by approximate expression $1.16V^*$ where $V^* = \overline{V}/\sigma_T$ for IROLL = 0 (top) and 1 (bottom) for February 5. 18

3.4 Computed cross-shore energy flux $F_x = \rho g F^*_x$, and energy dissipation rates $D_B = \rho g D^*_B$ and $D_f = \rho g D^*_f$ due to wave breaking and bottom friction for the time dependent and time-averaged models for February 5. 19

3.5 Computed turbulent velocity u'_f for the time-averaged model and the sediment fall velocity w_f of fine sand for February 5 20

3.6 Computed mean and standard deviation of U for the time-averaged and time-dependent models for February 5 21

3.7 Measured and computed (time dependent and time-averaged) cross-shore variations of longshore current $\overline{V}$ for February 5 22

3.8 Computed standard deviation of V and $\sin\theta$ for the time-averaged model for February 5. 23

3.9 Measured and computed (by time-dependent model RBREAK and time-averaged model with IROLL = 0 and 1) cross-shore variations of the standard deviation σ_η of the free surface elevation and the computed wave setup $\bar{\eta}$ from time-averaged model above the bottom profile z_b for February 6. 25

3.10 Measured and computed (time dependent and time-averaged) cross-shore variations of longshore current $\overline{V}$ for February 6. 26

3.11 Computed cross-shore energy flux $F_x = \rho g F_x^*$, and energy dissipation rates $D_B = \rho g D_B^*$ and $D_f = \rho g D_f^*$ due to wave breaking and bottom friction for the time-averaged model for February 6. . . 27

3.12 Computed dimensionless function G_{by}, longshore radiation stress $S_{xy} = \rho g S_{xy}^*$ and bottom shear stress $\tau_{by} = \rho g \tau_{by}^*$ for the time-averaged model for February 6. 28

4.1 Measured and smoothed bathymetric profiles and the cross-shore variation of deviations between them for the spilling wave test . . . 32

4.2 Measured and fitted parabolic profiles of mean $\overline{u}$ for spilling wave test 35

4.3 Measured and vertically averaged values of σ_u for spilling wave test 36

4.4 Measured and fitted logarithmic profiles of mean $\overline{v}$ for spilling wave test 38

4.5 Measured and vertically averaged values of σ_v for spilling wave test 39

4.6 Measured and fitted power-form and exponential profiles of mean concentration $\bar{c}$ for spilling wave test 44

4.7 Measured and vertically averaged values of $\sigma_c/\bar{c}$ for spilling wave test 45

4.8 Measured and smoothed bathymetric profiles and the cross-shore variation of deviations between them for the plunging wave test . . 49

4.9 Measured and fitted parabolic profiles of mean $\overline{u}$ for plunging wave test. 50

4.10 Measured and vertically averaged values of σ_u for plunging wave test. 51

4.11 Measured and fitted logarithmic profiles of mean $\overline{v}$ for plunging wave test. 52

4.12 Measured and vertically averaged values of σ_v for plunging wave test. 53

4.13 Measured and fitted power-form and exponential profiles of mean concentration $\bar{c}$ for plunging wave test. 54

4.14 Measured and vertically averaged values of $\sigma_c/\bar{c}$ for plunging wave test. 55

4.15 Measured and computed mean and standard deviation of η above bottom profile z_b for spilling wave test. 57

4.16 Number of iterations for computations with (IROLL = 1) and without roller (IROLL = 0) for spilling wave test. 58

4.17 Computed cross-shore variations of n, Q, σ_* and a for spilling wave test. 59

4.18 Computed roller volume flux q_r and roller slope β_r for IROLL = 1. 60

4.19 Computed cross-shore radiation stress $S_{xx} = \rho g S^*_{xx}$ and bottom shear stress $\tau_{bx} = \rho g \tau^*_{bx}$ for spilling wave test. 62

4.20 Measured and computed mean and standard deviation of U for spilling wave test. 63

4.21 Computed dimensionless function G_{by}, longshore radiation stress $S_{xy} = \rho g S^*_{sy}$ and bottom shear stress $\tau_{by} = \rho g \tau^*_{by}$. 64

4.22 Dimensionless function G_{by} calculted by Eq. 2.34 and by approximate expression $1.16V^*$ where $V^* = \overline{V}/\sigma_T$ for IROLL = 0 (top) and 1 (bottom) for spilling wave test. 65

4.23 Measured and computed longshore current $\overline{V}$ for spilling wave test. 66

4.24 Measured and computed standard deviation of V as well as computed $\sin\theta$ for spilling wave test. 67

4.25 Computed cross-shore energy flux $F_x = \rho g F_x^*$, and energy dissipation rates $D_B = \rho g D_B^*$ and $D_f = \rho g D_f^*$ due to wave breaking and bottom friction for spilling wave test. 69

4.26 Computed turbulent velocity u_f' and estimated sediment fall velocity w_f for spilling wave test. 70

4.27 Measured and computed suspended sediment volume $\overline{V_c}$ per unit horizontal area for spilling wave test. 71

4.28 Measured and computed offshore suspended sediment transport rate q_{off} due to offshore current for spilling wave test. 71

4.29 Measured and computed mean and standard deviation of η above bottom profile z_b for plunging wave test. 73

4.30 Computed cross-shore variations of n, Q, σ_* and a for plunging wave test. 74

4.31 Computed roller volume flux q_r and roller slope β_r for IROLL = 1 for plunging wave test. 75

4.32 Computed cross-shore radiation stress $S_{xx} = \rho g S_{xx}^*$ and bottom shear stress $\tau_{bx} = \rho g \tau_{bx}^*$ for plunging wave test. 76

4.33 Measured and computed mean and standard deviation of U for plunging wave test. 78

4.34 Computed dimensionless function G_{by}, longshore radiation stress $S_{xy} = \rho g S_{sy}^*$ and bottom shear stress $\tau_{by} = \rho g \tau_{by}^*$ for plunging wave test. 79

4.35 Dimensionless function G_{by} calculated by Eq. 2.34 and by approximate expression $1.16V^*$ where $V^* = \bar{V}/\sigma_T$ for IROLL = 0 (top) and 1 (bottom) for plunging wave test. 80

4.36 Measured and computed longshore current $\overline{V}$ for plunging wave test. 81

4.37 Measured and computed standard deviation of V as well as computed $\sin\theta$ for plunging wave test. 81

4.38 Computed cross-shore energy flux $F_x = \rho g F_x^*$, and energy dissipation rates $D_B = \rho g D_B^*$ and $D_f = \rho g D_f^*$ due to wave breaking and bottom friction for plunging wave test. 83

4.39 Computed turbulent velocity u_f' and estimated sediment fall velocity w_f for plunging wave test. 84

4.40 Measured and computed suspended sediment volume $\overline{V_c}$ per unit horizontal area for plunging wave test. 85

4.41 Measured and computed offshore suspended sediment transport rate q_{off} due to offshore current for plunging wave test. 85

5.1 Computed and approximate suspended sediment transport rate q_s in comparison with measured longshore suspended ($q_{\ell s}$) and trapped ($q_{\ell t}$) sediment transport rates for IROLL = 0 (top) and 1 (bottom) for spilling wave test. 89

5.2 Computed and approximate suspended sediment transport rate q_s in comparison with measured longshore suspended ($q_{\ell s}$) and trapped ($q_{\ell t}$) sediment transport rates for IROLL = 0 (top) and 1 (bottom) for plunging wave test. 90

LIST OF TABLES

3.1 Wave Conditions at Seaward Boundary for February 5 and 6 Data . 13

4.1 Wave Conditions at Seaward Boundary for Spilling and Plunging Wave Tests 30

4.2 Measured Depth and Free Surface Data for Spilling Wave Test . . . 33

4.3 Cross-shore Velocity Data for Spilling Wave Test 37

4.4 Longshore Velocity Data for Spilling Wave Test 40

4.5 Fitted Exponential and Power-Form Profiles for $\bar{c}$ for Spilling Wave Test 41

4.6 Measured Volume, Offshore and Longshore Transport Rates of Suspended Sediment for Spilling Wave Test 43

4.7 Measured Depth and Free Surface Data for Plunging Wave Test . . 46

4.8 Cross-shore Velocity Data for Plunging Wave Test 47

4.9 Longshore Velocity Data for Plunging Wave Test 48

4.10 Fitted Exponential and Power-Form Profiles for $\bar{c}$ for Plunging Wave Test 48

4.11 Measured Volume, Offshore and Longshore Transport Rates of Suspended Sediment for Plunging Wave Test 49

5.1 Total Sediment Transport Rates $Q_{\ell t}$ and Q_s for Spilling and Plunging Wave Tests 87

ABSTRACT

A numerical model based on the time-averaged continuity, cross-shore momentum, longshore momentum and energy equations for the case of longshore uniformity is developed to predict the cross-shore variations of the mean and standard deviation of the free surface elevation and depth-averaged cross-shore and longshore velocities under obliquely-incident irregular breaking waves. Iterative finite-difference approximations are used to solve these governing equations. The suspended sediment volume per unit horizontal area is estimated using the computed energy dissipation rates due to wave breaking and bottom friction. The longshore suspended sediment transport rate is estimated as the product of the longshore current and suspended sediment volume. The developed model is compared with available field data and with the time-dependent model of Kobayashi and Karjadi (1996). The model is also compared with the laboratory data for spilling and plunging breaker tests after analyzing the extensive measured data to get meaningful results for comparison. The calibrated model is in fair agreement with the data except that this time-averaged model cannot predict wave runup, low frequency waves, shear waves and bed load. The longshore suspended sediment transport rate is shown to be approximately proportional to the square of the longshore current. The developed model is computationally very efficient and well suited for future comparisons with extensive data sets.

Chapter 1

INTRODUCTION

A quantitative understanding of longshore sediment transport in surf and swash zones on beaches under obliquely incident waves is essential for the design of shoreline erosion mitigation measures such as beach nourishment and sand bypassing. A large number of empirical formulas including the CERC formula (*Coastal Engineering Manual* 2002) have been proposed for predicting the total longshore sediment transport rate over the entire surf and swash zones as a function of the breaking wave characteristics, beach slope and sediment diameter. Some of the formulas have been refined and may predict the total sediment transport rate within a factor of about two (Kamphuis 2002; van Rijn 2002). For practical applications in the US, the CERC formula is normally calibrated for each project site. This engineering practice may be prudent but requires time and expense. Moreover, the performance of a project will need to be monitored because the formula calibrated for field conditions before the project may need to be recalibrated after the project.

Field and laboratory measurements on the distribution of longshore sediment transport across the surf and swash zones (Bodge and Dean 1987; Wang 1998; Miller 1999; Wang et al. 2002a) indicated several distribution patterns depending on nearshore morphology (barred and plane beaches) and breaker type. The longshore sediment transport rate in the swash zone was found to contribute significantly to the total transport rate when incident waves collapsed on the foreshore. Wang (1998) evaluated available formulas for predicting the local longshore sediment transport

rate as a function of the cross-shore distance. The accuracy of these formulas is similar to the accuracy of the simpler CERC formula for the total transport rate. Consequently, use is rarely made of the cross-shore integration of the predicted local transport rate to estimate the total transport rate for practical applications. However, the local longshore sediment transport rate may be predicted more accurately now owing to the fairly accurate prediction of longshore currents on natural beaches (Ruessink el al. 2001).

Time-dependent numerical models such as those based on the finite-amplitude shallow-water equations have been shown to be capable of predicting surf and swash zone dynamics on beaches (Kobayashi et al. 1989; Kobayashi and Wurjanto 1992; Raubenheimer et al. 1995; Raubenheimer and Guza 1996). However, time-dependent numerical models require considerable computation time to resolve the wave profiles varying in time and space. The time-averaged models for random waves represented by the root-mean-square wave height (Battjes and Janssen 1978; Thornton and Guza 1983) or expressed as the superposition of regular waves [e.g., Dally (1992)] are much more efficient computationally but may considerably underpredict the wave setup and root-mean-square wave height near the still waterline (Cox et al. 1994).

The relatively simple numerical model by Ruessink et al. (2001) is extended here to the lower swash zone and coupled with the cross-shore suspended sediment transport model by Kobayashi et al. (2005). This extended model is based on the time-averaged continuity, cross-shore momentum, longshore momentum, and energy equations. The model predicts the cross-shore variations of the mean and standard deviation of the free surface elevation and depth-averaged cross-shore and longshore fluid velocities as well as the time-averaged suspended sediment volume per unit horizontal area. This time-averaged model is compared with the time-dependent model of Kobayashi and Karjadi (1996) who compared their model with

field data. Both models yield similar agreement with the measured longshore current and wave height. The time-averaged model extends only to the lower swash zone unlike the time-dependent model which can predict irregular wave runup. Since the field data was limited to just longshore current and standard deviation of the free surface elevation, the time-averaged model is also compared with the comprehensive laboratory data of the spilling and plunging wave tests by Wang et al. (2002a) after analyzing the measured time series data of the free surface, cross-shore and longshore velocities and suspended sediment concentration along with the measured bathymetry data.

In the following, the time-averaged model is presented first in Chapter 2 with the explanation of governing equations used and also the finite difference scheme that is employed to solve the governing equations. In Chapter 3 comparisons with the time-dependent model and field data are shown concisely as limited data was available for comparison with the time-averaged numerical model. The more detailed assessment of the time-averaged model using the comprehensive laboratory data is presented in Chapter 4. This chapter first discusses the nature of data that was available for analysis, then describes how the data was analyzed to get meaningful results which were used for subsequent comparison with the time-averaged model for both the spilling and plunging wave tests. Chapter 5 explains the approximate formulas developed for calculating the longshore suspended sediment transport rate. Finally, the findings of this study are summarized in Chapter 6.

Chapter 2

TIME-AVERAGED NUMERICAL MODEL

The time-averaged model developed here is an extension of the Dutch models by Battjes and Stive (1985), Reniers and Battjes (1997), and Ruessink et al. (2001). Fig. 2.1 shows obliquely incident irregular waves on a straight shoreline where the cross-shore coordinate x is positive onshore and the longshore coordinate y is positive in the downwave direction.

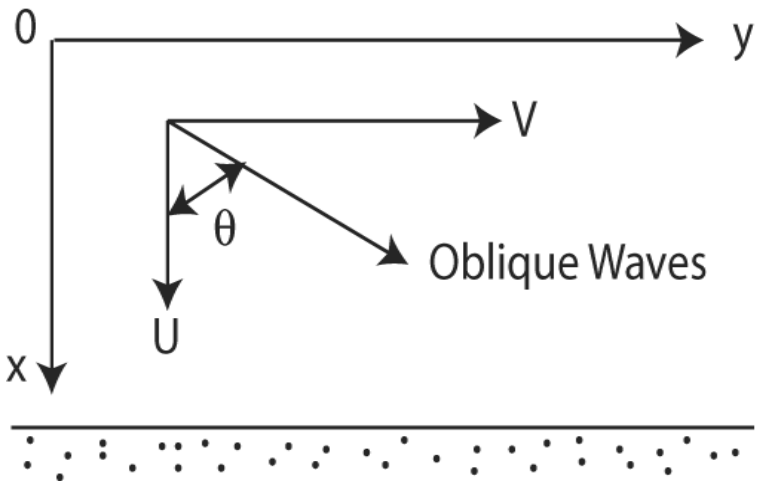

Figure 2.1: Obliquely incident irregular waves on a straight shoreline.

The depth-averaged cross-shore and longshore velocities are denoted by U and V, respectively. Incident waves are assumed to be unidirectional with $\theta =$ incident angle and uniform in the longshore direction.

2.1 Governing Equations

The time-averaged cross-shore momentum, longshore momentum and energy equations for the case of longshore uniformity are expressed as

$$\frac{dS_{xx}}{dx} = -\rho g \bar{h} \frac{d\bar{\eta}}{dx} - \tau_{bx} \tag{2.1}$$

$$\frac{dS_{xy}}{dx} = -\tau_{by} \tag{2.2}$$

$$\frac{dF_x}{dx} = -D_B - D_f \tag{2.3}$$

where S_{xx} = cross-shore radiation stress; ρ = fluid density; g = gravitational acceleration; $\bar{h}$ = mean water depth given by $\bar{h} = (\bar{\eta} - z_b)$ with $\bar{\eta}$ = mean free surface elevation and z_b = bottom elevation; τ_{bx} = cross-shore bottom stress; S_{xy} = longshore radiation stress; τ_{by} = longshore bottom stress; F_x = cross-shore energy flux; and D_B and D_f = energy dissipation rates due to wave breaking and bottom friction, respectively. The terms τ_{bx} in Eq. (2.1) and D_f in Eq. (2.3) are normally neglected but are included here because of the importance of bottom friction for sediment transport.

Linear wave theory for onshore progressive waves is used to estimate S_{xx}, S_{xy} and F_x

$$S_{xx} = (En + E_r)\cos^2\theta + E\left(n - \frac{1}{2}\right) \tag{2.4}$$

$$S_{xy} = (En + E_r)\cos\theta\sin\theta \tag{2.5}$$

$$F_x = EC_g\cos\theta \tag{2.6}$$

with

$$E = \rho g \sigma_\eta^2 \tag{2.7}$$

$$n = C_g/C_p \tag{2.8}$$

$$\sin\theta/C_p = \alpha \tag{2.9}$$

$$E_r = \rho C_p q_r \tag{2.10}$$

where E = specific wave energy; σ_η = standard deviation of the free surface elevation η related to the root-mean-square wave height $H_{\rm rms}$ as $H_{\rm rms} = \sqrt{8}\sigma_\eta$; C_g and C_p = group velocity and phase velocity, respectively, in the mean water depth $\bar{h}$ corresponding to the spectral peak period T_p; α = constant in the region $x \geq 0$ based on Snell's law; and q_r and E_r = volume and momentum fluxes of a roller propagating with the speed C_p. The roller effect has been represented by its area or energy (Svendsen 1984) but the roller volume flux has been used by Kobayashi et al. (2005) who have found that the roller effect is most apparent in the increase of undertow current for normally incident waves. The energy equation for the roller may be expressed as (Ruessink et al. 2001)

$$\frac{d}{dx}\left(\rho C_p^2 q_r \cos\theta\right) = D_B - D_r \tag{2.11}$$

with

$$D_r = \rho g \beta_r q_r \tag{2.12}$$

where the roller dissipation rate D_r is assumed to be equal to the rate of work done to maintain the roller on the wave-front slope β_r of the order of 0.1.

The time-averaged bottom shear stresses and the energy dissipation rate due to bottom friction are expressed as

$$\tau_{bx} = \frac{1}{2}\rho f_b \overline{U U_a} \tag{2.13}$$

$$\tau_{by} = \frac{1}{2}\rho f_b \overline{V U_a} \tag{2.14}$$

$$D_f = \frac{1}{2}\rho f_b \overline{U_a^3} \tag{2.15}$$

with

$$U_a = \left(U^2 + V^2\right)^{0.5} \tag{2.16}$$

where f_b = bottom friction factor; and the overbar indicates time averaging. Linear shallow-water wave theory has been used to find the approximate local relationships between the free surface elevation and the horizontal velocity in the direction of

wave propagation [e.g., Kobayashi et al. (1998)]. The velocities U and V in Eqs. (2.13)–(2.16) are assumed to be expressed as

$$U = \overline{U} + U_T \cos\theta \tag{2.17}$$

$$V = \overline{V} + U_T \sin\theta \tag{2.18}$$

$$U_T = \left(g/\bar{h}\right)^{0.5} (\eta - \bar{\eta}) \tag{2.19}$$

where $\overline{U}$ and $\overline{V}$ = depth-averaged cross-shore and longshore currents; and U_T = oscillatory horizontal velocity with zero mean. Eq. (2.17)–(2.19) yields

$$\sigma_U = \sigma_T \cos\theta \tag{2.20}$$

$$\sigma_V = \sigma_T \sin\theta \tag{2.21}$$

$$\sigma_T = \left(g\bar{h}\right)^{0.5} \sigma_* \tag{2.22}$$

with

$$\sigma_* = \sigma_\eta / \bar{h} \tag{2.23}$$

where σ_U, σ_V and σ_T = standard deviations of U, V and U_T, respectively.

Assuming the equivalency of the time and probabilistic averaging as well as the Gaussian distribution of U_T, Eqs. (2.13)–(2.15) are approximated as

$$\tau_{bx} = \frac{1}{2}\rho f_b \sigma_T^2 G_{bx} \tag{2.24}$$

$$\tau_{by} = \frac{1}{2}\rho f_b \sigma_T^2 G_{by} \tag{2.25}$$

$$D_f = \frac{1}{2}\rho f_b \sigma_T^3 G_f \tag{2.26}$$

with

$$G_{bx} = \int_{-\infty}^{\infty} F_U F_a f(r) dr \tag{2.27}$$

$$G_{by} = \int_{-\infty}^{\infty} F_V F_a f(r) dr \tag{2.28}$$

$$G_f = \int_{-\infty}^{\infty} F_a^3 f(r) dr \tag{2.29}$$

$$F_U = \frac{\overline{U}}{\sigma_T} + r\cos\theta \tag{2.30}$$

$$F_V = \frac{\overline{V}}{\sigma_T} + r\sin\theta \tag{2.31}$$

$$F_a = (F_U^2 + F_V^2)^{0.5} \tag{2.32}$$

$$f(r) = \frac{1}{\sqrt{2\pi}} \exp\left(-\frac{r^2}{2}\right) \tag{2.33}$$

where the mean and standard deviation of the Gaussian variable $r = U_T/\sigma_T$ is zero and unity, respectively. The numerical integration with respect to r in Eqs. (2.27)–(2.29) is performed in the range of $-5 < r < 5$ where $f(r) = 1.5 \times 10^{-6}$ for $r^2 = 25$.

The longshore momentum equation, Eq. (2.2), is used to obtain the value of G_{by} and the corresponding longshore current $\overline{V}$ using a bisection method (Press et al. 1989). It is more efficient computationally to adopt the following explicit relationship between G_{by} and $\overline{V}$ obtained by Feddersen et al. (2000) using field data and probabilistic analysis:

$$G_{by} = \frac{\overline{V}}{\sigma_T}\left[1.16^2 + \left(\frac{\overline{V}}{\sigma_T}\right)^2\right]^{0.5} \tag{2.34}$$

The difference between the values of G_{by} computed using Eqs. (2.28) and (2.34) is less than about 20% for the computations made in this study. This difference is less than the uncertainty of the bottom friction factor f_b. As a result, Eq. (2.34) is adopted in the following. On the other hand, the cross-shore momentum equation, Eq. (2.1), and the energy equation, Eq. (2.3), can be solved numerically without difficulties [e.g., Kobayashi and Johnson (1998)] to obtain $\bar{\eta}$ and σ_η. The depth-integrated continuity equation of water on the beach, which is assumed impermeable, is expressed as $(\overline{hU} + q_r\cos\theta) = 0$ with $h = (\eta - z_b)$. Using Eqs. (2.17)–(2.23), the

continuity equation yields

$$\overline{U} = -\sigma_U \sigma_* \left(1 + \sqrt{\frac{\bar{h}}{g} \frac{q_r}{\sigma_\eta^2}} \right) \tag{2.35}$$

The energy dissipation rate D_B due to wave breaking in Eq. (2.3) is estimated using the formula by Battjes and Stive (1985)

$$D_B = \frac{\rho g a Q H_B^2}{4 T_p} \tag{2.36}$$

with

$$\frac{Q-1}{\ln Q} = \left(\frac{H_{\rm rms}}{H_m} \right)^2 \tag{2.37}$$

$$H_m = \frac{0.88}{k_p} \tanh \left(\frac{\gamma k_p \bar{h}}{0.88} \right) \tag{2.38}$$

where a = empirical coefficient suggested as $a = 1$; Q = fraction of breaking waves with $Q = 0$ for no wave breaking and $Q = 1$ when all waves break; H_B = wave height used to estimate D_B with $H_B = H_m$ in their formula; $H_{\rm rms} = \sqrt{8}\ \sigma_\eta$ = root-mean-square wave height; H_m = local depth limited wave height; k_p = wave number given by $k_p = 2\pi/(C_p T_p)$; and γ = breaker ratio parameter. The values of γ calibrated by Battjes and Stive (1985) were in the range of 0.6–0.8.

The following empirical modifications to Eq. (2.36) have been made by Kobayashi et al. (2005) to extend the time-averaged model to the lower swash zone. The requirement of $0 \le Q \le 1$ implies $H_{\rm rms} \le H_m$ but $H_{\rm rms}$ becomes larger than H_m in very shallow water. When $H_{\rm rms} > H_m$, use is made of $Q = 1$ and $H_B = H_{\rm rms}$ instead of $H_B = H_m$. In addition, $\sigma_* = \sigma_\eta/\bar{h}$ in Eqs. (2.23) and (2.35) becomes too large due to the local use of linear shallow-water wave theory and use is made of $\sigma_* = (\sigma_{*c}\ \sigma_\eta/\bar{h})^{0.5}$ if $\sigma_* > \sigma_{*c} = \gamma/\sqrt{8}$ to reduce the dependency on the mean depth $\bar{h}$. The effects of the local bottom slope $S_b = dz_b/dx$ are included in the parameter a in Eq. (2.36)

$$a = \frac{1}{3} S_b T_p \left(g/\bar{h} \right)^{0.5} \ge 1 \tag{2.39}$$

and the roller slope β_r in Eq. (2.12)

$$\beta_r = (0.1 + S_b) \geq 0.1 \tag{2.40}$$

where the ratio a between the wavelength $T_p(g\bar{h})^{0.5}$ and the horizontal length $(3\bar{h}/S_b)$ imposed by the depth $\bar{h}$ and the slope S_b is used to increase D_B only in the region of small $\bar{h}$ and large S_b. The increase of β_r due to S_b is introduced to reduce the increase of q_r in Eqs. (2.11) and (2.12) resulting from the increased D_B. The formulas in Eq. (2.39) and Eq. (2.40) may need to be improved in the future because the slope effects on D_B and β_r have been examined very little.

Eqs. (2.1)–(2.12) and (2.20)–(2.40) are solved using a finite difference method of constant grid spacing Δx of the order of 1 cm. The finite difference scheme adopted is explained in detail in the next section of this chapter. The measured bottom elevation $z_b(x)$ is specified in the computation domain $x \geq 0$ where $x = 0$ is the seaward boundary outside the surf zone. The measured values of T_p, $\bar{\eta}$, $H_{\rm rms} = \sqrt{8}\sigma_\eta$ and θ as well as $q_r = 0$ at $x = 0$ are specified as input. The landward-marching computation is continued until the computed value of $\bar{h}$ or σ_η becomes negative. This landward limit corresponds to the mean water depth $\bar{h}$ of the order of 0.1 cm. The computation is made with and without the roller effect, corresponding to IROLL = 1 and 0. For IROLL = 0, $q_r = 0$, $D_r = D_B$ and Eq. (2.11) is not used.

Reflected waves are neglected in the time-averaged model. Kobayashi et al. (2005) used the residual cross-shore energy flux F_{xs} at the still water shoreline to estimate the degree of wave reflection where F_x is defined in Eq. (2.6). Assuming that the residual energy flux F_{xs} is reflected from the shoreline and propagates seaward, the reflected root-mean-square wave height $(H_{\rm rms})_r$ may be estimated as

$$(H_{\rm rms})_r = \left[8\ F_{xs}/\left(\rho g C_g \cos\theta\right)\right]^{0.5} \tag{2.41}$$

where C_g and $\cos\theta$ are assumed to be the same for the incident and reflected waves.

After the landward-marching computation, the suspended sediment volume $\overline{V_c}$ per unit horizontal area is estimated using the sediment suspension model by Kobayashi and Johnson (2001)

$$\overline{V_c} = \frac{e_B D_r + e_f D_f}{\rho g (s-1) w_f} \tag{2.42}$$

where s and w_f = specific gravity and fall velocity of the sediment, respectively, and e_B and e_f = suspension efficiencies associated with breaking waves and bottom friction, respectively. They used $e_f = 0.01$ and $e_B = 0.002$, 0.005 and 0.01 to predict beach profile changes observed in large-scale laboratory experiments. Use is made of $e_f = 0.01$ and $e_B = 0.002$ because $e_B = 0.005$ is found to overpredict $\overline{V_c}$ in the following comparisons.

2.2 Finite Difference Method

First-order finite-difference approximations of Eqs. (2.3), (2.1), (2.11) and (2.2) are expressed as

$$\frac{(F_x^*)_{j+1} - (F_x^*)_j}{\Delta x} = -\frac{1}{2}\left[(D_B^*)_{j+1} + (D_B^*)_j\right] - \frac{1}{2}\left[\left(D_f^*\right)_{j+1} + \left(D_f^*\right)_j\right] \tag{2.43}$$

$$\frac{(S_{xx}^*)_{j+1} - (S_{xx}^*)_j}{\Delta x} = -\frac{\left(\bar{h}\right)_{j+1} + \left(\bar{h}\right)_j}{2}\frac{(\bar{\eta})_{j+1} - (\bar{\eta})_j}{\Delta x} - \frac{(\tau_{bx}^*)_{j+1} + (\tau_{bx}^*)_j}{2} \tag{2.44}$$

$$\frac{\left(C_p^2 \cos\theta\right)_{j+1}(q_r)_{j+1} - \left(C_p^2 \cos\theta\right)_j (q_r)_j}{g\Delta x} = \frac{(D_B^*)_{j+1} + (D_B^*)_j}{2} - \frac{(\beta_r q_r)_{j+1} + (\beta_r q_r)_j}{2} \tag{2.45}$$

$$\frac{\left(S_{xy}^*\right)_{j+1} - \left(S_{xy}^*\right)_j}{\Delta x} = -\left(\tau_{by}^*\right)_{j+1} \tag{2.46}$$

where the subscripts $(j+1)$ and j indicates the quantities at nodes located at x_{j+1} and x_j, respectively, with $\Delta x = (x_{j+1} - x_j)$ being the nodal spacing which is of the order of 1 cm for the following study and the notation [variable]* = [variable]$/\rho g$ is used for simplicity. An iterative scheme is adopted to solve the Eqs. (2.43)–(2.46). The initial estimates for starting the iterative process for these equations is provided by assuming that $(D_B^*)_{j+1} = (D_B^*)_j$, $(D_f^*)_{j+1} = (D_f^*)_j$, $(\tau_{bx}^*)_{j+1} = (\tau_{bx}^*)_j$, $(\overline{h})_{j+1} = (\overline{h})_j$, $(C_p^2 \cos\theta)_{j+1} = (C_p^2 \cos\theta)_j$ and $(\beta_r q_r)_{j+1} = (\beta_r q_r)_j$ where Eq. (2.46) is implicit to improve the numerical stability. Eqs. (2.43)–(2.46) are hence approximated as:

$$(F_x^*)_{j+1} = (F_x^*)_j - \Delta x \left[(D_B^*)_j + \left(D_f^* \right)_j \right] \tag{2.47}$$

which is used to guess the initial value of $(\sigma_\eta)_{j+1}$

$$(\bar{\eta})_{j+1} = (\bar{\eta})_j - \frac{\left[(S_{xx}^*)_{j+1} - (S_{xx}^*)_j + \Delta x \, (\tau_{bx}^*)_j \right]}{\left(\bar{h} \right)_j} \tag{2.48}$$

which is used to guess the initial value of $(\overline{h})_{j+1}$

$$(q_r)_{j+1} = (q_r)_j + \frac{g \Delta x \left[(D_B^*)_j - (\beta_r q_r)_j \right]}{\left(C_p^2 \cos\theta \right)_j} \tag{2.49}$$

which is used to guess the initial value of $(q_r)_{j+1}$

$$\left(\tau_{by}^* \right)_{j+1} = - \frac{\left[\left(S_{xy}^* \right)_{j+1} - \left(S_{xy}^* \right)_j \right]}{\Delta x} \tag{2.50}$$

which is used to guess the initial value of $(\overline{V})_{j+1}$

After guessing the initial estimates, Eqs. (2.43)–(2.46) are used iteratively to obtain the improved values of $(\sigma_\eta)_{j+1}$, $(\overline{h})_{j+1}$, $(q_r)_{j+1}$ and $(\overline{V})_{j+1}$. This iterative process is continued till the $\mid$ improved value $-$ estimated value $\mid$ is less than the specified small value ϵ, where use is made of $\epsilon = 10^{-3}$ (m or m/s) for $(\sigma_\eta)_{j+1}$, $(\overline{h})_{j+1}$, and $(\overline{V})_{j+1}$ but $\epsilon = 10^{-6}$ (m^2/s) for $(q_r)_{j+1}$ because q_r is related to σ_η^2 instead of σ_η.

Chapter 3

COMPARISONS WITH FIELD DATA

The developed time-averaged model is compared with the time-dependent model RBREAK by Kobayashi and Karjadi (1996) who compared RBREAK with the field data of February 5 and 6, 1980 obtained by Thornton and Guza (1986) at the Leadbetter beach.

Table 3.1: Wave Conditions at Seaward Boundary for February 5 and 6 Data

Date	d (cm)	T_p (s)	H_{rms} (cm)	θ_i (degrees)	γ	r	
						IROLL = 0	IROLL = 1
Feb.5	300	12.8	49	7.8	0.5	0.22	0.24
Feb.6	300	11.1	28	7.5	0.5	0.24	0.25

Table 3.1 shows the wave conditions at the seaward boundary $x = 0$ located in the still water depth $d = 300$ cm. The mean free surface elevation $\bar{\eta}$ was not reported for both these dates and is assumed to be zero at $x = 0$. Thornton and Guza (1986) calibrated the friction factor $C_f = 0.5\ f_b$ for their longshore current model using the measured longshore currents. Their calibrated value was $f_b = 0.012$. In the following computation, $f_b = 0.01$ is assumed to avoid its fine tuning for each comparison. The breaker ratio parameter γ is calibrated to obtain good agreement between the measured and computed cross-shore variations of σ_η. The initial value of $\gamma = 0.7$ is increased or decreased by an increment of 0.1. The decrease of γ causes the seaward shift of irregular wave breaking. The final calibrated value of γ is 0.5

as listed in Table 3.1. The reflection coefficient in Table 3.1 is the ratio between $(H_{\rm rms})_r$ at $x = 0$ computed using Eq. (2.41) and the specified value of $H_{\rm rms}$ at $x = 0$ which includes the effect of reflected waves. The estimated reflection coefficients in the range of 0.22–0.25 may be somewhat large but may not be unrealistic in view of the field data discussed by Baquerizo et al. (1997).

The field data from February 5 and 6 is limited to just σ_η and $\overline{V}$. Computed results from the time-dependent model RBREAK are limited to σ_η and $\overline{V}$ for February 6. For February 5, computed results from RBREAK are available for $\overline{\eta}, \overline{U}, \sigma_U, \sigma_V, F_x, D_B, D_f, S_{xy}$ and τ_{by} together with σ_η and $\overline{V}$.

In the following two sections the time-averaged model is compared with February 5 and 6 field data and the time-dependent model within the availability of the results presented by Kobayashi and Karjadi (1996).

3.1 Comparisons with February 5 Data

Fig. 3.1 compares the measured and computed cross-shore variations of σ_η and $\bar{\eta}$ and also shows the bathymetry for February 5. The still water shoreline where $z_b = 0$ is located at $x = 72$ m. The difference between the computed σ_η for IROLL = 0 and 1 is very small because the energy equation, Eq. (2.3) does not include the roller-related energy in Eq. (2.11). The time-averaged model with IROLL = 0 and 1 is limited to the lower swash zone unlike the time-dependent model RBREAK which can predict the shoreline movement and includes the duration of no water for its time averaging. The time-averaged model for both IROLL = 0 and 1 yields almost similar wave setup as $\bar{\eta}$ from the time-dependent model which becomes almost tangential to the bottom above the still water shoreline.

Fig. 3.2 shows the computed cross-shore variations of G_{by}, S_{xy} and τ_{by} related to the longshore momentum equation in Eq. (2.2) from both the time-averaged model with IROLL = 0 and 1 and the time-dependent model. The dimensionless function G_{by} given by Eq. (2.34) is simplified as $G_{by} \approx 1.16\overline{V}/\sigma_T$ within the error of

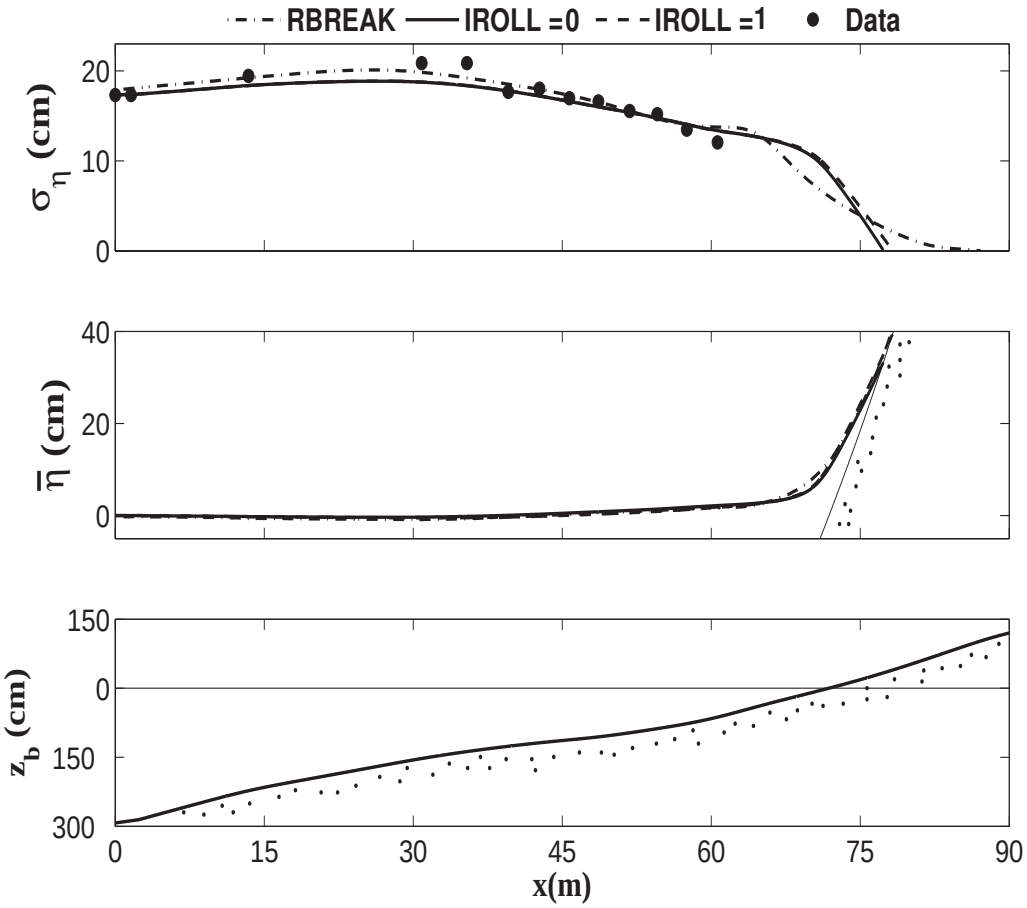

Figure 3.1: Measured and computed (by time-dependent model RBREAK and time-averaged model with IROLL = 0 and 1) cross-shore variations of the mean $\bar{\eta}$ and standard deviation σ_η of the free surface elevation above the bottom profile z_b on February 5.

about 20% as shown in Fig. 3.3. Since τ_{by} is directly proportional to G_{by} as can be seen from Eq. (2.25), the cross-shore variation patterns of τ_{by} and G_{by} are similar. The roller effect (IROLL = 1) increases the longshore radiation stress S_{xy} compared to the non-roller computation (IROLL = 0).

Fig. 3.4 shows the computed cross-shore variations of F_x, D_B and D_f in the energy equation, Eq. (2.3). The energy flux F_x decreases landward due to wave energy dissipation. The value of F_x at the still water shoreline is used in Eq. (2.41) to calculate the reflection coefficient at $x = 0$ listed in Table 3.1. The energy dissipation rate D_f due to bottom friction is much less than the rate D_B caused by wave breaking. The computed D_f yields the turbulent velocity $u'_f = (D_f/\rho)^{1/3}$ (Kobayashi et al. 2005) of about 9 cm/s which is significantly larger than the assumed fall velocity $w_f = 1.65$ cm/s of fine sand in Chapter 4 as shown in Fig. 3.5. This implies significant sediment suspension near the bottom.

The computed mean and standard deviation of the cross-shore velocity U are shown in Fig. 3.6 for both the time-averaged (IROLL = 0 and 1) and time-dependent model. The addition of roller effect (IROLL = 1) increases the undertow current $\overline{U}$ near the still water shoreline compared to the computation without the roller (IROLL = 0) in the time-averaged model. The noticeable difference between the time-averaged and time-dependent models occurs near the shoreline where the values of $\overline{U}$ and σ_U computed by the time-averaged model are smaller than those computed by RBREAK perhaps because the time-averaged model does not include low frequency waves.

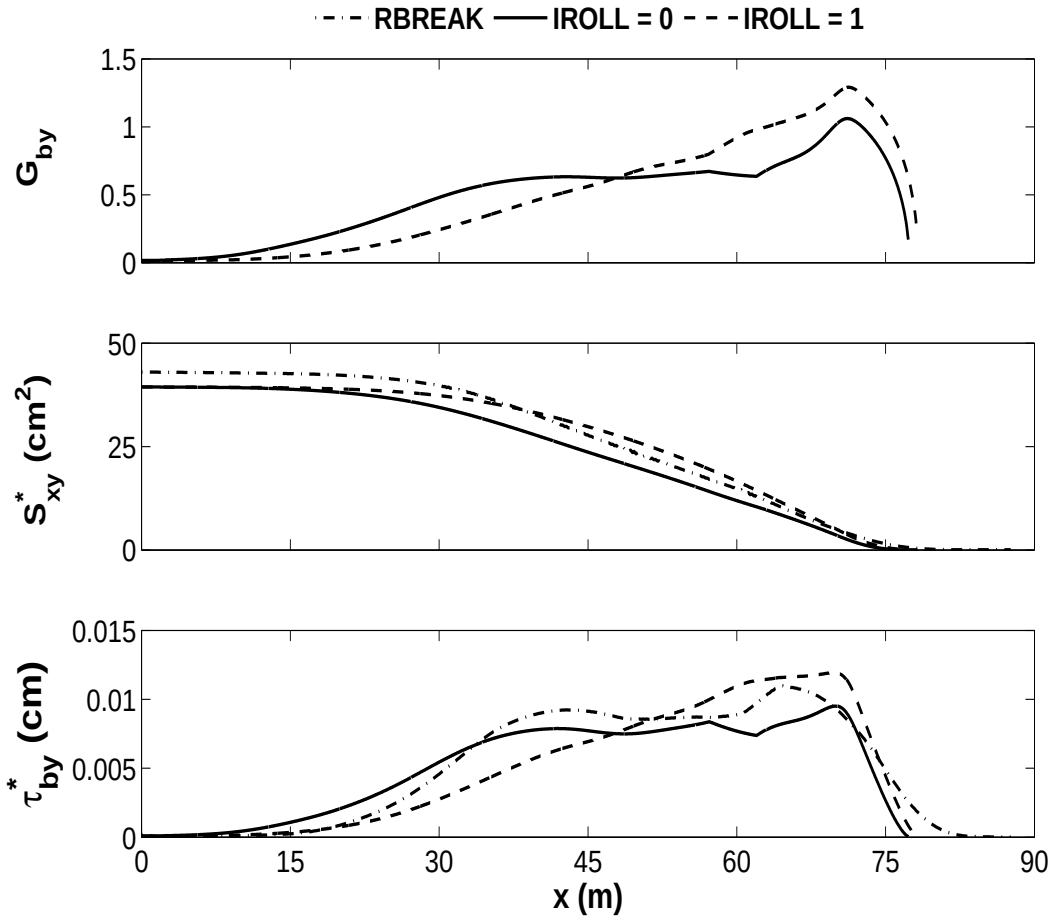

Figure 3.2: Computed dimensionless function G_{by}, longshore radiation stress $S_{xy} = \rho g S^*_{xy}$ and bottom shear stress $\tau_{by} = \rho g \tau^*_{by}$ for February 5.

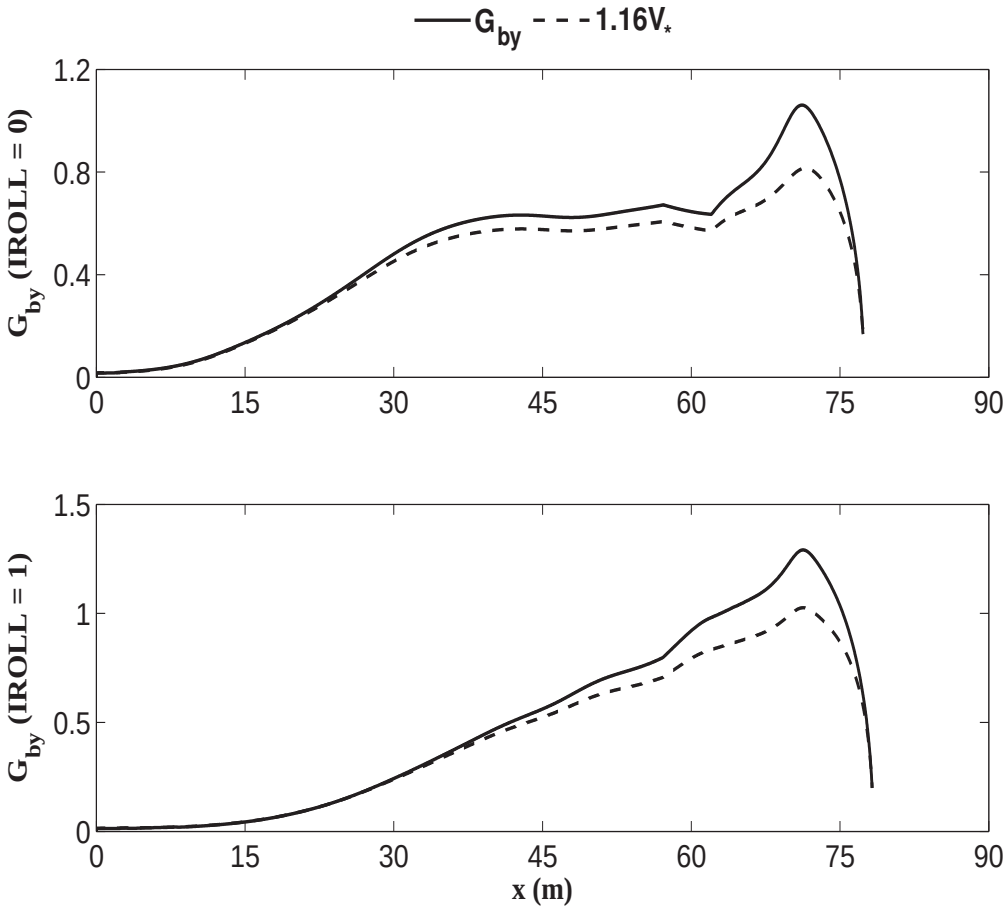

Figure 3.3: Dimensionless function G_{by} calculated by Eq. 2.34 and by approximate expression $1.16V^*$ where $V^* = \overline{V}/\sigma_T$ for IROLL = 0 (top) and 1 (bottom) for February 5.

.

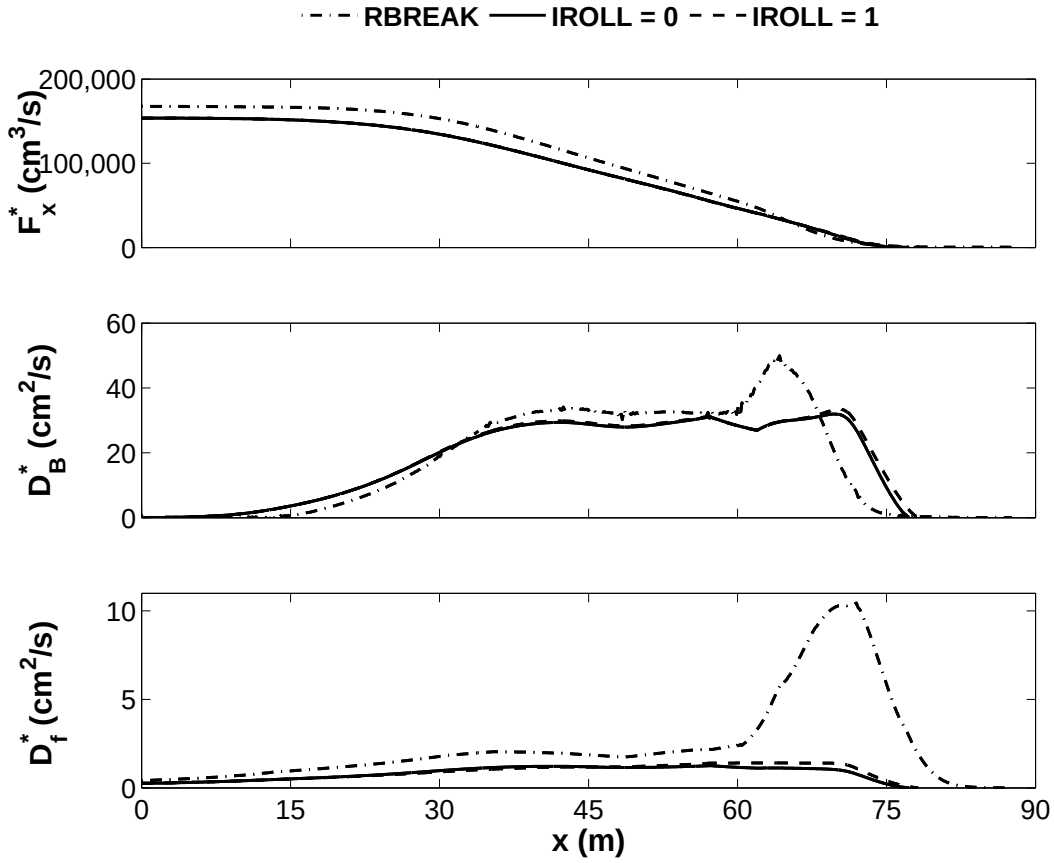

Figure 3.4: Computed cross-shore energy flux $F_x = \rho g F_x^*$, and energy dissipation rates $D_B = \rho g D_B^*$ and $D_f = \rho g D_f^*$ due to wave breaking and bottom friction for the time dependent and time-averaged models for February 5.

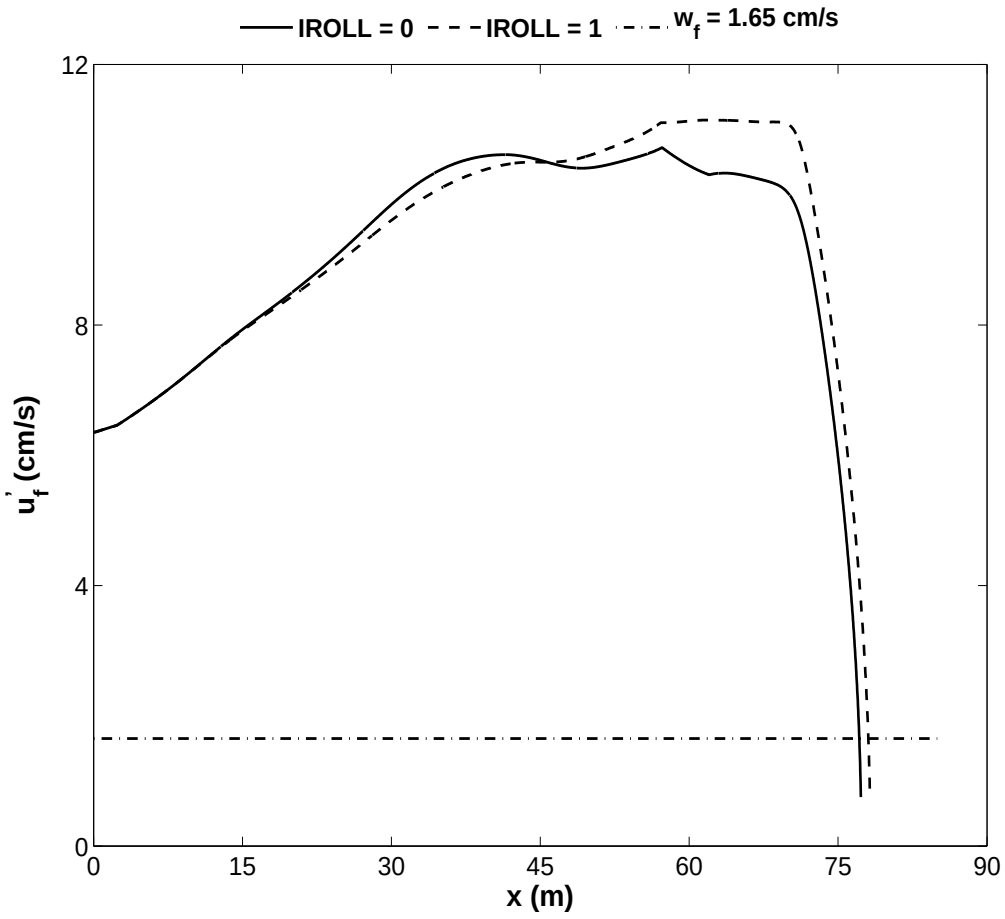

Figure 3.5: Computed turbulent velocity u'_f for the time-averaged model and the sediment fall velocity w_f of fine sand for February 5

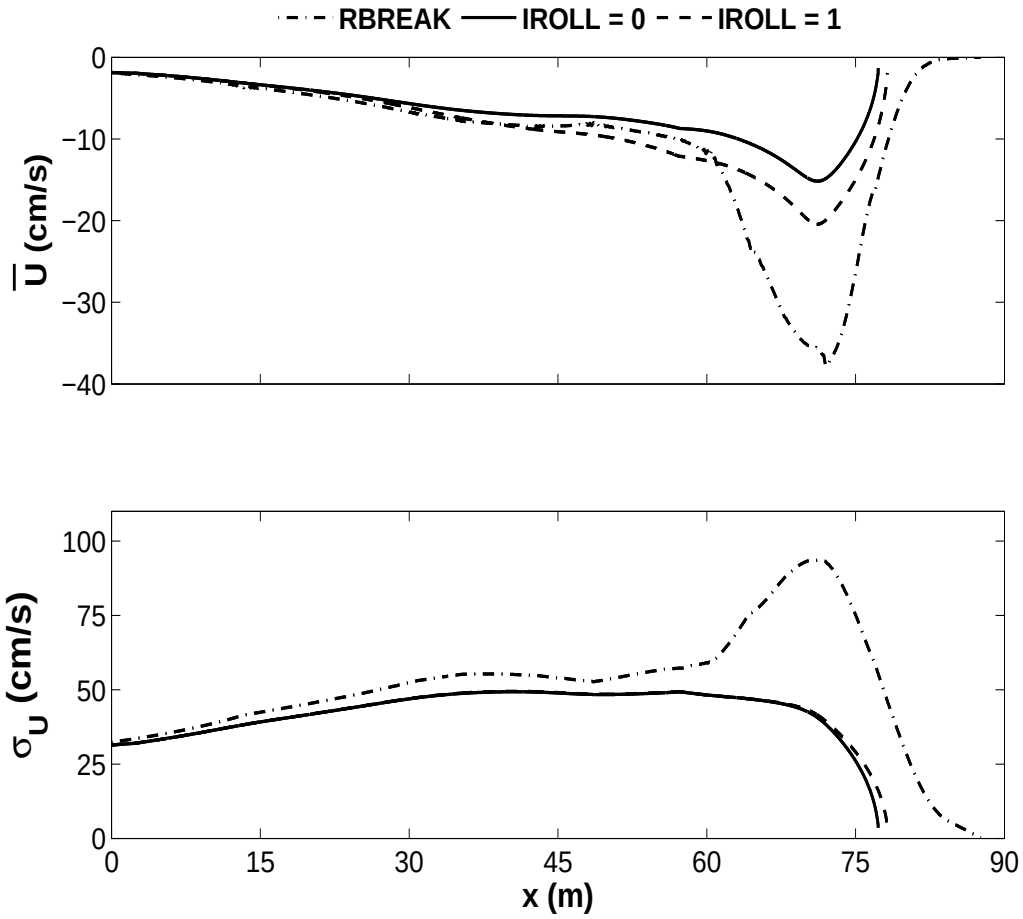

Figure 3.6: Computed mean and standard deviation of U for the time-averaged and time-dependent models for February 5

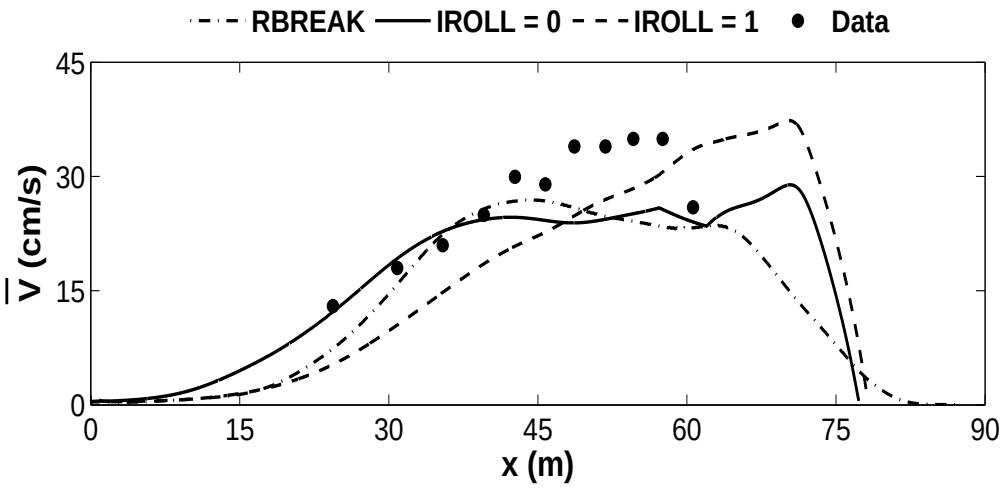

Figure 3.7: Measured and computed (time dependent and time-averaged) cross-shore variations of longshore current $\overline{V}$ for February 5

The measured and computed cross-shore variations of $\overline{V}$ for February 5 are shown in Fig. 3.7. The agreement of $\overline{V}$ is better for IROLL = 0 in the outer surf zone and for IROLL = 1 in the inner surf zone. No data is available for comparison with the numerical model near the shoreline.

The computed standard deviation σ_V representing the longshore oscillatory velocity from the time-averaged and time-dependent models shown in Fig. 3.8 is less than the longshore current $\overline{V}$ shown in Fig. 3.7. The reason for the smaller value of σ_V computed by the time-averaged model near the shoreline is that the time-averaged model does not include the low frequency waves which were included in the time-dependent model. The formula for σ_V in Eq. (2.21) predicts the landward decrease of σ_V with the decrease of $\sin\theta$ due to wave refraction as shown in Fig. 3.8

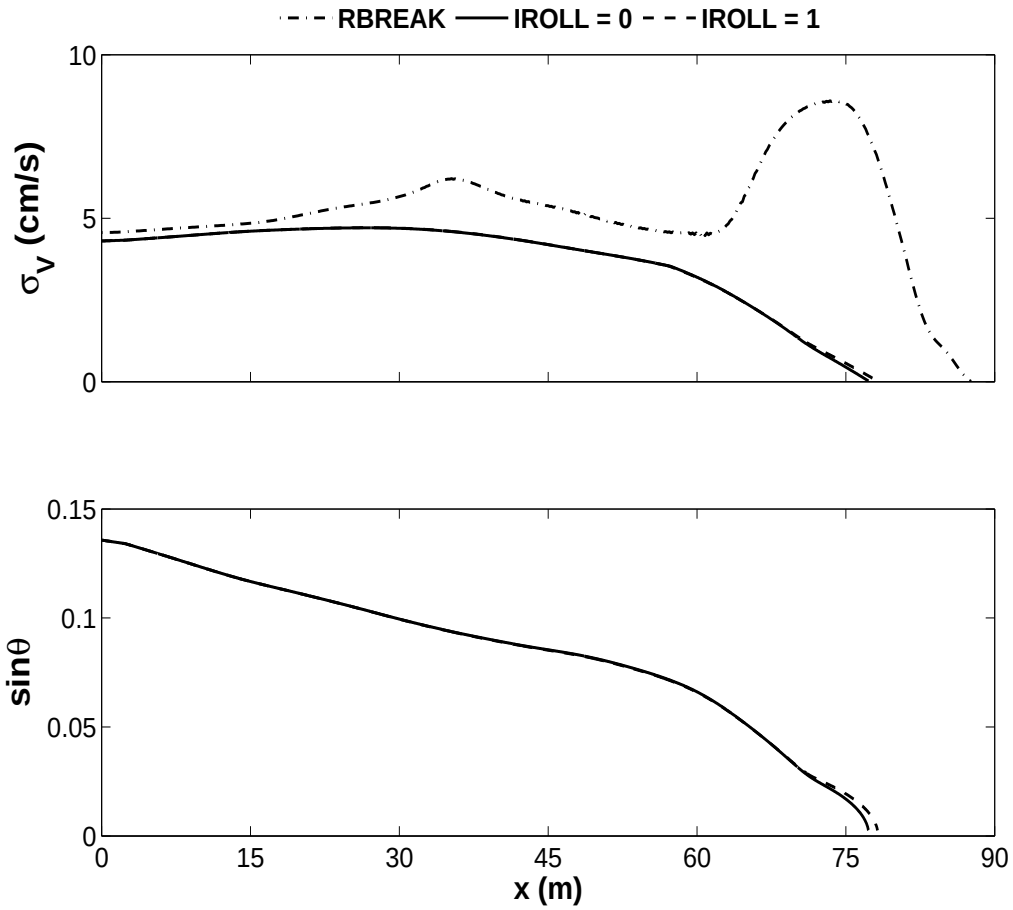

Figure 3.8: Computed standard deviation of V and $\sin\theta$ for the time-averaged model for February 5.

3.2 Comparisons with February 6 Data

The computed results from the time-dependent model is limited to σ_η in Fig. 3.9. The agreement between the measured and computed results is not as good as that achieved for February 5 data probably because the measured data for February 6 is more scattered in the inner surf zone. The still water shoreline was located at x = 70 m. The computed wave setup $\bar{\eta}$ for both IROLL = 0 and 1 becomes tangential to the bottom near the still water shoreline.

Fig. 3.10 shows the measured and computed variations of $\overline{V}$ from the time-averaged (IROLL = 0 and 1) and time dependent model for February 6. The cross-shore variation of measured $\overline{V}$ for this case is less than that for February 5 shown in Fig. 3.7. A significant difference between the computed $\overline{V}$ by the time-averaged model for February 5 and 6 is that $\overline{V} \approx 0$ in the offshore region for February 6 when the incident wave height was smaller as listed in Table 3.1. No wave breaking in the offshore region is apparent in the plot of D_B in Fig. 3.11. Consequently, the longshore radiation stress S_{xy} is almost constant in the offshore region as shown in Fig. 3.12 and the corresponding longshore bottom stress τ_{by} and current $\overline{V}$ are almost zero as shown in Figs. 3.12 and 3.10, respectively.

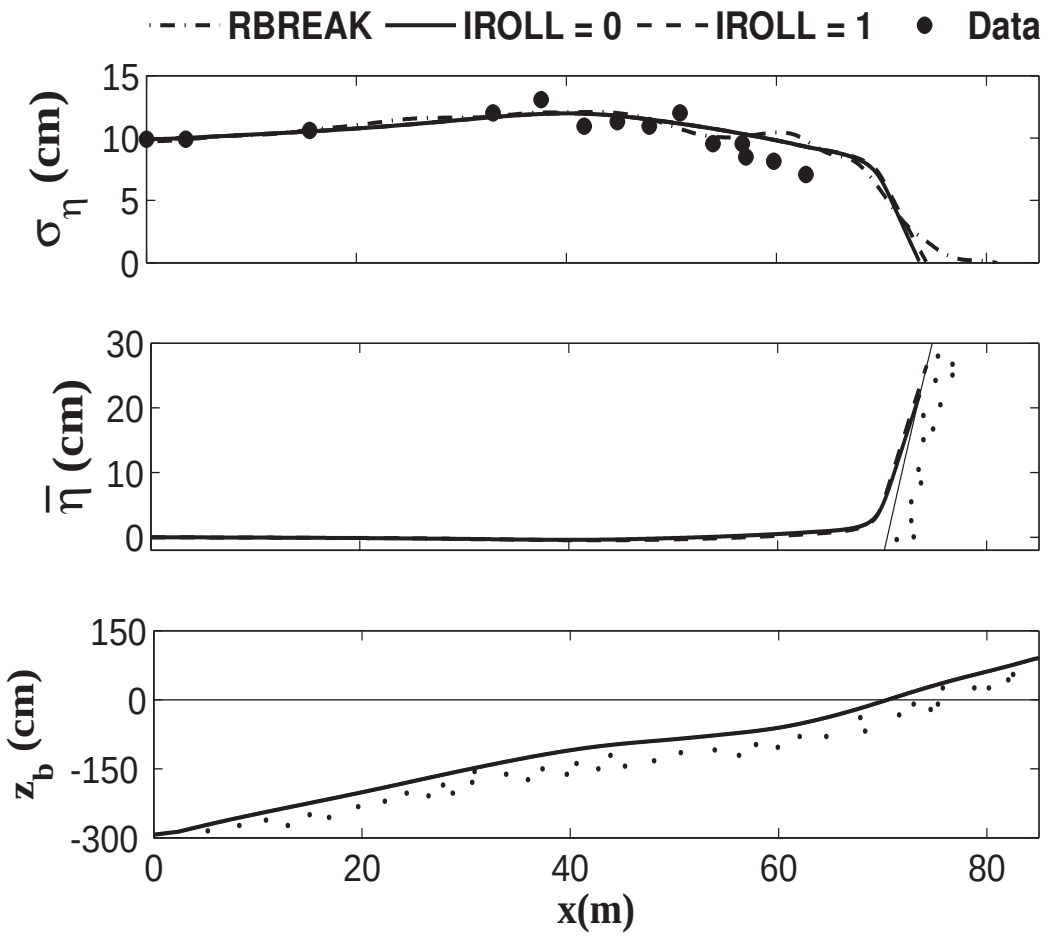

Figure 3.9: Measured and computed (by time-dependent model RBREAK and time-averaged model with IROLL = 0 and 1) cross-shore variations of the standard deviation σ_η of the free surface elevation and the computed wave setup $\bar{\eta}$ from time-averaged model above the bottom profile z_b for February 6.

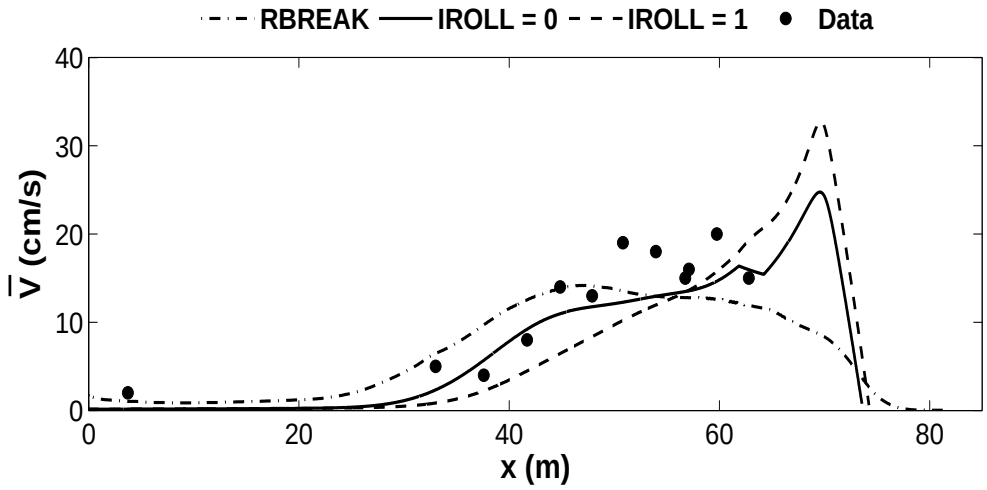

Figure 3.10: Measured and computed (time dependent and time-averaged) cross-shore variations of longshore current $\overline{V}$ for February 6.

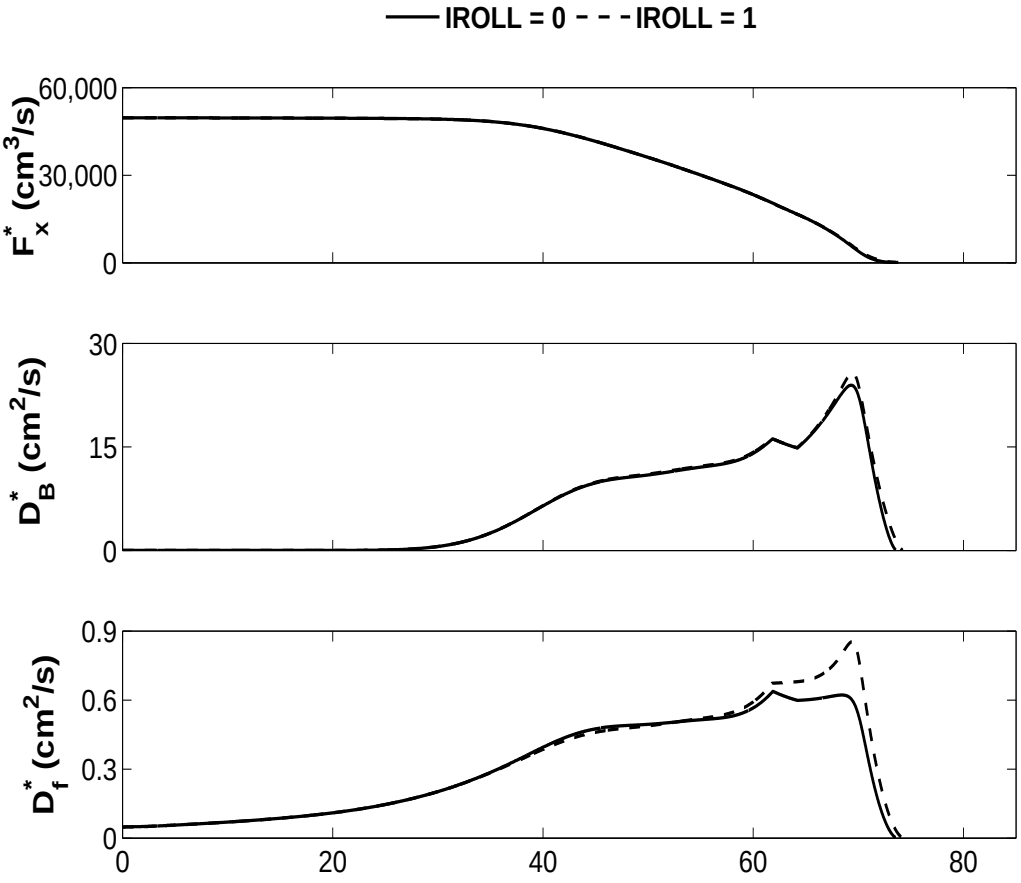

Figure 3.11: Computed cross-shore energy flux $F_x = \rho g F_x^*$, and energy dissipation rates $D_B = \rho g D_B^*$ and $D_f = \rho g D_f^*$ due to wave breaking and bottom friction for the time-averaged model for February 6.

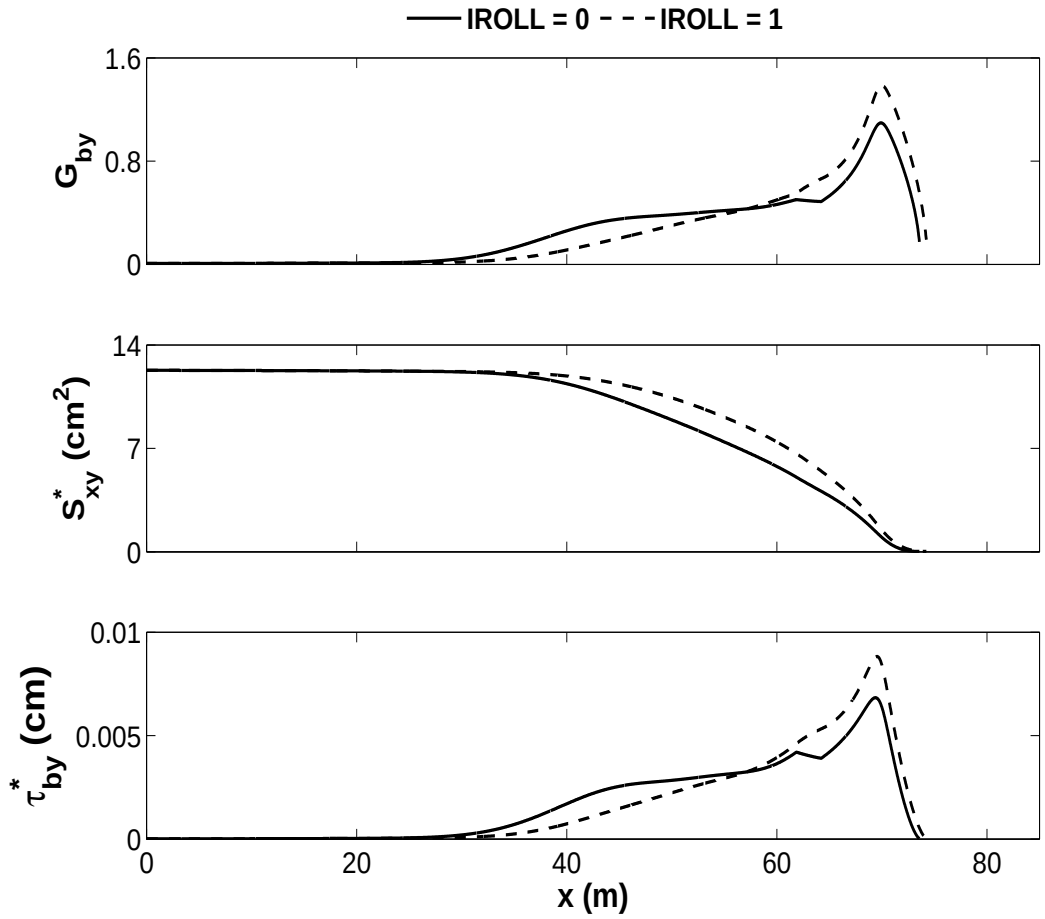

Figure 3.12: Computed dimensionless function G_{by}, longshore radiation stress $S_{xy} = \rho g S^*_{xy}$ and bottom shear stress $\tau_{by} = \rho g \tau^*_{by}$ for the time-averaged model for February 6.

Chapter 4

COMPARISONS WITH LABORATORY DATA

Since the field data available from experiments on February 5 and 6 was limited to just σ_η and $\overline{V}$, additional comprehensive data was needed to compare other hydrodynamic variables calculated by the time-averaged model and those related to the sediment transport dynamics. So the data from the laboratory experiments conducted at the Large-scale Sediment Transport Facility at the US Army Engineer Research and Development Center (Wang et al. 2002a, 2002b) is used.

An extensive amount of data available for two different tests was analyzed to deduce from it the values that can be directly compared with the time-averaged model. The major difference between these two tests was the spectral peak period T_p and the resulting breaker patterns. Pumps were used to circulate the wave-induced longshore current and establish the longshore uniformity of hydrodynamics and morphology on the middle section of the quassi-equilibrium beach comprised of uniform fine sand with a median diameter, d_{50}, of 0.15 mm.

Bathymetric data of the bottom elevations measured every 0.005 m in the cross-shore direction was available. Time-series of water surface elevations measured at 10 different cross-shore positions for a number of cases (each case representing a different elevation of velocity measurement) using capacitance type wave gauges were available for both tests. The cross-shore and longshore velocities measured at 10 different cross-shore locations using Acoustic Doppler Velocimeters (ADVs) were available. For each of these cross-shore locations, velocities were measured at 11 different elevations for the spilling wave test and 8 for the plunging wave test.

Suspended sediment concentrations measured using Fibre-Optic Backscatter Sensors (FOBs) for a number of elevations in the water column were available for 7 cross-shore locations in the spilling wave test and 4 for the plunging wave test. Longshore sediment transport rates using traps were available for 20 different cross-shore locations.

Table 4.1: Wave Conditions at Seaward Boundary for Spilling and Plunging Wave Tests

Breaker	d (cm)	T_p (s)	H_{rms} (cm)	θ_i (degrees)	γ	r	
						IROLL = 0	IROLL = 1
Spilling	76.8	1.5	18.2	10	1.0	0.12	0.12
Plunging	77.3	3.0	18.9	10	0.7	0.13	0.14

Table 4.1 lists the measured values of T_p and H_{rms} in the still water depth d of approximately 77 cm where the incident angle of unidirectional irregular waves was 10 degrees for both tests. The value of γ calibrated for each test is listed in Table 4.1 where the reason for the relatively large value of $\gamma = 1.0$ for the spilling wave test is not clear. Johnson and Smith (2005) analyzed the terms involved in the longshore momentum equation in Eq. (2.2) using the measured velocities for the spilling wave test. Their calibrated value of $f_b = 0.02$ is adopted in the following computations for both tests. The computed reflection coefficients at the seaward boundary $x = 0$ are in the range of 0.12–0.14 which is smaller than those listed in Table 3.1.

The following two sections discuss the analysis procedure for the spilling and plunging wave data for the subsequent comparisons with the time-averaged numerical model.

4.1 Spilling Wave Data Analysis

Analysis of Bathymetry Data

The first step in the data analysis was to get a smoothed profile as the measured profile had many ripples whereas the present numerical model does not account for ripples explicitly. For smoothing, a numerical scheme is used in which the first and last points are kept the same, 3-point averaging is done for the two points adjacent to the end points and 5-point averaging is done for the rest of the data points. The new smoothed value at each point is compared with the measured value. If the difference between the two values is greater than 0.01 mm, the smoothing process is repeated again. For the next iterative loop the present smoothed values become the values to be used for smoothing. This process is repeated till the elevation difference becomes less than 0.01 mm for all the points.

Once the smoothing is achieved, the deviation at each point between the measured profile and the final smoothed profile is calculated. A spatial series of these deviations (ripples and bed forms) is analyzed using a time series subroutine TIMPAR used in the report of Cox et al. (1991) where time is interpretted as cross-shore distance. The mean of the deviation series calculated by TIMPAR is then subtracted from the final smoothed values at each point. This process basically ensures that the mean elevation of the fluctuating spatial variation is zero.

So we have the smoothed profile from x = 0.3 m to x = 17.95 m, but the most seaward wave gauge and ADV were located at x = 0 m which is the seaward boundary of the numerical model. A cubic curve fitted to the smoothed profile from x = 0.3 m to x = 0.55 m and the smoothed bathymetry is extrapolated from x = 0 m to x = 0.295 m with the spacing of 0.005 m to be consistent with the rest of the bathymetry data. Fig. 4.1 shows the smoothed profile superimposed on the measured profile and also the difference between these two profiles which is analogous to ripples present in the bathymetry except near the shoreline. The mean

length and height of these ripples is approximately 8 and 0.8 cm, respectively.

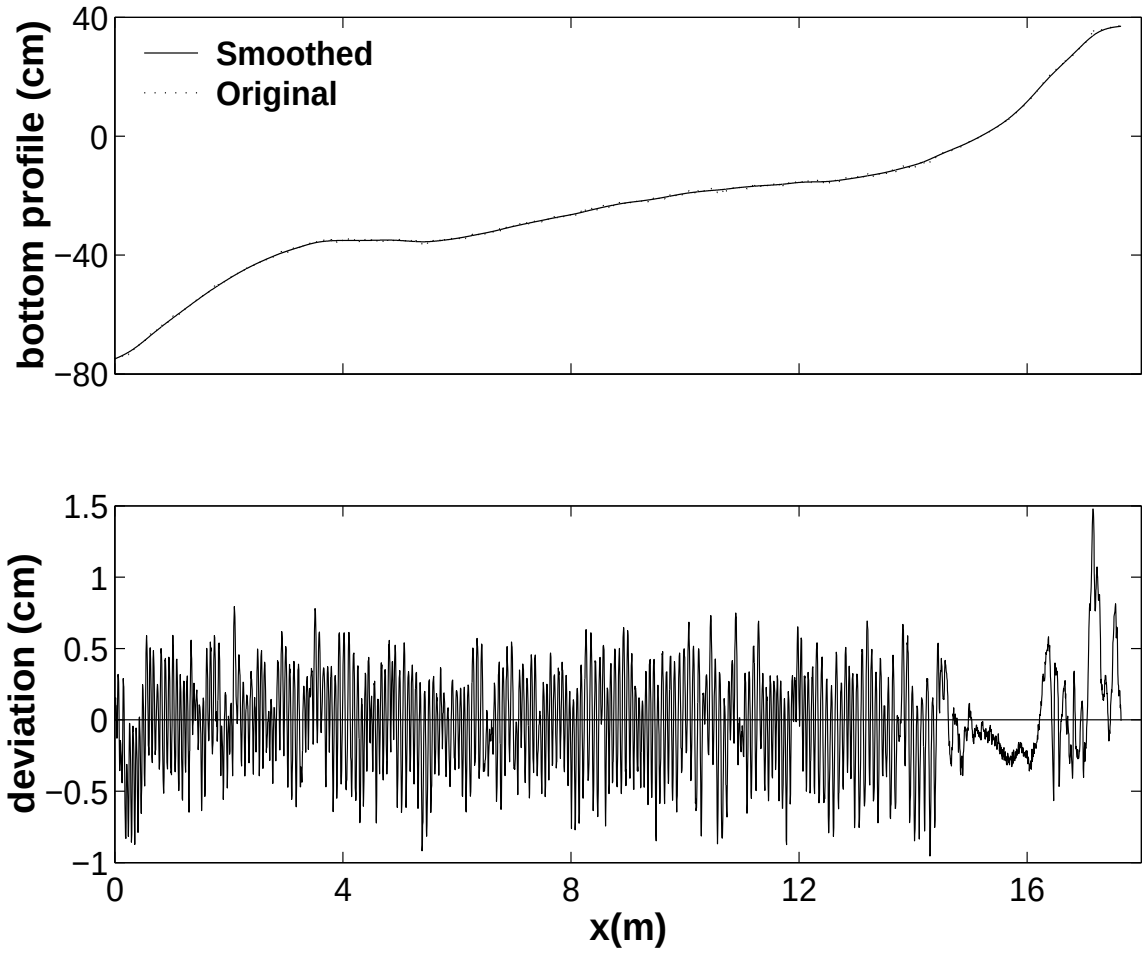

Figure 4.1: Measured and smoothed bathymetric profiles and the cross-shore variation of deviations between them for the spilling wave test

Analysis of Free Surface Elevation Data

The free surface elevation above the still water level (SWL) measured by 10 wave gauges for 11 cases were available. The mean and standard deviation of all the time series corresponding to each wave gauge for all the cases are calculated and averaged to get a single value for a given wave gauge location. Table 4.2 shows

the analyzed values of the mean ($\overline{\eta}$) and standard deviation (σ_η) of the free surface elevation η, the still water depth d and the mean water depth $\overline{h} = d + \overline{\eta}$, for different cross-shore locations x starting from the most seaward wave gauge at $x = 0$.

Table 4.2: Measured Depth and Free Surface Data for Spilling Wave Test

x (m)	d (cm)	$\overline{h}$ (cm)	$\overline{\eta}$ (cm)	σ_η (cm)
0.00	76.79	76.74	-0.05	6.44
2.47	46.03	45.73	-0.30	6.43
3.97	35.38	35.17	-0.21	5.81
5.47	35.32	35.08	-0.24	4.95
7.07	31.38	31.42	0.04	4.80
8.47	25.71	25.84	0.13	4.36
9.87	20.79	20.96	0.17	4.15
11.47	16.91	17.34	0.43	3.76
12.87	15.13	15.70	0.57	2.59
14.47	8.74	9.57	0.83	2.50

Analysis of Cross-Shore and Longshore Velocity Data

The velocity data was available for 10 different cross-shore locations for 11 cases. The vertical positions of the ADV's were changed in different cases to get the vertical variations of the cross-shore u and longshore v velocities. From the given time series the mean and standard deviation of u and v for each cross-shore location and each case are calculated where no averaging is performed unlike $\bar{\eta}$ and σ_η in Table 4.2.

The mean $\overline{u}$ and $\overline{v}$ are fitted to the following profiles:

$$\overline{u} = a_u z_m^2 + b_u z_m + c_u \tag{4.1}$$

$$\overline{v} = a_v \ln(z_m / z_o) \tag{4.2}$$

where z_m = elevation above the local bottom; a_u, b_u, c_u, a_v, and z_o = fitted coefficients at each cross-shore location. The fitted parabolic profiles of $\overline{u}$ and fitted logarithmic profiles of $\overline{v}$ were presented by Wang et al. (2002a).

The fitted parabolic profile of $\overline{u}$ is integrated analytically in the region of $\overline{u} < 0$, where $\overline{u} > 0$ near the free surface in the surf zone, to obtain the average offshore velocity $\overline{U}$ which is assumed to be the same as $\overline{U}$ predicted using Eq. (2.35). The height above the local bottom where the fitted $\overline{u} = 0$ is denoted as h_o. The analytical expression used to calculate $\overline{U}$ is:

$$\overline{U} = \frac{1}{h_*} \int_0^{h_*} \left(a_u z_m^2 + b_u z_m + c_u \right) dz_m = \left(\frac{a_u}{3} h_*^2 + \frac{b_u}{2} h_* + c_u \right) \tag{4.3}$$

where h_* = smaller value of h_o and $\overline{h}$ because $\overline{h} < h_o$ outside the surf zone.

The standard deviation σ_u did not change much above the bottom boundary layer and the vertically-averaged value of σ_u above the boundary layer is assumed to be the same as σ_U predicted using Eq. (2.20). Table 4.3 lists the values for $\overline{U}$ and σ_U used for comparison with the time-averaged model along with the fitted coefficients for the parabolic curve. CC represents the correlation coefficient between the measured data points and the fitted curve. The CC values in the Table 4.3 indicate that the selected parabolic curve fits fairly well to the given data set.

The measured and fitted parabolic profiles of the mean $\overline{u}$ and the measured and average σ_u at the 10 cross-shore locations are shown in Figs. 4.2 and 4.3, respectively.

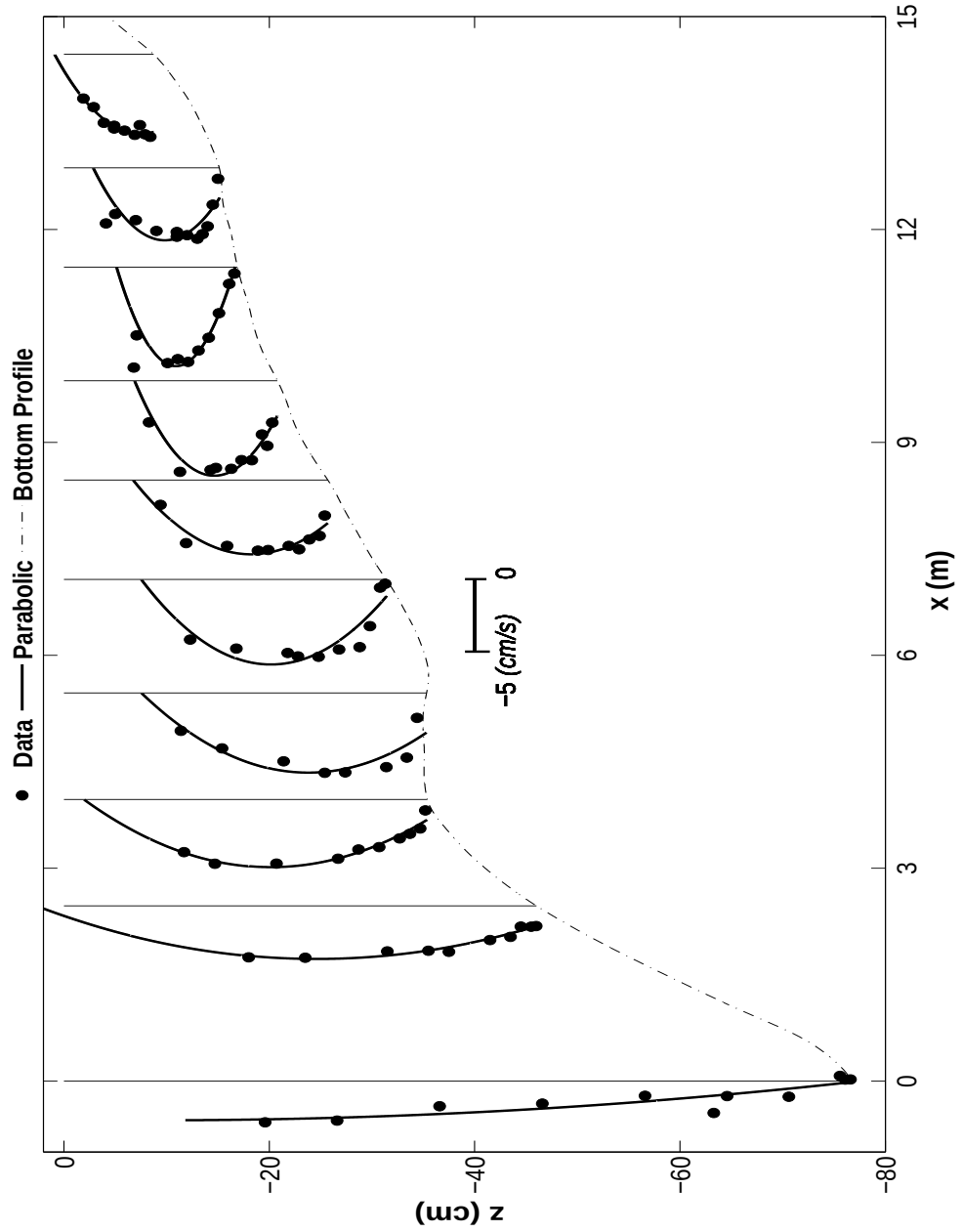

Figure 4.2: Measured and fitted parabolic profiles of mean $\overline{u}$ for spilling wave test

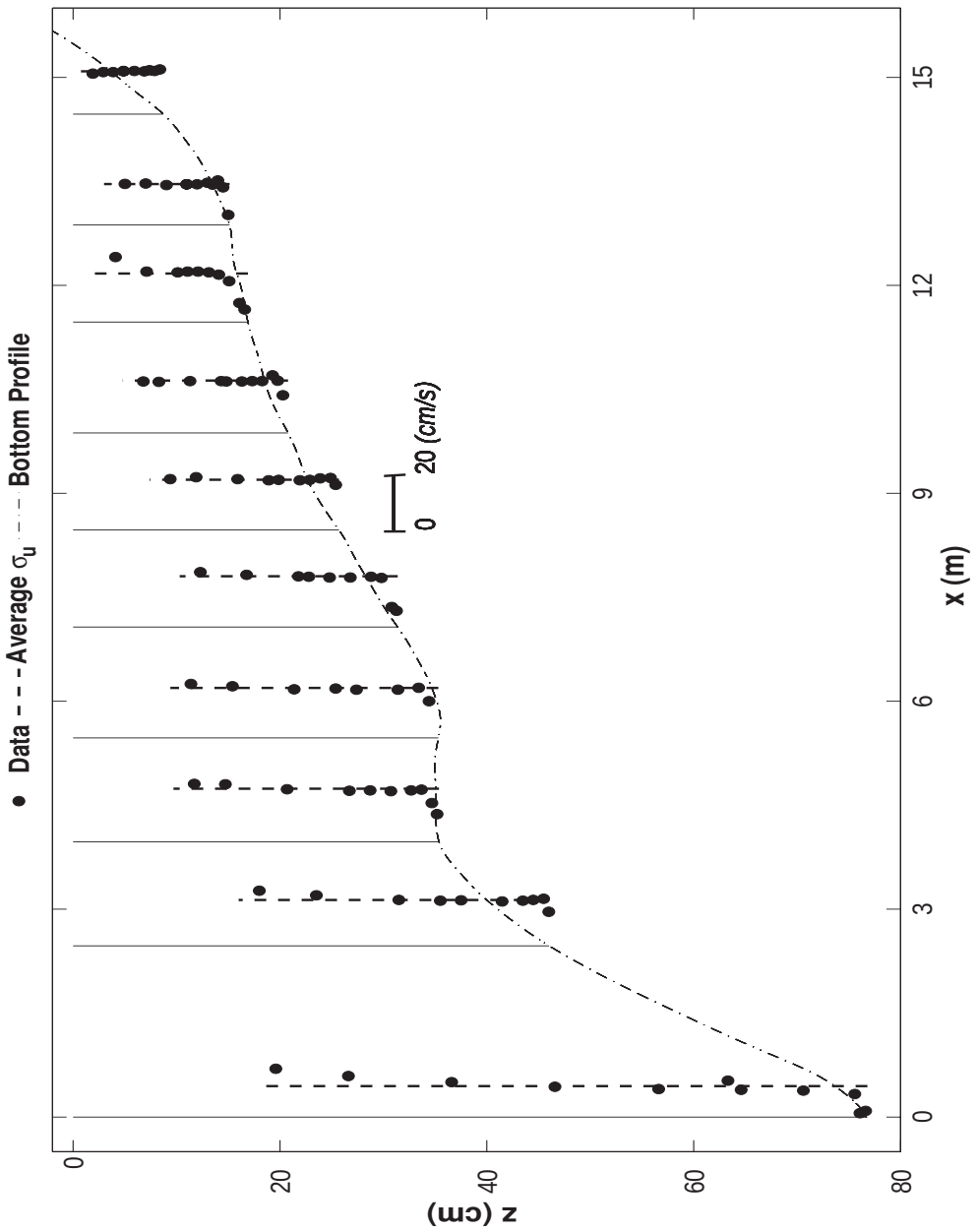

Figure 4.3: Measured and vertically averaged values of σ_u for spilling wave test

Table 4.3: Cross-shore Velocity Data for Spilling Wave Test

x (m)	$\overline{h}$ (cm)	h_0 (cm)	a_u ($\text{cm}^{-1}.\text{s}^{-1}$)	b_u (s^{-1})	c_u ($\text{cm}.\text{s}^{-1}$)	CC	$\overline{U}$ (cm/s)	σ_U (cm/s)
0.00	76.74	136.36	0.0006	-0.80	-0.063	0.883	-1.97	11.18
2.47	45.73	48.72	0.0050	-0.216	-1.433	0.975	-2.86	16.59
3.97	35.17	33.45	0.0144	-0.439	-1.436	0.962	-3.41	19.19
5.47	35.08	27.78	0.0213	-0.491	-2.793	0.828	-4.14	18.05
7.07	31.42	23.85	0.0378	-0.850	-1.228	0.884	-4.20	18.31
8.47	25.84	18.97	0.0395	-0.590	-3.030	0.901	-3.89	18.15
9.87	20.96	13.91	0.1115	-1.373	-2.478	0.961	-4.84	18.88
11.47	17.34	11.78	0.2095	-2.517	0.576	0.994	-4.56	17.50
12.87	15.70	12.28	0.1048	-1.111	-2.166	0.784	-3.72	14.78
14.47	9.57	9.66	0.0793	-0.199	-5.472	0.956	-4.00	15.45

The fitted logarithmic profile of $\overline{v}$ is integrated analytically from $z_m = z_o$ to $z_m = \overline{h}$ to obtain the depth-averaged longshore current $\overline{V}$ predicted by the time-averaged model. The analytical expression used to calculate $\overline{V}$ is:

$$\overline{V} = \frac{1}{\overline{h}} \int_{z_o}^{\overline{h}} a_v \ln\left(\frac{z_m}{z_o}\right) dz_m = a_v \left[\ln\left(\frac{\overline{h}}{z_o}\right) - 1 + \frac{z_o}{\overline{h}}\right] \tag{4.4}$$

The reasonably high CC values in Table 4.4 justify the logarithmic profile for this longshore current data. The vertically averaged value of σ_v is assumed to be the same as σ_V predicted by Eq. (2.21). Table 4.4 lists the final values of $\overline{V}$ and σ_V and also the values of fitted coefficients for the logarithmic profile.

The measured and fitted logarithmic profiles of mean $\overline{v}$ and the measured and average σ_v at the 10 cross-shore locations are shown in Figs. 4.4 and 4.5 respectively.

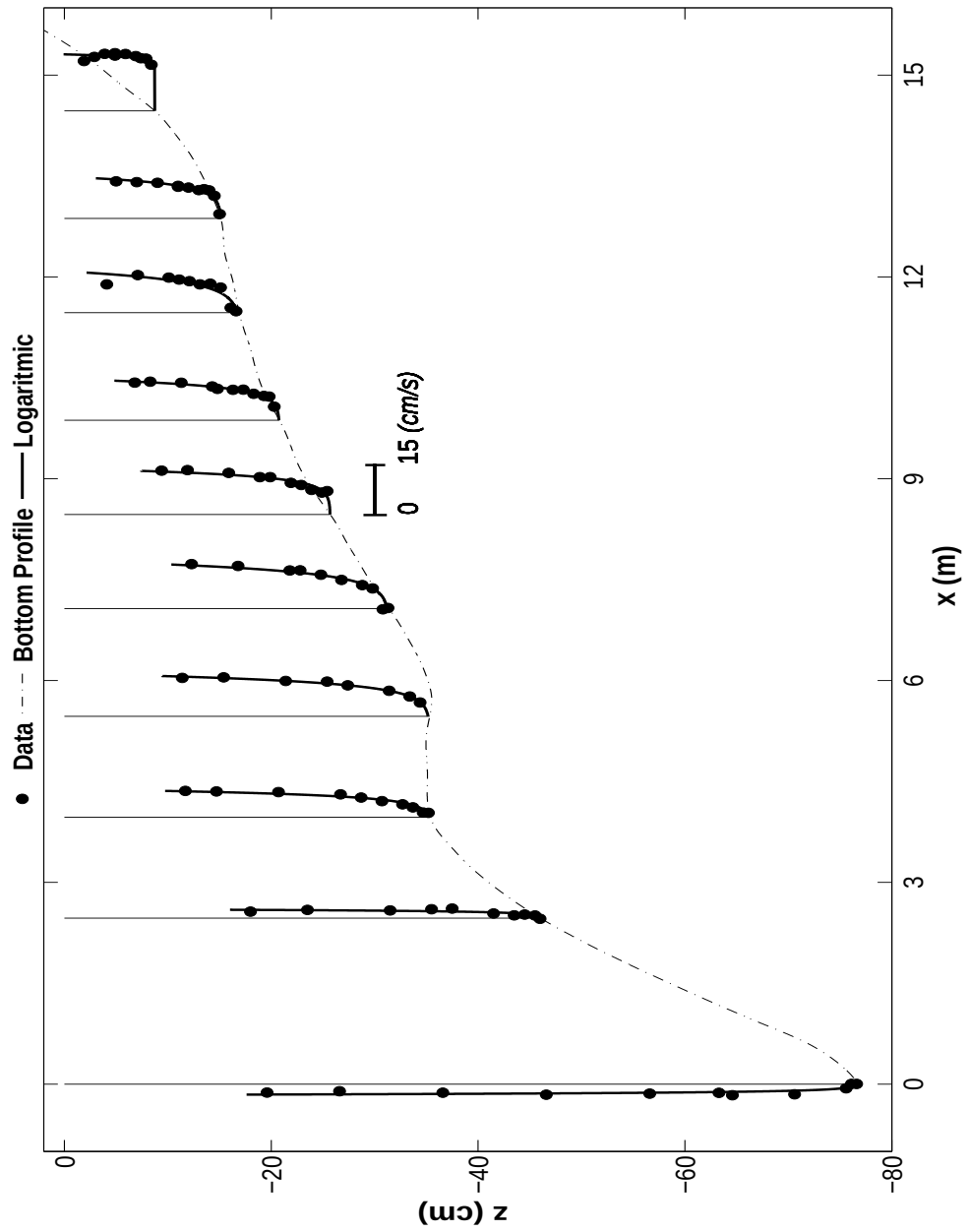

Figure 4.4: Measured and fitted logarithmic profiles of mean $\overline{v}$ for spilling wave test

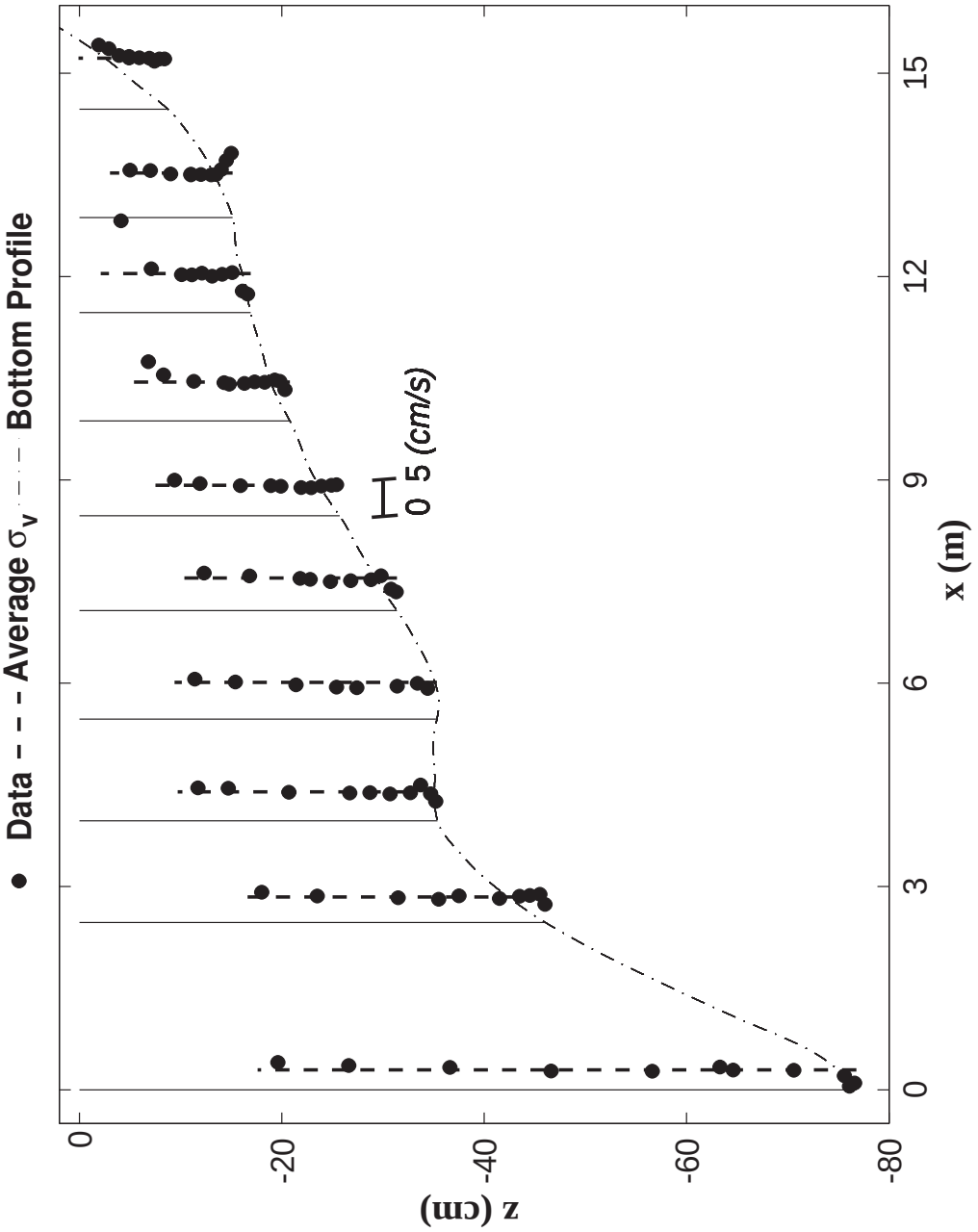

Figure 4.5: Measured and vertically averaged values of σ_v for spilling wave test

Table 4.4: Longshore Velocity Data for Spilling Wave Test

x (m)	$\overline{h}$ (cm)	a_v (cm/s)	z_o (cm)	CC	$\overline{V}$ (cm/s)	σ_V (cm/s)
0.00	76.74	-0.5552	0.156	0.828	-2.72	2.95
2.47	45.73	0.4183	0.076	0.881	2.26	3.75
3.97	35.17	1.5608	0.166	0.968	6.81	4.26
5.47	35.08	2.3499	0.155	0.995	10.40	5.42
7.07	31.42	2.7442	0.174	0.954	11.53	4.81
8.47	25.84	1.8886	0.019	0.941	11.77	4.50
9.87	20.96	2.0282	0.047	0.979	10.35	5.73
11.47	17.34	2.8847	0.235	0.911	9.57	5.76
12.87	15.70	2.0614	0.036	0.963	10.49	6.58
14.47	9.57	0.6710	1.14E-10	0.597	16.21	7.54

Analysis of Concentration Data

The concentration data for the spilling wave test was available for 7 different cross-shore locations and a number of elevations for several repeated runs. The lowest concentration measurement was taken at a height of 1 cm above the local bottom. Averaging was done for all the runs to get a single value of measured concentration data at any elevation for a given cross-shore location. The mean $\bar{c}$ is fitted to the exponential and power-form profiles as follows:

$$\bar{c} = \bar{c_b} \exp(-z_m/\ell_c) \tag{4.5}$$

$$\bar{c} = \bar{c_a}(z_a/z_m)^m \tag{4.6}$$

where $\bar{c_b}$, ℓ_c, $\bar{c_a}$, and m = fitted coefficients at each cross shore location; and z_a = lowest elevation of the power-form profile of $\bar{c}$ which is takes as z_a = 1 cm. Fig. 4.6 shows the fitted power-form and exponential profiles. Kobayashi et al. (2005) showed that their concentration data could be fitted by the power-form and exponential profiles equally well. For the present concentration data, the power-form profile gives a better fit as can be clearly seen from the values of correlation

Table 4.5: Fitted Exponential and Power-Form Profiles for $\bar{c}$ for Spilling Wave Test

x	*Exponential*			*Power-form*			
(m)	$\bar{c}_b$ (g/l)	l_c (cm)	CC	$\bar{c}_a$ (g/l)	m	CC	α_c
3.97	4.9635	4.69	0.874	10.0172	1.32	0.955	1.439
5.47	2.7807	5.43	0.854	5.6922	1.19	0.942	3.656
7.07	1.6562	4.01	0.812	1.5133	1.09	0.974	5.507
8.47	1.6613	3.33	0.902	1.5548	1.18	0.990	1.627
9.87	6.4989	2.44	0.874	4.8385	1.48	0.988	4.160
11.47	4.3156	1.61	0.921	1.6760	1.33	0.974	3.093
12.87	3.6734	1.57	0.920	1.0083	1.10	0.957	1.834

coefficient CC between the data points and the fitted profile in Table 4.5. The power-form profile given by Eq. (4.6) is adopted hereafter.

The fitted power-form profile of $\bar{c}$ is integrated analytically from $z_m = z_a =$ 1 cm to $z_a = \overline{h}$ to obtain the suspended sediment volume per unit area which is compared to $\overline{V_c}$ predicted using Eq. (2.42). The analytical expression of $\overline{V_c}$ is given by:

$$\overline{V_c} = \int_{z_a}^{\bar{h}} \bar{c}_a \left(\frac{z_a}{z_m}\right)^m dz_m = \frac{\bar{c}_a z_a}{m-1}\left[1 - \left(\frac{z_a}{\bar{h}}\right)^{m-1}\right] \tag{4.7}$$

where $\bar{c}_a$ in the above expression is the volumetric concentration obtained by converting mass concentration in Fig. 4.6 to volumetric concentration using the sand density of 2.65 g/cm^3. The measured values of $\overline{V_c}$ are shown in Table 4.6. The measured values of $\sigma_c/\bar{c}$ at each cross-shore location are plotted in Fig. 4.7 and the value of α_c in Table 4.5 is the vertically averaged value at each location.

The time-averaged cross-shore and longshore sediment fluxes are given by the following equations:

$$\begin{aligned}\overline{uc} &= \bar{u}\bar{c} + \overline{(u-\bar{u})(c-\bar{c})} \\ \overline{vc} &= \bar{v}\bar{c} + \overline{(v-\bar{v})(c-\bar{c})}\end{aligned}$$

The velocity and concentration measurements in these tests were not synchronized and the correlation terms on the right hand side of these equations cannot be quantified. The measured offshore suspended sediment transport rate q_{off} due to the mean current $\bar{u}$, which is positive onshore, is obtained by integrating $(-\bar{u}\bar{c})$ analytically in the region of $\overline{u} < 0$ and $z_m \geq 1$ cm where use is made of the fitted profiles of $\overline{u}$ and $\overline{c}$ in Eqs. (4.1) and (4.6) respectively. The integral expression for calculating q_{off} is given as:

$$q_{\text{off}} = \int_{z_a}^{h_*} (-\bar{u})\bar{c}dz_m = \int_{z_a}^{h_*} -(a_u z_m^2 + b_u z_m + c_u)\bar{c}_a \left(\frac{z_a}{z_m}\right)^m dz_m \tag{4.8}$$

which results in the analytical expression

$$q_{\text{off}} = \bar{c}_a z_a \left[\frac{a_u z_a^2}{3-m}\left(1-\xi_o^{3-m}\right) + \frac{b_u z_a}{2-m}\left(1-\xi_o^{2-m}\right) + \frac{c_u}{1-m}\left(1-\xi_o^{1-m}\right)\right] \tag{4.9}$$

with $\xi_o = h_0/z_a$; $z_a = 1$ cm and $\bar{c}_a$ = volumetric concentration of suspended sediment.

The measured longshore suspended sediment transport rate q_{ls} is obtained by integrating $(\bar{v}\bar{c})$ analytically from $z_m = 1$ cm to $z_m = \overline{h}$ using Eqs. (4.2) and (4.6) respectively. The integral expression and the analytical expression derived are expressed as:

$$q_{\text{ls}} = \int_{z_a}^{\bar{h}} \bar{v}\bar{c}dz_m = \int_{z_a}^{\bar{h}} a_v \ln\left(\frac{z_m}{z_o}\right)\bar{c}_a \left(\frac{z_a}{z_m}\right)^m dz_m \tag{4.10}$$

$$q_{\text{ls}} = \frac{z_a a_v \bar{c}_a}{(1-m)^2}\left\{\left(\frac{\bar{h}}{z_a}\right)^{1-m}\left[(1-m)\ln\left(\frac{\bar{h}}{z_o}\right) - 1\right] - (1-m)\ln\left(\frac{z_a}{z_o}\right) + 1\right\} \tag{4.11}$$

The measured values of q_{off} and q_{ls} calculated from Eqs. (4.9) and (4.11) are shown in Table 4.6.

Table 4.6: Measured Volume, Offshore and Longshore Transport Rates of Suspended Sediment for Spilling Wave Test

x (m)	$\overline{V_c}$ (cm)	q_{off} (cm^2/s)	q_{ls} (cm^2/s)
3.97	0.0081	0.0236	0.0421
5.47	0.0054	0.0199	0.0452
7.07	0.0018	0.0064	0.0165
8.47	0.0015	0.0055	0.0151
9.87	0.0029	0.0135	0.0246
11.47	0.0011	0.0045	0.0086
12.87	0.0010	0.0036	0.0093

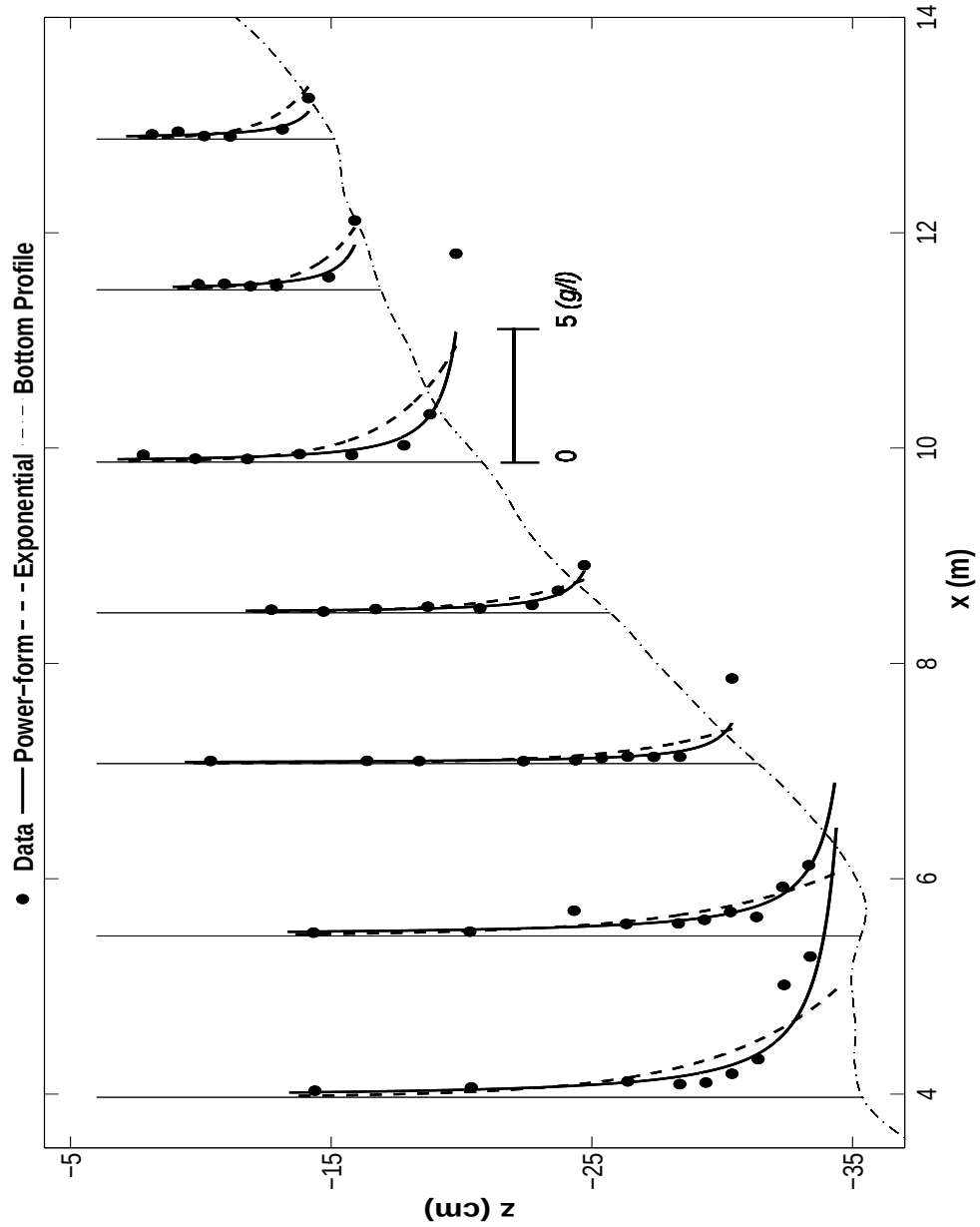

Figure 4.6: Measured and fitted power-form and exponential profiles of mean concentration $\bar{c}$ for spilling wave test

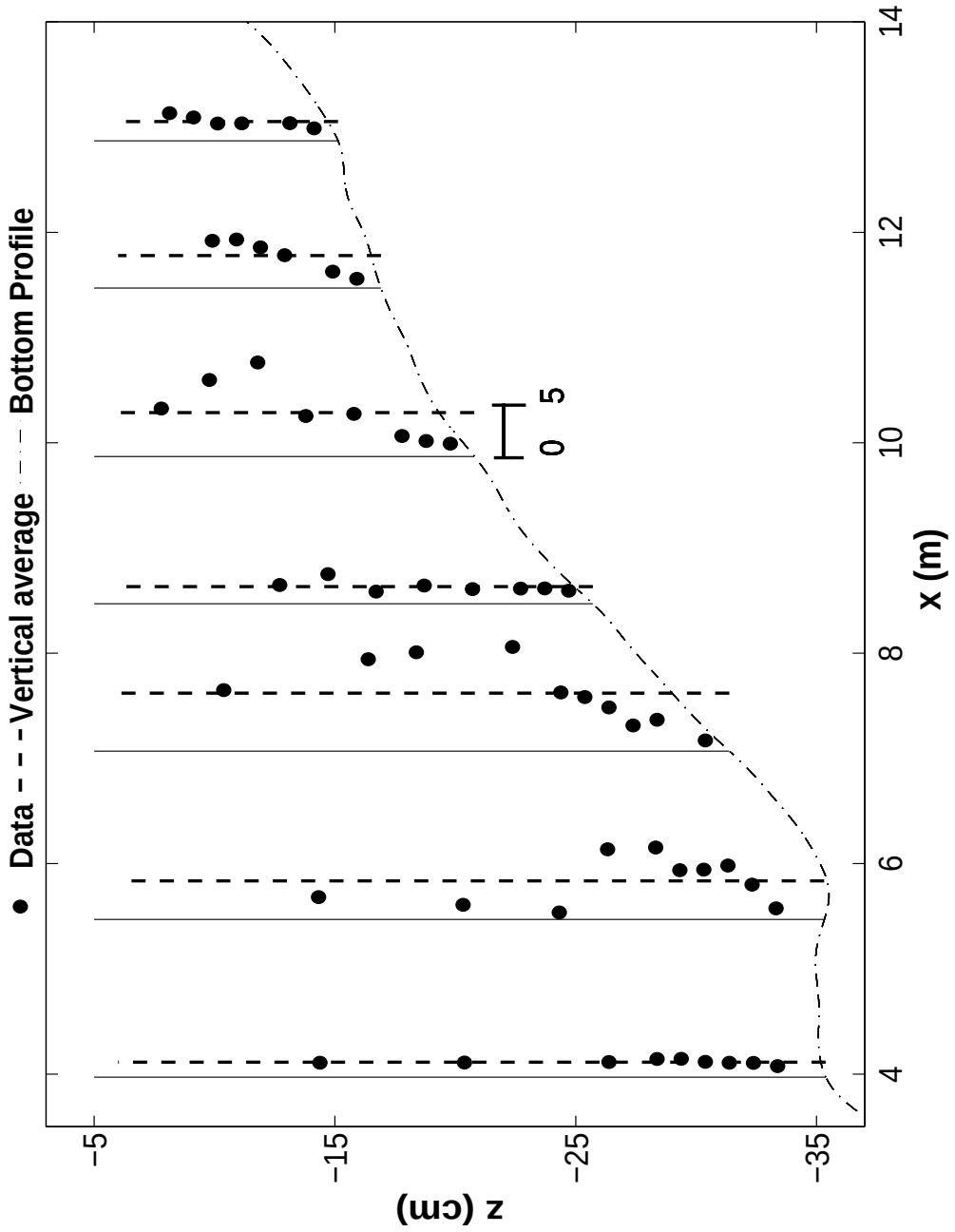

Figure 4.7: Measured and vertically averaged values of $\sigma_c/\bar{c}$ for spilling wave test

4.2 Plunging Wave Data Analysis

All the data of the plunging wave test are analyzed in the same way as that adopted for spilling wave data analysis.

Analysis of Bathymetry Data

Fig. 4.8 shows the smoothed and measured bottom profiles and also the cross-shore variation of the ripples and bed form present in the bathymetry. The mean length and height of the ripples are approximately 13 and 0.9 cm but the bed forms were different seaward of the bar crest and near the shoreline.

Analysis of Free Surface Elevation Data

The free surface elevation data measured by 10 wave gauges for 8 cases was available. A single value of the mean ($\overline{\eta}$) and standard deviation (σ_η) of the free surface elevation η and the mean water depth $\overline{h}$ is calculated for all the 10 wave gauges. But due to erroneous results for 3 gauges, only 7 cross-shore locations are considered for later comparison with the time-averaged model. Table 4.7 lists the measured values.

Table 4.7: Measured Depth and Free Surface Data for Plunging Wave Test

x (m)	d (cm)	$\overline{h}$ (cm)	$\overline{\eta}$ (cm)	σ_η (cm)
0.00	77.27	76.68	-0.59	6.68
3.97	29.79	29.00	-0.79	6.07
5.47	37.13	36.66	-0.47	4.92
7.07	31.13	31.47	0.34	4.61
9.87	24.66	25.05	0.39	3.89
11.47	20.31	20.89	0.58	3.70
14.47	10.93	11.92	0.99	3.16

Analysis of Cross-shore and Longshore Velocity Data

The velocity data was available for 10 different cross-shore locations for 8 cases out of which only the first 7 cases are considered for analysis as for the last case the vertical position of some of the ADV's was above the still water level. Eqs. (4.1) and (4.2) are used for fitting parabolic and logarithmic profiles to mean $\overline{u}$ and $\overline{v}$, respectively. These fitted profiles are integrated to get $\overline{U}$ and $\overline{V}$ except for the mean $\overline{u}$ at $x = 0$ and mean $\overline{v}$ at $x = 0$ and 14.47 m, where the vertically averaged value of the data points was used because the data points did not follow the assumed profile. Results of the analysis of velocity data are shown in Tables 4.8 and 4.9 and plotted in Figs. 4.9–4.12. For the integration of the $\overline{v}$ profiles, still water depth d was used as the upper limit because the data for wave setup $\overline{\eta}$ is not available for three cross-shore locations. This choice does not makes much difference in the analysis because the magnitude of $\bar{\eta}$ is less than 1 cm and much smaller than d in Table 4.7.

Table 4.8: Cross-shore Velocity Data for Plunging Wave Test

x (m)	d (cm)	h_0 (cm)	a_u ($\text{cm}^{-1}.s^{-1}$)	b_u (s^{-1})	c_u (cm.s^{-1})	CC	$\overline{U}$ (cm/s)	σ_u (cm/s)
0.00	77.27	NaN	0.0000	0.0000	1.9796	NaN	1.98	18.58
2.47	42.50	27.56	0.0119	-0.2797	-1.3395	0.669	-2.18	26.64
3.97	29.79	20.41	0.0870	-1.9494	3.5255	0.899	-4.28	31.49
5.47	37.13	26.05	0.0074	0.2199	-10.7337	0.992	-6.20	20.22
7.07	31.13	21.47	0.0492	-0.9178	-2.9963	0.841	-5.28	21.83
8.47	27.17	22.05	0.0558	-1.2249	-0.1231	0.873	-4.58	21.03
9.87	24.66	16.28	0.0753	-0.8070	-6.8337	0.981	-6.75	19.88
11.47	20.31	12.98	0.1861	-2.3506	-0.8365	0.979	-5.64	21.60
12.87	17.24	16.37	0.0199	0.0276	-5.7897	0.910	-3.78	15.39
14.47	10.93	7.44	0.1021	-0.7599	0.0000	1.000	-0.94	14.39

Table 4.9: Longshore Velocity Data for Plunging Wave Test

x (m)	d (cm)	a_v (cm/s)	z_0 (cm)	CC	$\overline{V}$ (cm/s)	σ_v (cm/s)
0.00	77.27	0.0000	0.000	NaN	0.00	5.44
2.47	42.50	0.7951	1.857	0.656	1.73	6.24
3.97	29.79	2.5333	1.568	0.827	5.06	8.44
5.47	37.13	0.8034	0.000	0.796	11.50	7.27
7.07	31.13	3.1186	0.294	0.973	11.45	6.57
8.47	27.17	3.4626	0.500	0.943	10.43	6.18
9.87	24.66	1.4531	0.003	0.967	11.51	6.75
11.47	20.31	3.7789	0.237	0.858	13.09	7.13
12.87	17.24	1.3786	0.000	0.942	16.12	8.35
14.47	10.93	0.0000	0.000	NaN	15.21	11.16

Table 4.10: Fitted Exponential and Power-Form Profiles for $\bar{c}$ for Plunging Wave Test

x	*Exponential*			*Power-form*			
(m)	$\bar{c}_b$ (g/l)	l_c (cm)	CC	$\bar{c}_a$ (g/l)	m	CC	α_c
3.97	4.8084	12.58	0.710	4.9990	0.37	0.805	2.131
7.07	2.2054	3.69	0.823	0.8410	0.72	0.924	1.536
12.87	3.8745	1.87	0.886	1.5506	1.06	0.948	1.323

Analysis of Concentration Data

Concentration data for the plunging wave test was available for 4 different cross-shore locations out of which only 3 locations gave reliable data. For plunging wave test also power-form gave a better fitting. The results of the analysis are presented in Tables 4.10 and 4.11 and the plotted profiles are shown in Figs. 4.13 and 4.14.

Table 4.11: Measured Volume, Offshore and Longshore Transport Rates of Suspended Sediment for Plunging Wave Test

x (m)	$\overline{V_c}$ (cm)	q_{off} (cm^2/s)	q_{ls} (cm^2/s)
3.97	0.0726	0.1039	0.0226
7.07	0.0081	0.0176	0.0018
12.87	0.0073	0.0229	0.0016

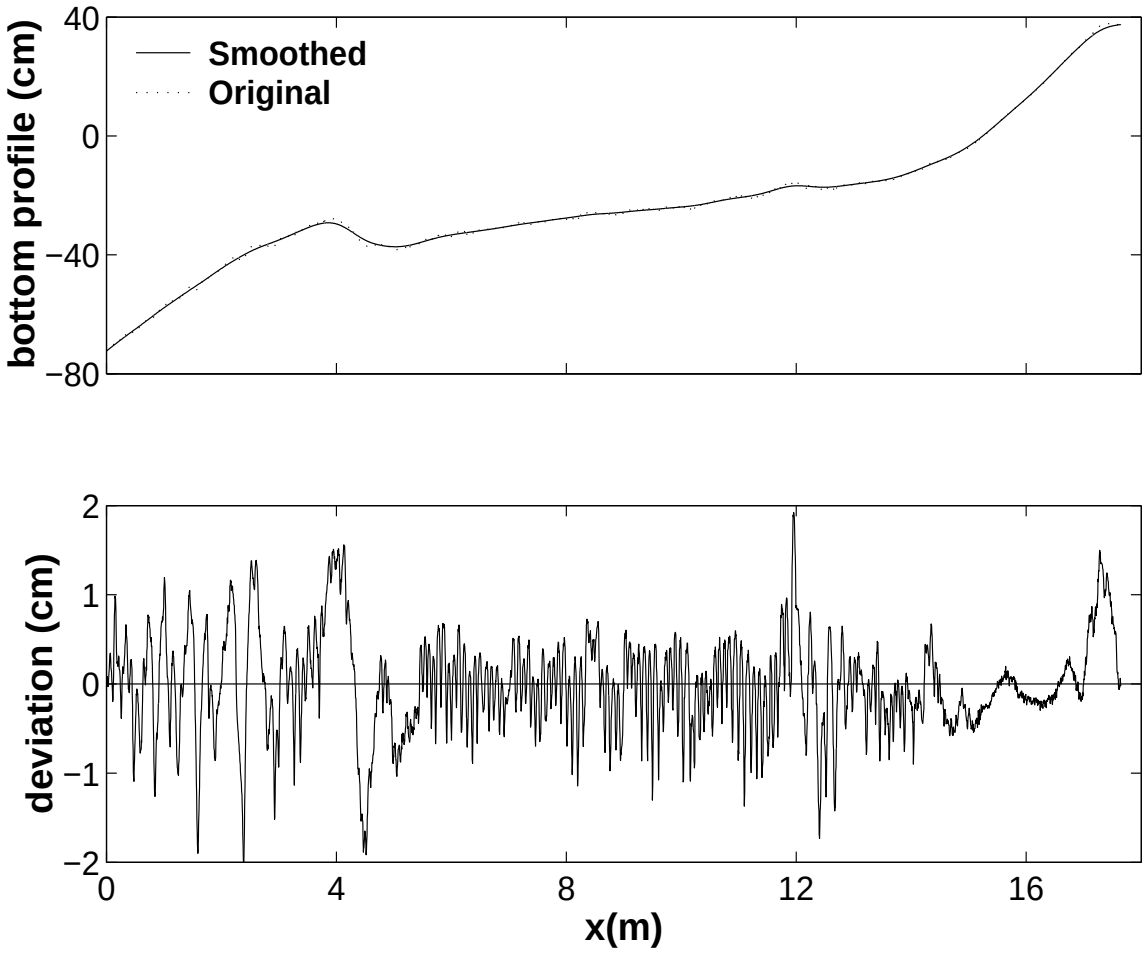

Figure 4.8: Measured and smoothed bathymetric profiles and the cross-shore variation of deviations between them for the plunging wave test

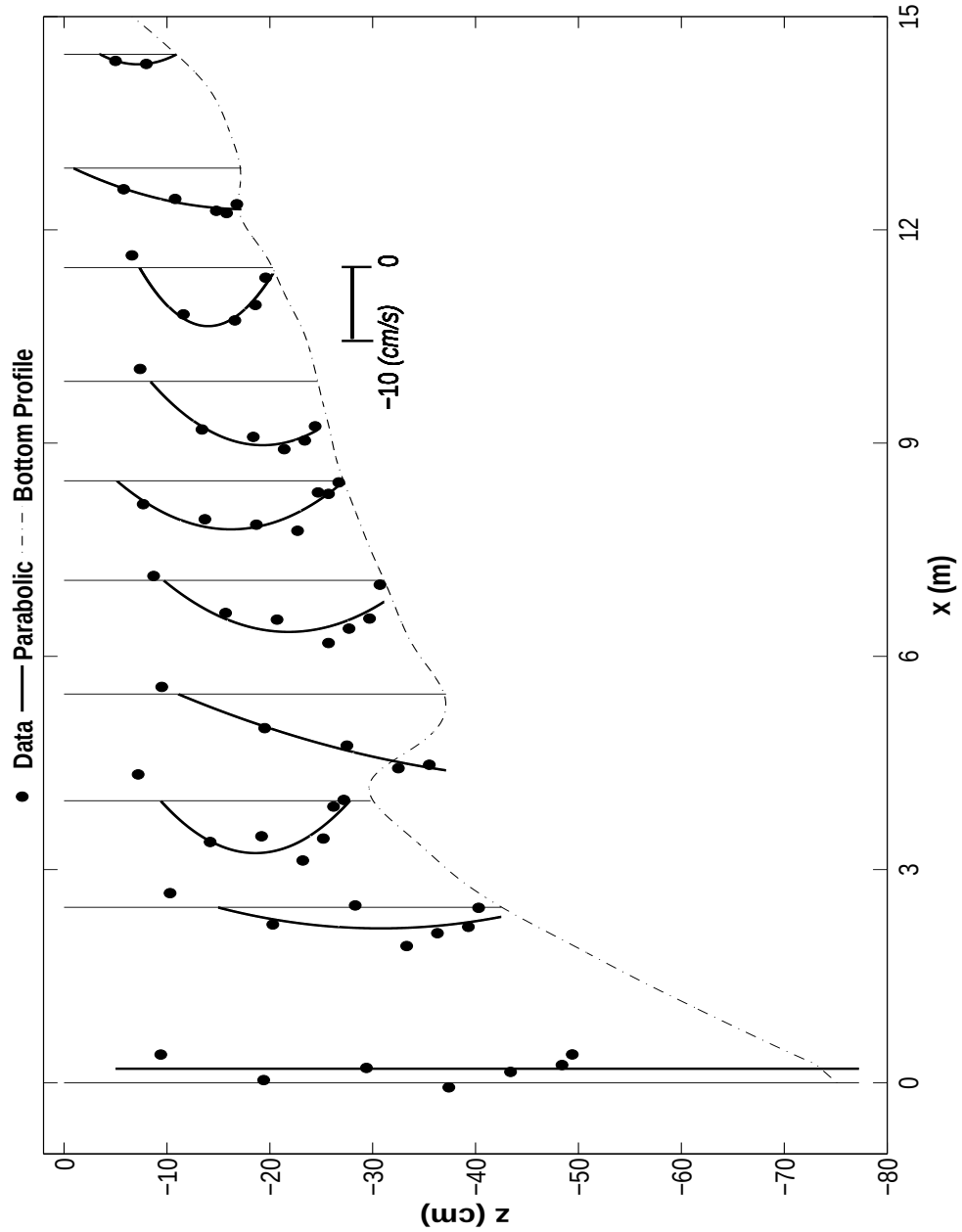

Figure 4.9: Measured and fitted parabolic profiles of mean $\overline{u}$ for plunging wave test.

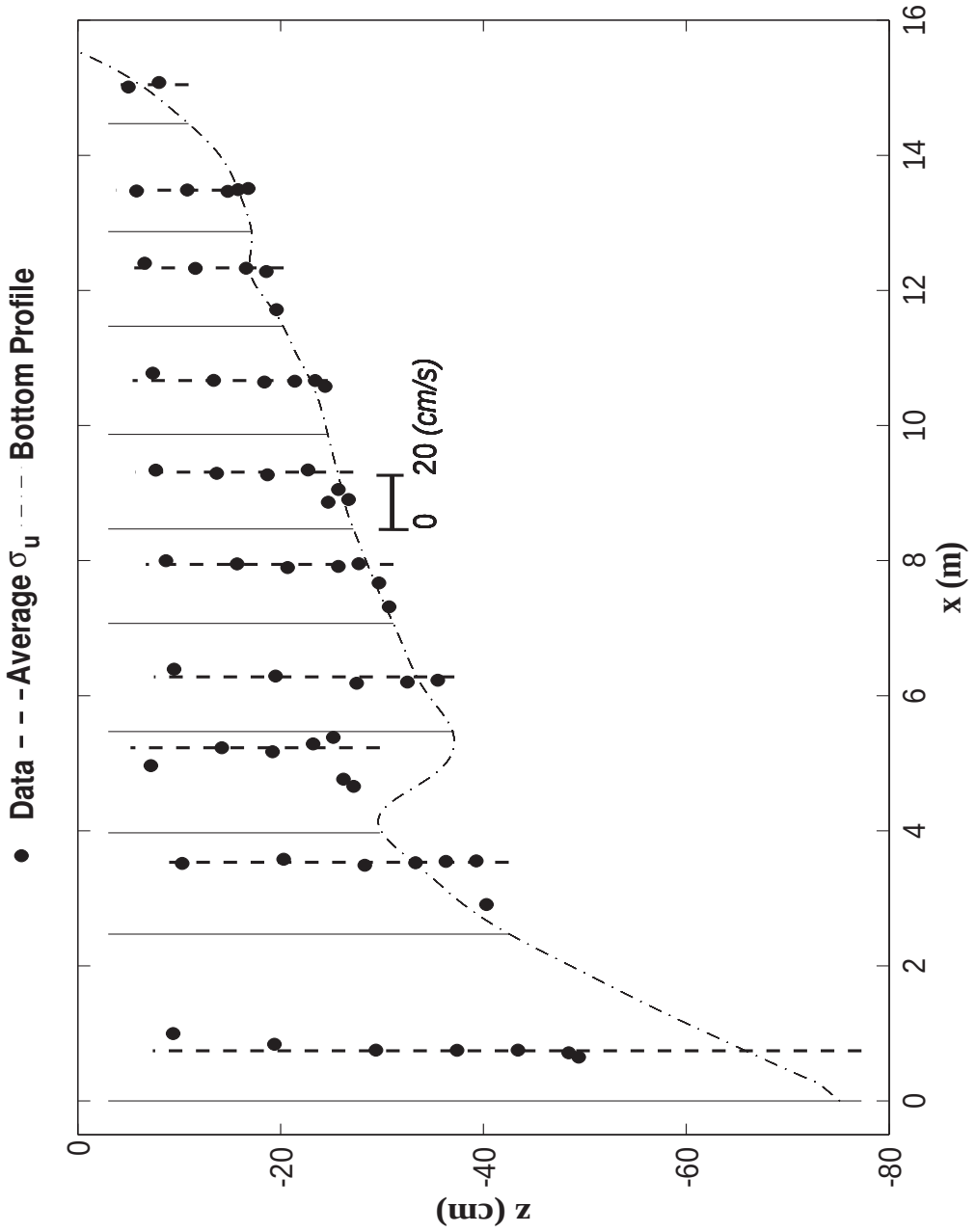

Figure 4.10: Measured and vertically averaged values of σ_u for plunging wave test.

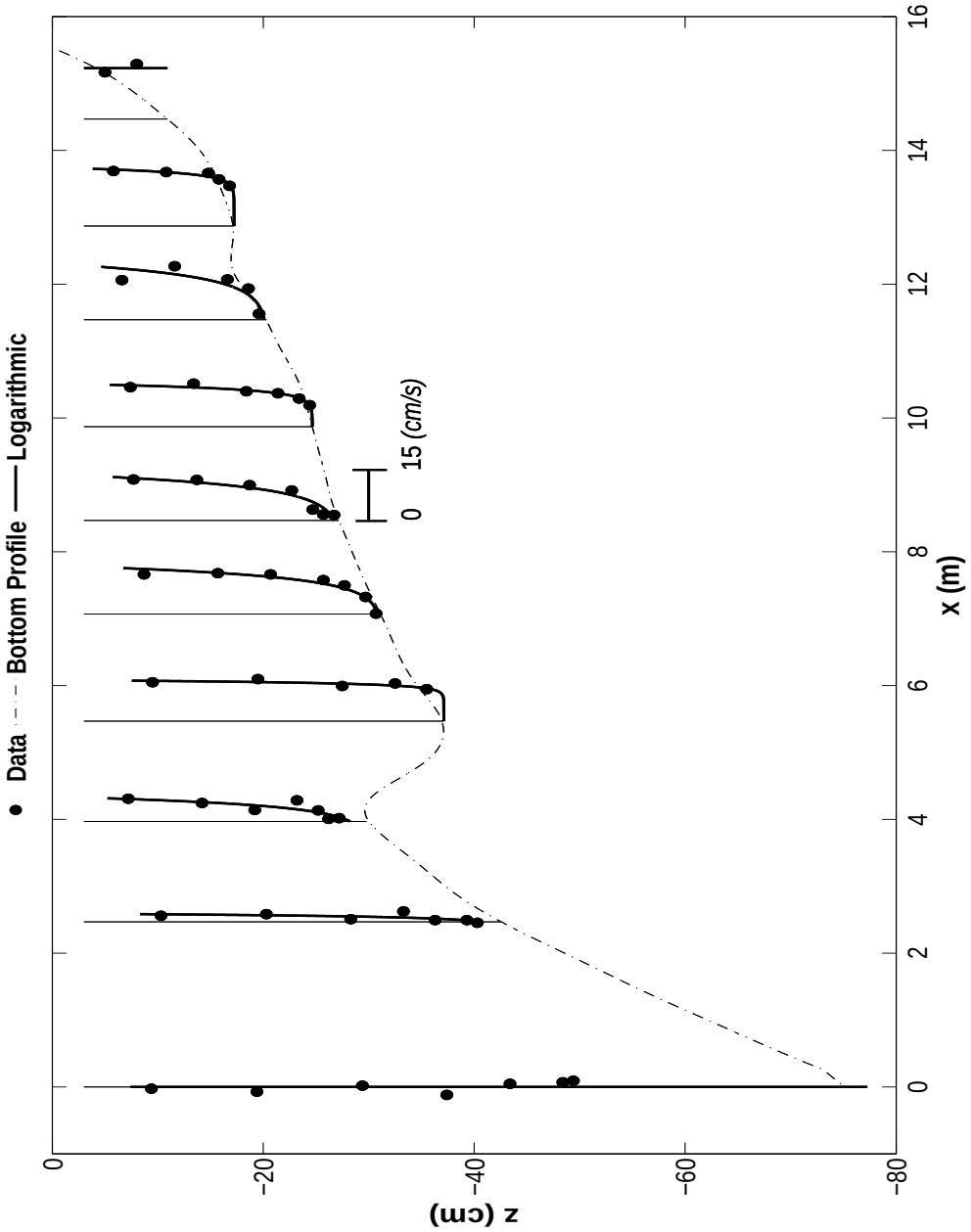

Figure 4.11: Measured and fitted logarithmic profiles of mean $\overline{v}$ for plunging wave test.

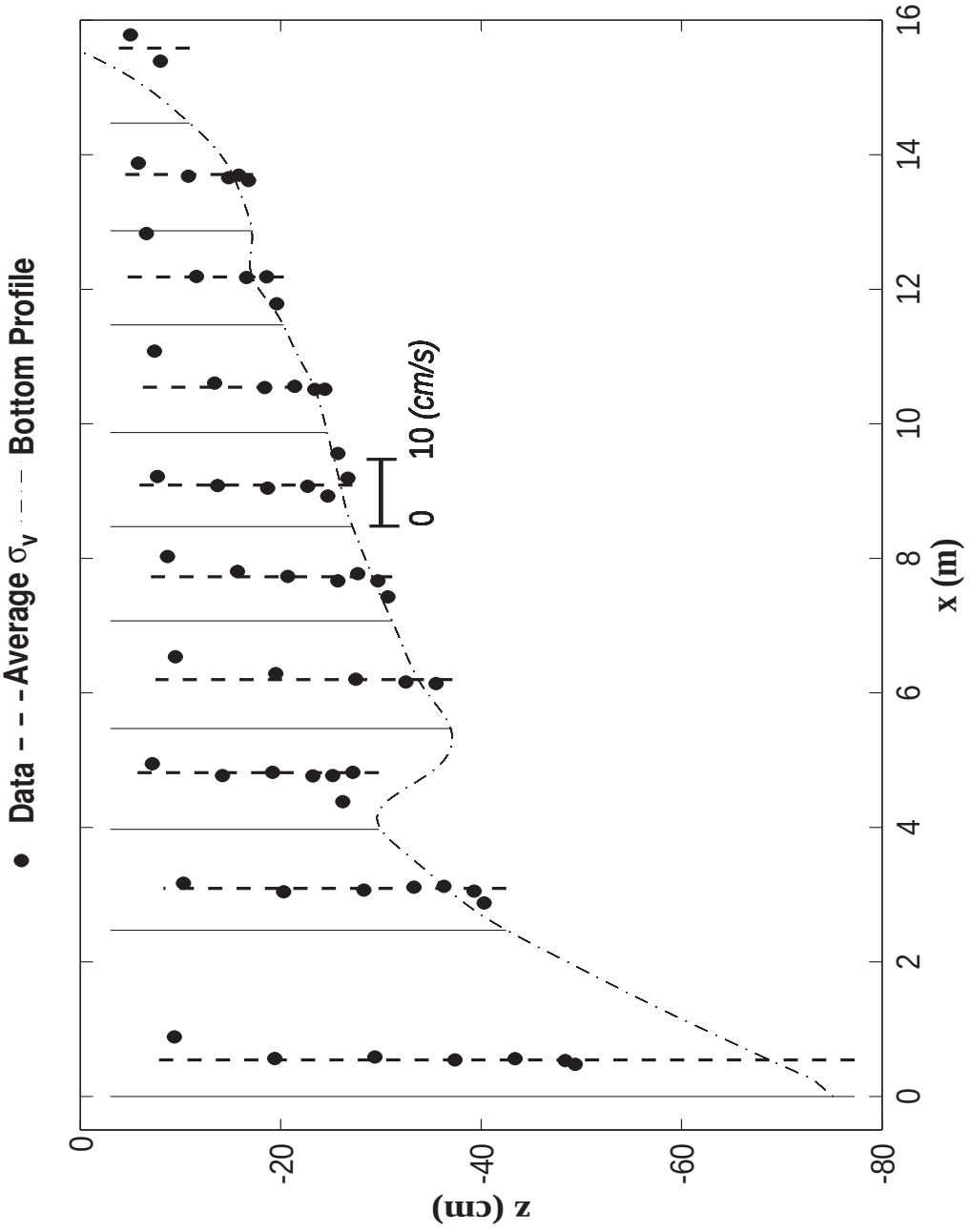

Figure 4.12: Measured and vertically averaged values of σ_v for plunging wave test.

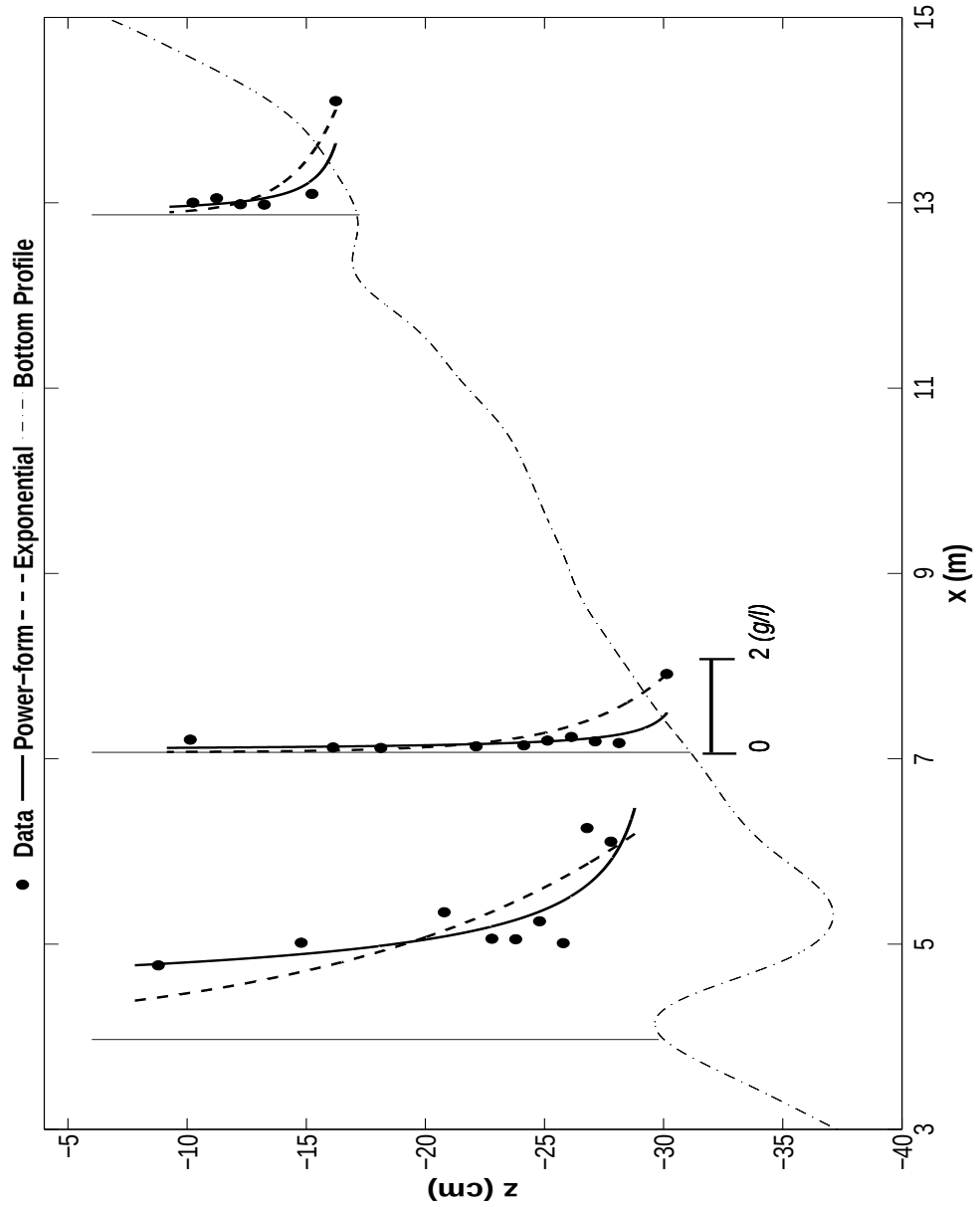

Figure 4.13: Measured and fitted power-form and exponential profiles of mean concentration $\bar{c}$ for plunging wave test.

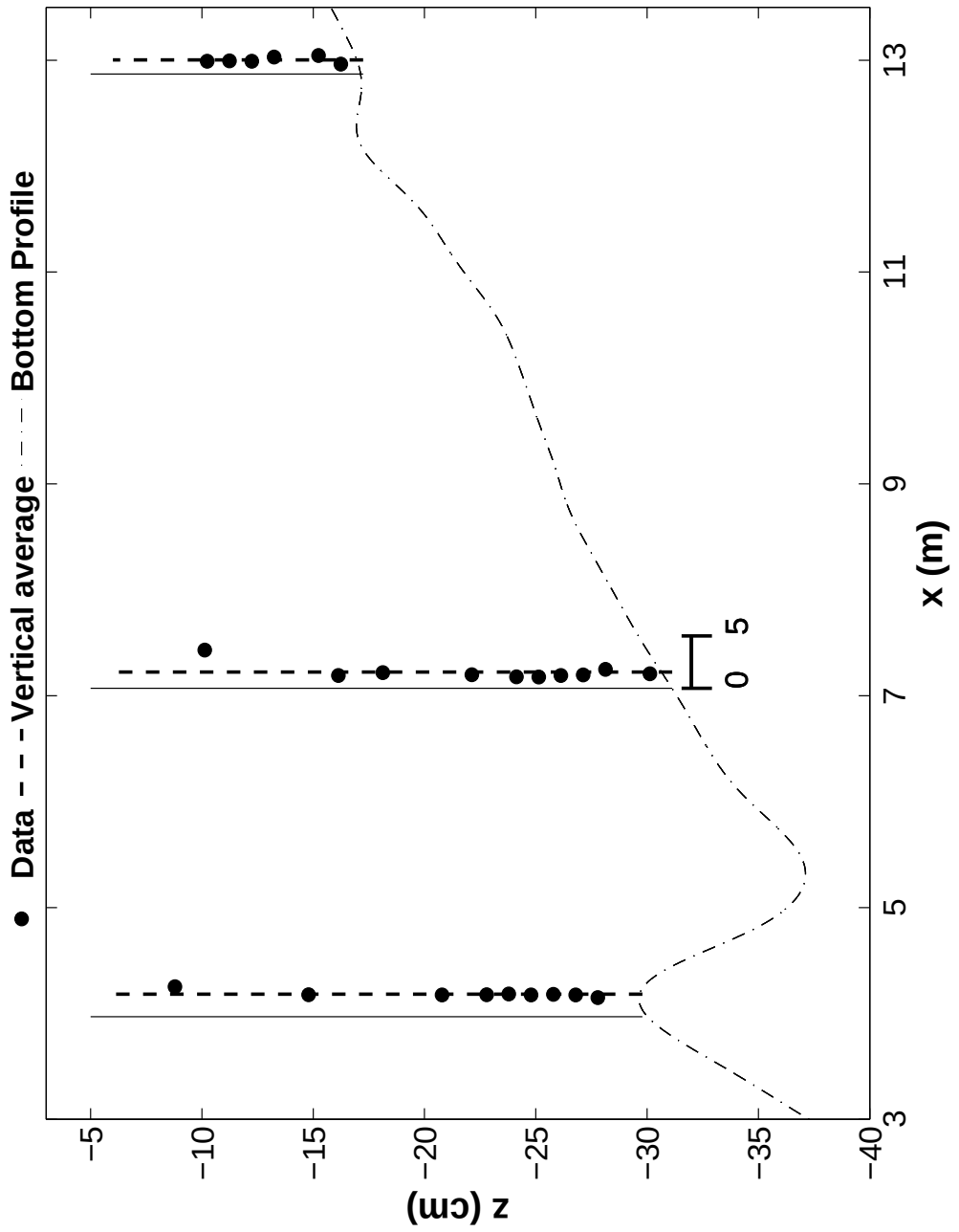

Figure 4.14: Measured and vertically averaged values of $\sigma_c/\bar{c}$ for plunging wave test.

4.3 Comparisons with Spilling Wave Data

Fig. 4.15 shows the measured and computed cross-shore variations of the mean and standard deviation of the free surface elevation η as well as the smoothed bottom elevation z_b for the spilling wave test. No bar was present in the spilling wave test. The time-averaged model overpredicts the wave setup $\bar{\eta}$ slightly and yields good agreement for σ_η partly because γ is calibrated for each test. The difference between IROLL = 0 and 1 is small in Fig. 4.15.

The number of iterations needed for convergence at each landward step are shown in Fig. 4.16. It is clearly seen that for the case where computations are done without adding the roller the convergence is reached in just 1 iteration whereas when the roller effects are added to the numerical model it takes as many as 10 iterations at some cross-shore locations to reach the specified convergence limit. The landward-marching computation stops at $x = 15.9$ m for IROLL = 0 and 1, landward of the still water shoreline located at $x = 15.5$ m.

Fig. 4.17 shows the computed cross-shore variations of n, Q, σ_* and a. The ratio n between the group and phase velocities in Eq. (2.8) approaches unity in very shallow water near the still water shoreline located at $x = 15.5$ m. The assumption of linear shallow-water wave theory used for Eqs. (2.17)–(2.19) is not very good in the offshore region of the spilling wave test with $T_p = 1.5$ s. The fraction Q of breaking waves in Eq. (2.37) increases gradually from zero at $x = 0$ and rapidly approaches unity near the shoreline. The ratio $\sigma_* = \sigma_\eta/\bar{h}$ in Eqs. (2.23) and (2.35) increases landward but is less than 0.6 in very shallow water because of the empirical modification described in relation to Eq. (2.39). The parameter a given by Eq. (2.39) is unity but becomes large in the region where the wave setup $\bar{\eta}$ becomes almost tangential to the bottom in Fig. 4.15. This parameter a increases D_B given in Eq. (2.36) and enables the computation to march well above the still water shoreline.

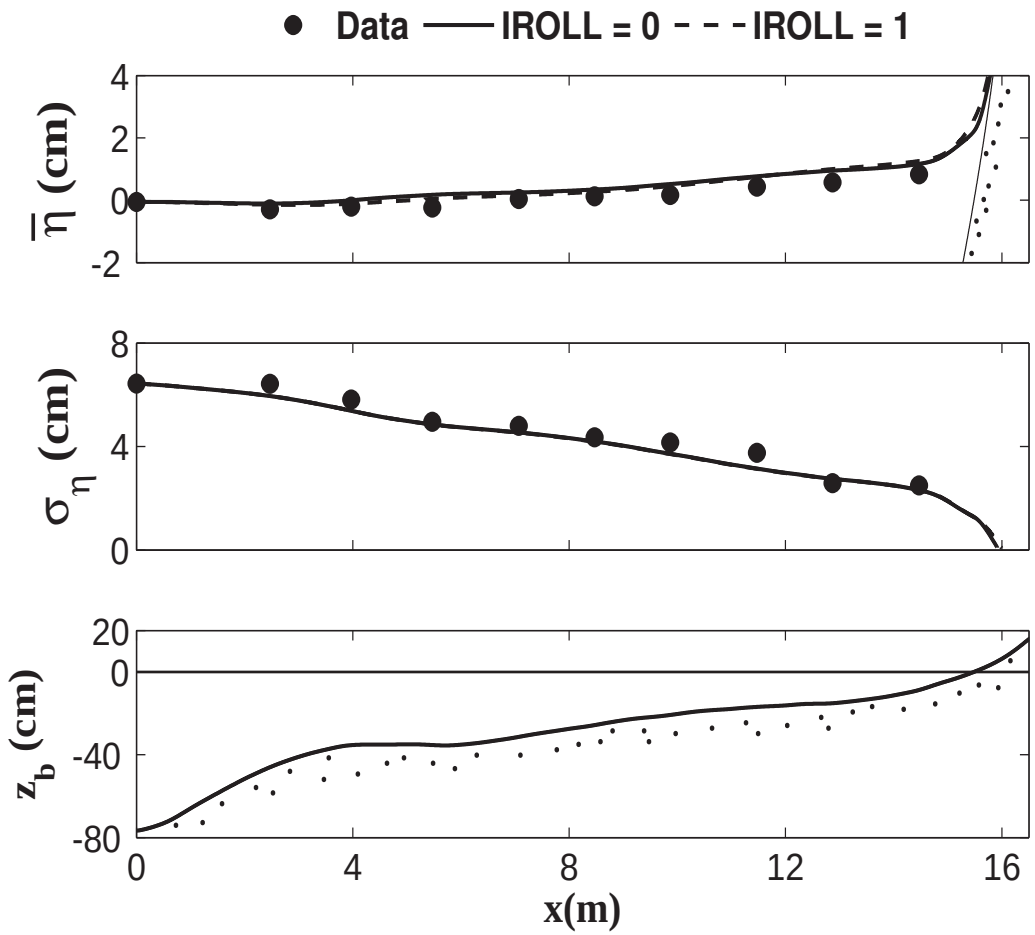

Figure 4.15: Measured and computed mean and standard deviation of η above bottom profile z_b for spilling wave test.

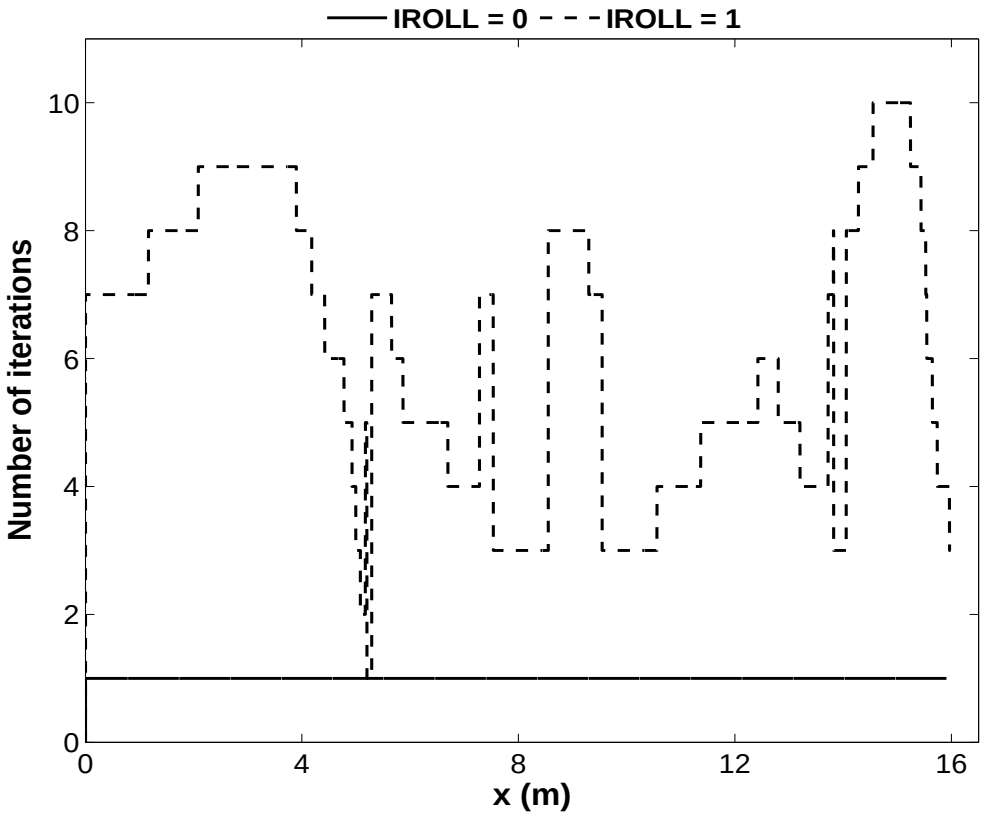

Figure 4.16: Number of iterations for computations with (IROLL = 1) and without roller (IROLL = 0) for spilling wave test.

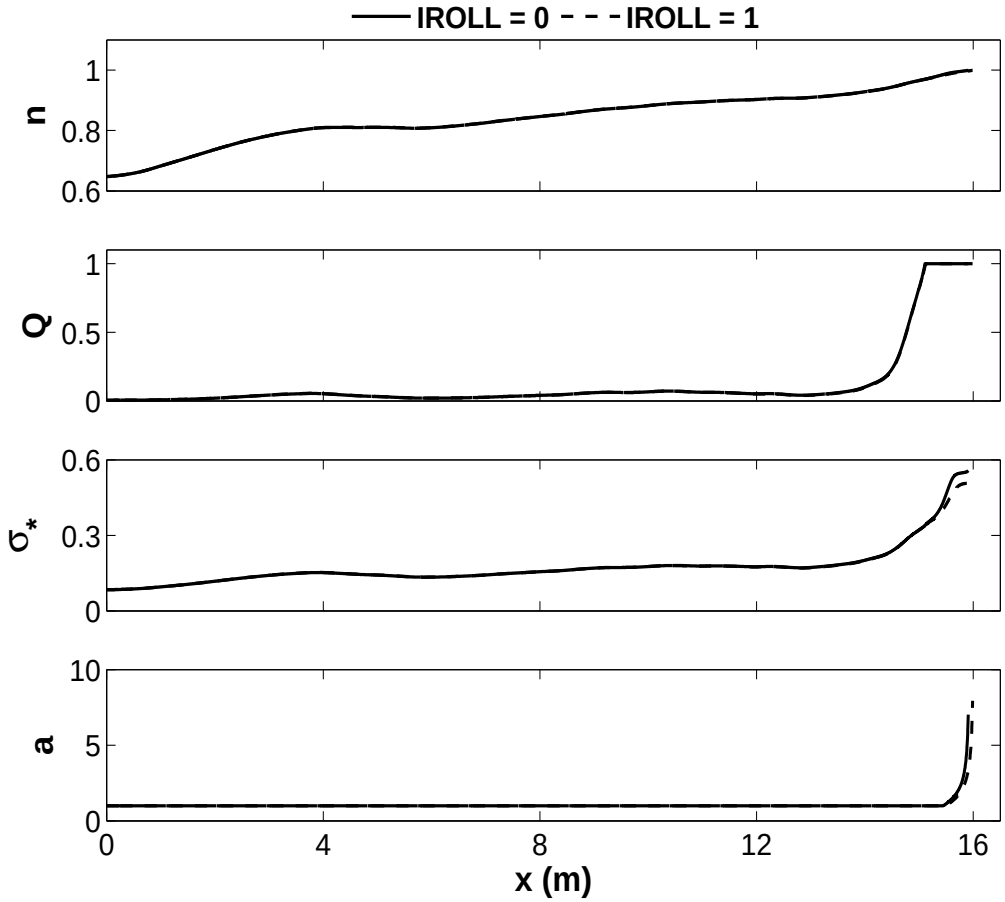

Figure 4.17: Computed cross-shore variations of n, Q, σ_* and a for spilling wave test.

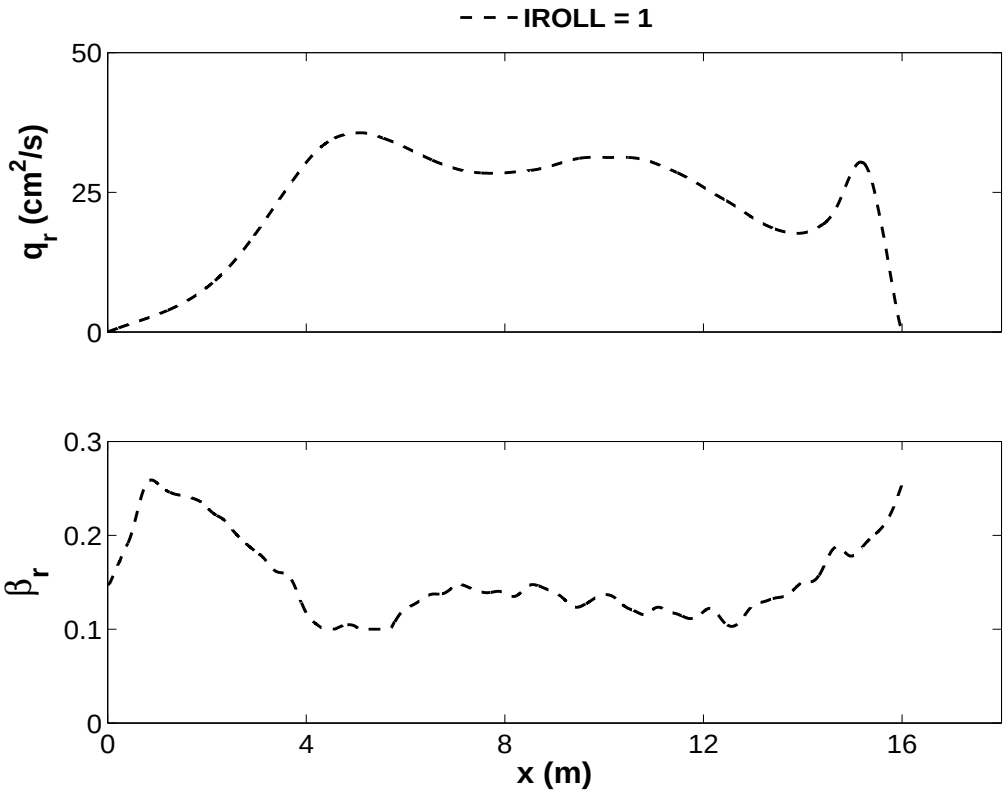

Figure 4.18: Computed roller volume flux q_r and roller slope β_r for IROLL = 1.

Fig. 4.18 shows the cross-shore variations of the roller volume flux q_r computed using Eq. (2.11) and the roller slope β_r given in Eq. (2.40). The computed q_r increases from zero at $x = 0$ and becomes the maximum landward of the zone of the bottom slope change in Fig. 4.15. The local bottom slope S_b can be inferred from $\beta_r = (0.1 + S_b) \geq 0.1$. The slight bottom undulation is also discernible in Fig. 4.18 but may have been caused by the numerical method used to smooth the measured rippled bottom profile.

Fig. 4.19 shows the computed cross-shore variations of S_{xx} and τ_{bx} in the cross-shore momentum equation in Eq. (2.1) where the superscript star indicates the variable divided by ρg. The roller effect included in IROLL = 1 causes the

increase and landward shift of the cross-shore radiation stress S_{xx} and the increase of the onshore bottom shear stress ($-\tau_{bx}$) which can be attributed to the increased return current $\overline{U}$ due to the onshore roller volume flux q_r.

Fig. 4.20 shows the measured and computed cross-shore variations of the mean and standard deviation of the cross-shore velocity U. The flux q_r included in Eq. (2.35) does not necessarily improve the agreement for $\overline{U}$ as has been pointed out by Kobayashi et al. (2005) for normally incident irregular waves. The numerical model overpredicts σ_U for the spilling wave test. The reason for this overprediction is not clear because Kobayashi et al. (2005) obtained better agreement for their normally-incident spilling and plunging wave tests.

Fig. 4.21 shows the computed cross-shore variations of G_{by}, S_{xy} and τ_{by} related to the longshore momentum equation in Eq. (2.2). The dimensionless function G_{by} given by Eq. (2.34) is found to be simplified as $G_{by} \simeq 1.16\overline{V}/\sigma_T$ within the error of about 20% for both IROLL = 0 and 1 as shown in Fig. 4.22. As a result, the longshore bottom stress τ_{by} is approximately proportional to the longshore current $\overline{V}$. The roller effect increases the longshore radiation stress S_{xy} and causes the cross-shore gradient of S_{xy} to become more uniform in the surf zone where $\tau_{by} = -dS_{xy}/dx$. Consequently, τ_{by} and $\overline{V}$ vary less across the surf zone for IROLL = 1.

Fig. 4.23 compares the measured and computed longshore currents. Only positive measured alongshore velocities are shown in Fig. 4.23 excluding the measured $\overline{V}$ = -2.72 cm/s at $x = 0$. The roller effect improves the agreement for $\overline{V}$. On the other hand, the standard deviation σ_V representing the longshore oscillatory velocity in Fig. 4.24 is less than the longshore current $\overline{V}$. The simple formula for σ_V in Eq. (2.21) predicts the landward decrease of σ_V with the decrease of $\sin\theta$ due to wave refraction. To the contrary, the measured σ_V increases landward. The time series and spectra of the measured longshore velocity v were presented by Wang et

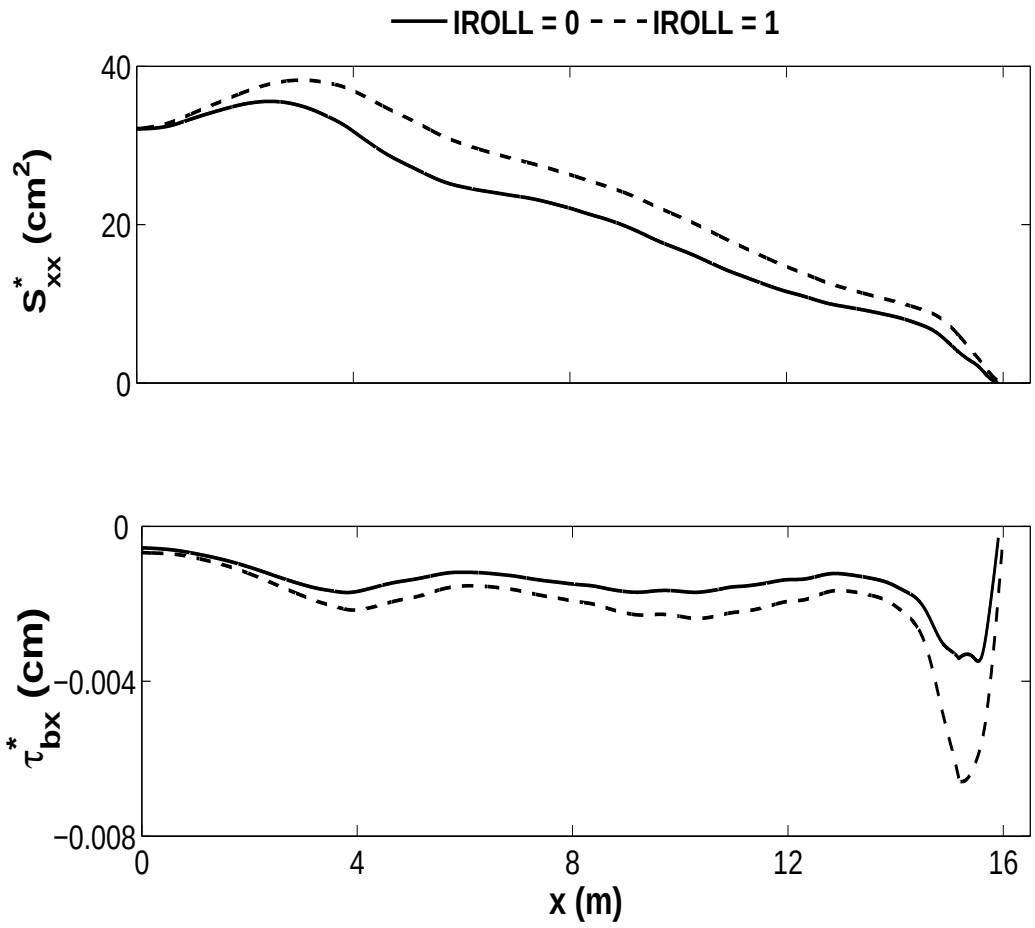

Figure 4.19: Computed cross-shore radiation stress $S_{xx} = \rho g S^*_{xx}$ and bottom shear stress $\tau_{bx} = \rho g \tau^*_{bx}$ for spilling wave test.

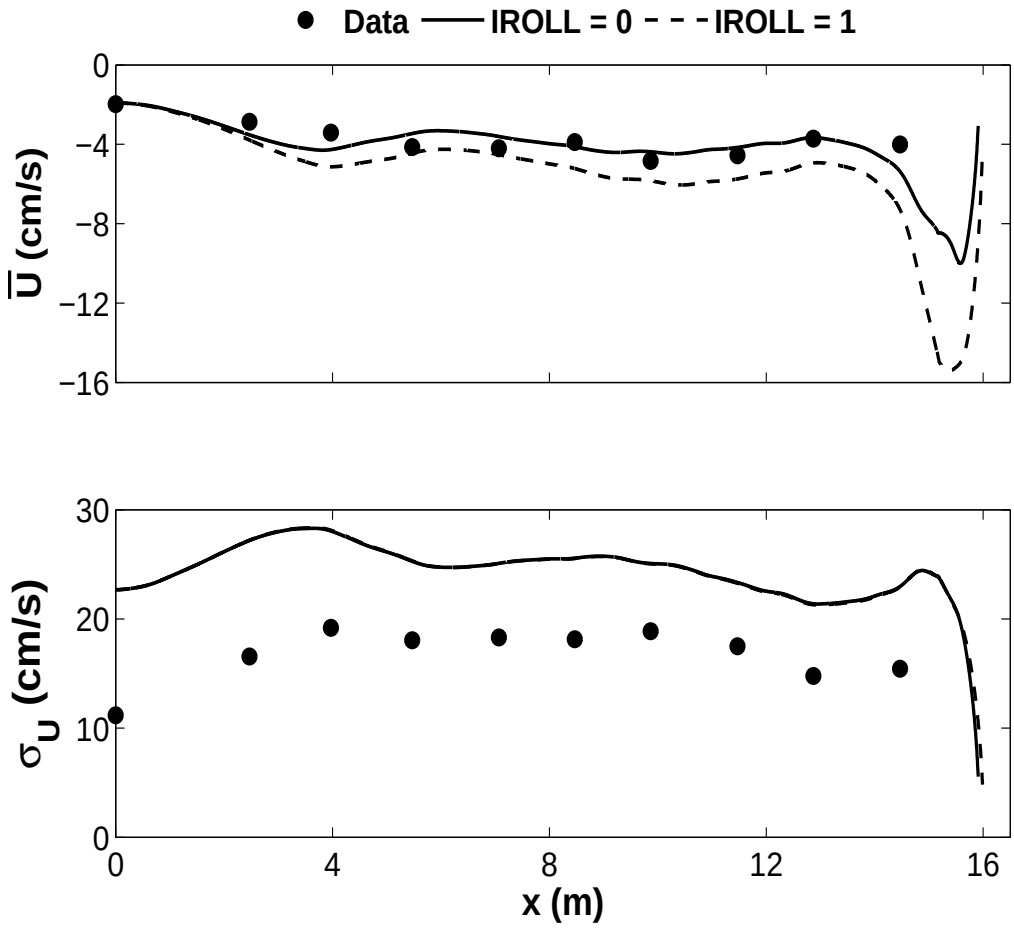

Figure 4.20: Measured and computed mean and standard deviation of U for spilling wave test.

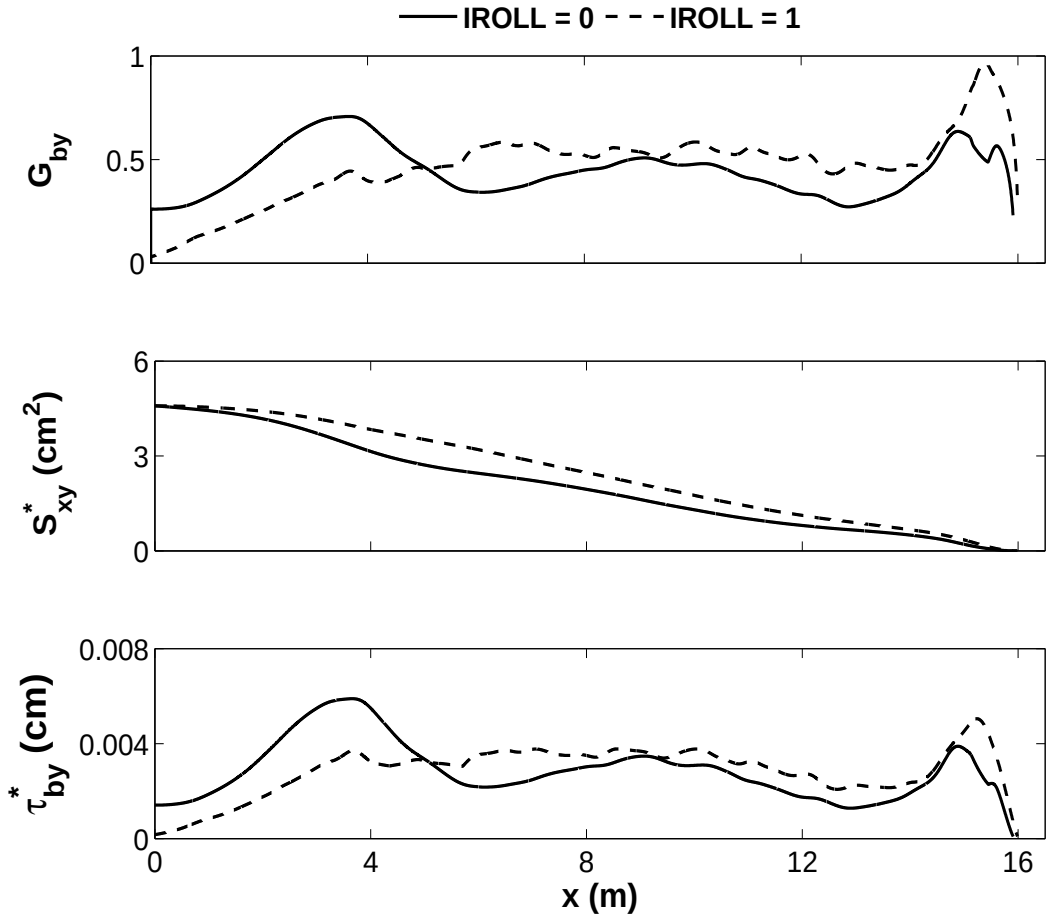

Figure 4.21: Computed dimensionless function G_{by}, longshore radiation stress $S_{xy} = \rho g S^*_{sy}$ and bottom shear stress $\tau_{by} = \rho g \tau^*_{by}$.

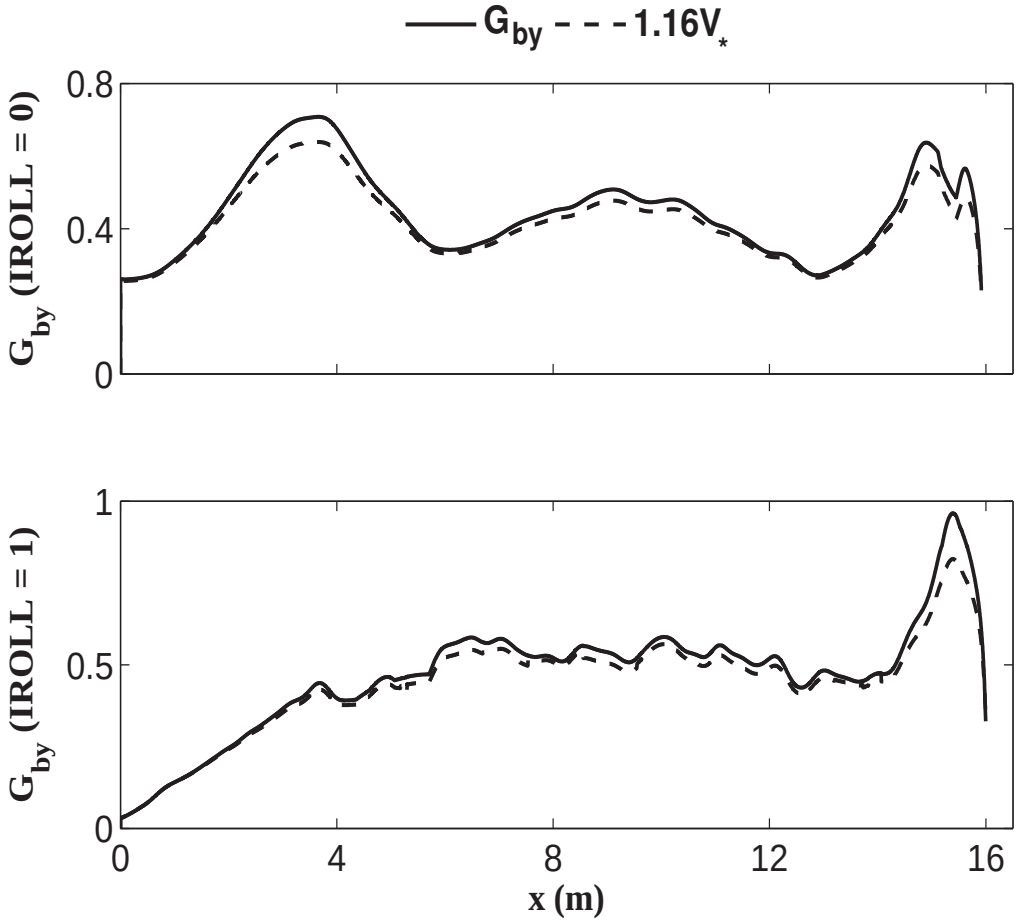

Figure 4.22: Dimensionless function G_{by} calculted by Eq. 2.34 and by approximate expression $1.16V^*$ where $V^* = \overline{V}/\sigma_T$ for IROLL = 0 (top) and 1 (bottom) for spilling wave test.

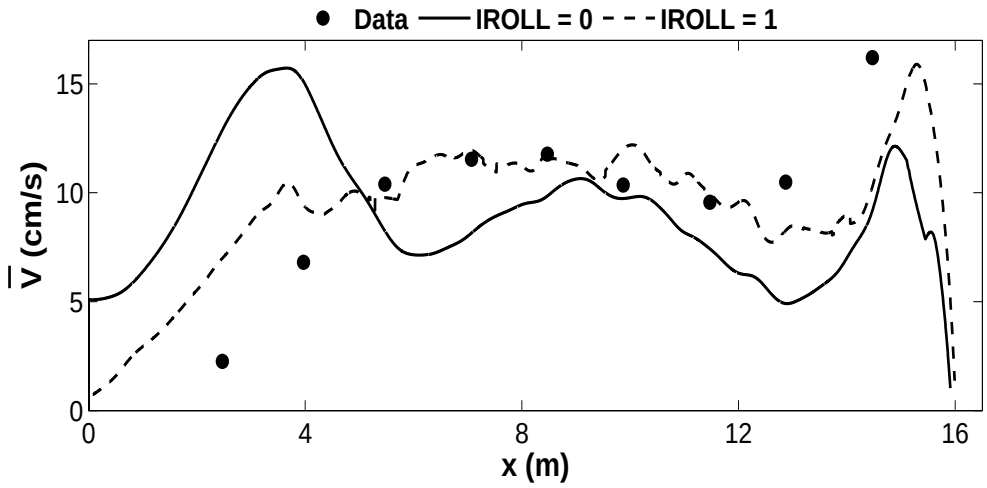

Figure 4.23: Measured and computed longshore current $\overline{V}$ for spilling wave test.

al. (2002a) where the low frequency components of v were appreciable. The landward increase of σ_V may have been caused partly by shear waves where Noyes et al. (2005) observed the landward increase of shear wave velocity fluctuations on a natural beach.

Fig. 4.25 shows the computed cross-shore variations of F_x, D_B and D_f in the energy equation, Eq. (2.3). The cross-shore energy flux F_x decreases landward due to wave energy dissipation. The value of F_x at the still water shoreline located at $x = 15.5$ m is used in Eq. (2.41) to estimate the reflection coefficient at $x = 0$ listed in Table 4.1. The energy dissipation rate D_f due to bottom friction is much smaller than the rate D_B due to wave breaking. The ratio D_f/D_B is of the order of 0.1. Kobayashi et al. (2005) measured the turbulent velocity variances near the bottom and showed that the measured time-averaged turbulent velocity was similar to the turbulent velocity $u'_f = (D_f/\rho)^{1/3}$. The computed D_f shown in Fig. 4.25 yields the turbulent velocity u'_f of about 7 cm/s which is significantly larger than the estimated fall velocity $w_f = 1.65$ cm/s of the sand used in these tests as shown

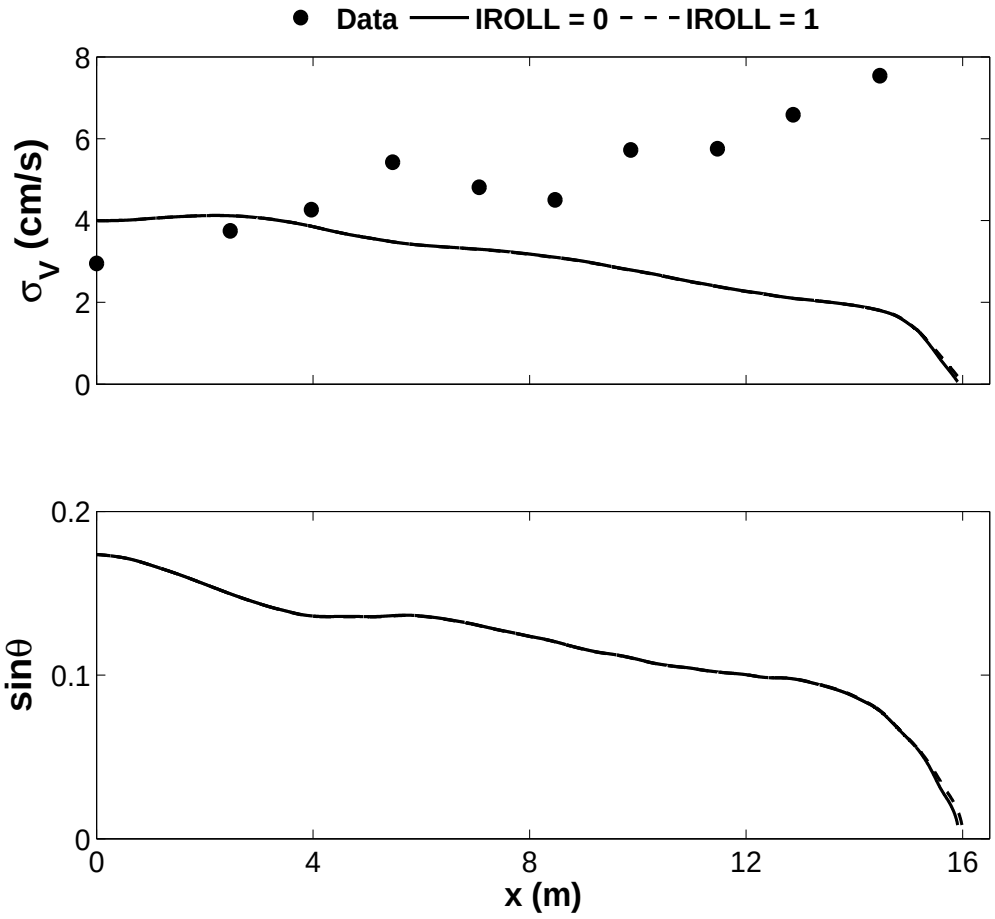

Figure 4.24: Measured and computed standard deviation of V as well as computed $\sin\theta$ for spilling wave test.

in Fig. 4.26. This implies significant sediment suspension near the bottom as shown in Fig. 4.6.

Fig. 4.27 compares the measured and computed suspended sediment volume $\overline{V_c}$ per unit area. The agreement within a factor of about two is similar to the comparisons with three tests made by Kobayashi et al. (2005) for normally incident waves. The computed value of $\overline{V_c}$ is based on Eq. (2.42) with $e_B = 0.002$, $e_f = 0.01$, $s = 2.65$ and $w_f = 1.65$ cm/s where $D_r = D_B$ for IROLL = 0. The use of $e_B = 0.005$ results in the overprediction of $\overline{V_c}$. Since D_f/D_B is of the order of 0.1 in Fig. 4.25, the contribution to $\overline{V_c}$ by $e_f D_f$ in Eq. (2.42) is of the order of 1/3, indicating that the effect of bottom friction on sediment suspension is not negligible. The cross-shore variation patterns of τ_{by}, $\overline{V}$ and $\overline{V_c}$ in Figs. 4.21, 4.23 and 4.27 respectively, appear very similar. This similarity is explained later in Chapter 5 in relation to the longshore sediment transport rate.

Fig. 4.28 compares the measured and computed offshore suspended sediment transport rate $q_{\rm off}$ due to undertow current. The measured $q_{\rm off}$, which is positive offshore, is obtained by integrating $(-\bar{u}\bar{c})$ analytically in the region of $\bar{u} < 0$ and $z_m \geq 1$ cm where use is made of the fitted profiles of $\bar{u}$ and $\bar{c}$ given in Eqs. (4.1) and (4.6). The computed $q_{\rm off}$ is given by $q_{\rm off} = (-0.9\overline{U}\ \overline{V_c})$ on the basis of the cross-shore suspended sediment transport data analysis by Kobayashi et al. (2005) where the coefficient 0.9 does not change the agreement in Fig. 4.28. In view of the comparisons in Figs. 4.20 and 4.27, the disagreement in Fig. 4.28 results mostly from the error of the computed $\overline{V_c}$. Kobayashi et al. (2005) analyzed the onshore suspended sediment transport using the synchronous measurements of u and c which were not made in the present tests. Kobayashi et al. (2005) proposed a formula for the onshore suspended sediment transport rate $q_{\rm on} = 0.8\ \sigma_* \sigma_U \overline{V_c}$. The computed $q_{\rm on}$ using this formula is found to be similar to $q_{\rm off}$ shown in Fig. 4.28. It is not possible at present to explain why the beach shown in Fig. 4.15 was quasi-equilibrium.

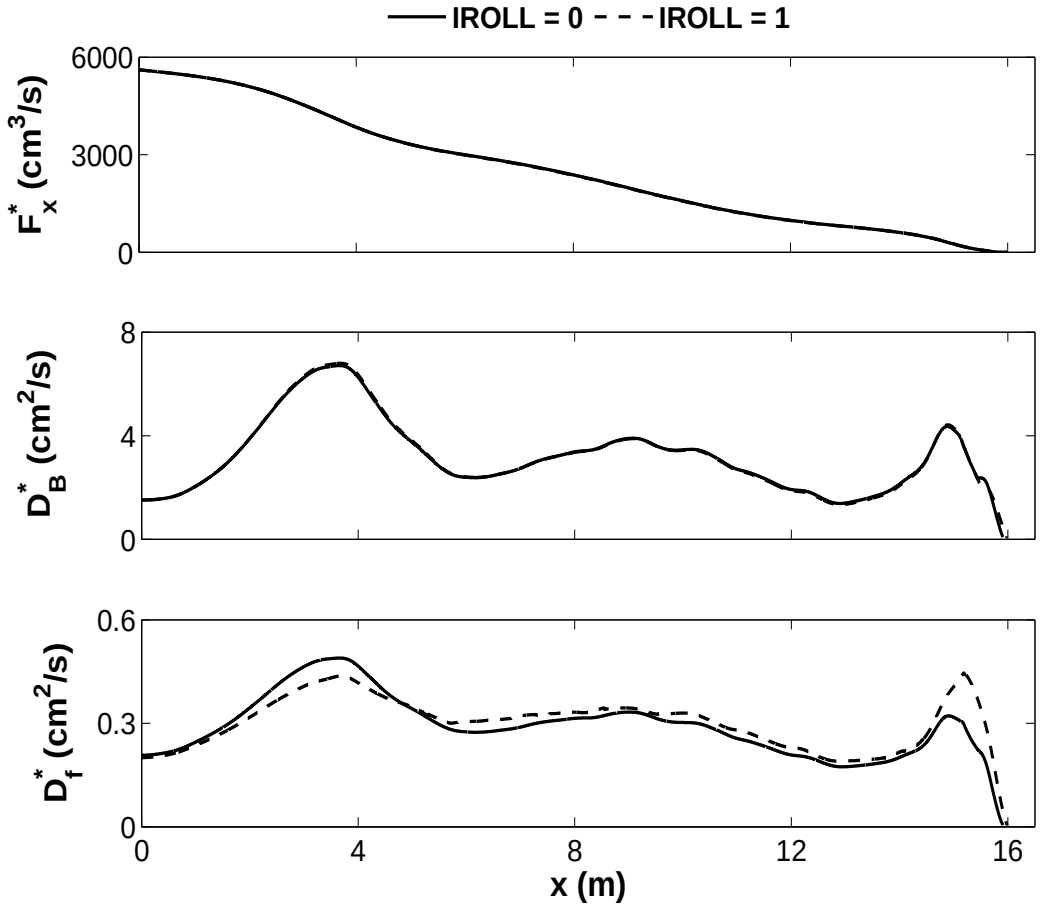

Figure 4.25: Computed cross-shore energy flux $F_x = \rho g F_x^*$, and energy dissipation rates $D_B = \rho g D_B^*$ and $D_f = \rho g D_f^*$ due to wave breaking and bottom friction for spilling wave test.

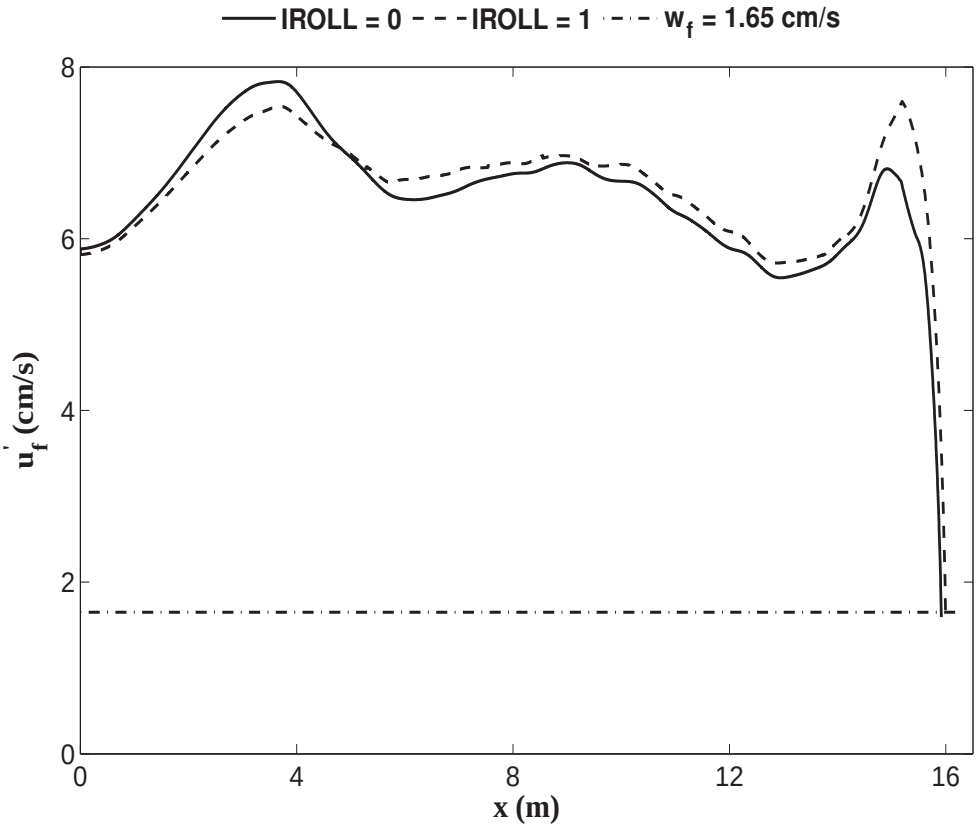

Figure 4.26: Computed turbulent velocity u'_f and estimated sediment fall velocity w_f for spilling wave test.

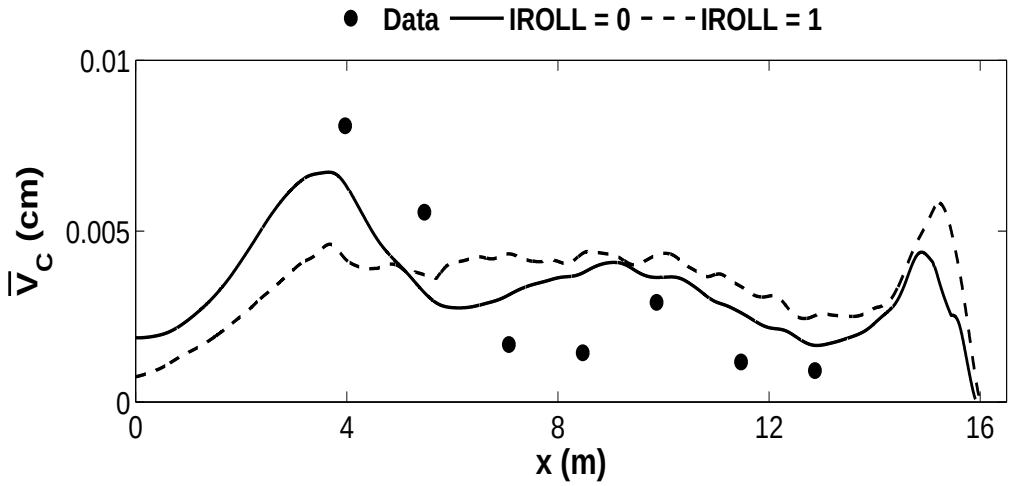

Figure 4.27: Measured and computed suspended sediment volume $\overline{V_c}$ per unit horizontal area for spilling wave test.

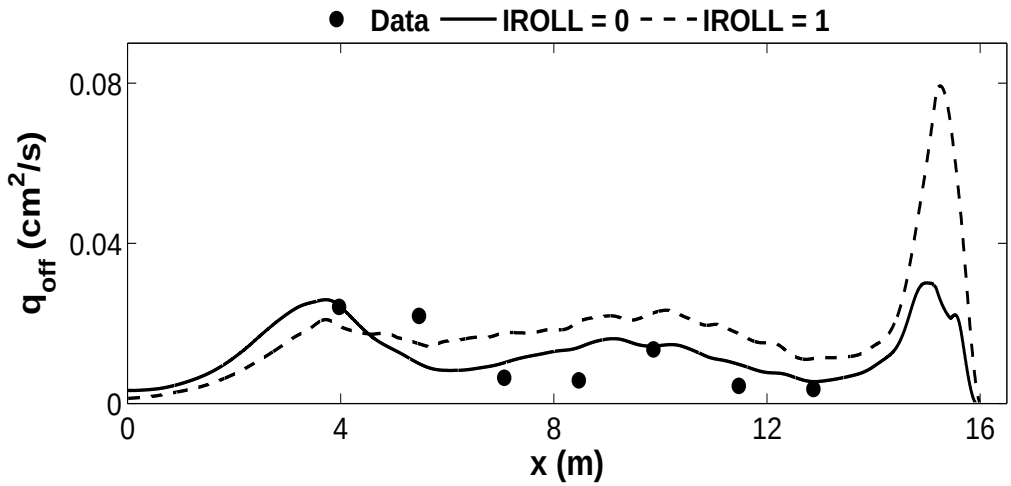

Figure 4.28: Measured and computed offshore suspended sediment transport rate q_{off} due to offshore current for spilling wave test.

4.4 Comparisons with Plunging Wave Data

The measured and computed cross-shore variations of the mean and standard deviation of the free surface elevation η as well as the smoothed elevation z_b for the plunging wave test is shown in Fig. 4.29. A bar was formed under the plunging waves. The wave setup $\overline{\eta}$ is slightly overpredicted whereas due to the calibration of γ, good agreement is achieved for σ_η. One noticeable difference between the σ_η plots for the spilling and plunging wave tests is that for the plunging waves σ_η increases from $x = 0$ to the bar crest before the landward decrease.

Fig. 4.30 shows the computed (IROLL = 0 and 1) cross-shore variations of n, Q, σ_* and a for the plunging wave test. The ratio n is almost equal to 1 right from the starting of the surf zone because the spectral peak period $T_p = 3.0$ s was twice as large as $T_p = 1.5$ s for the spilling waves. The fraction Q of breaking waves shows an increase at around $x = 4$ and 12 m due to the depth decrease at the bar crest and a small hump, before rapidly approaching unity near the shoreline like in the spilling case. The ratio σ_* and parameter a show similar patterns as in the spilling case.

The roller volume flux q_r and the roller slope β_r are shown in Fig. 4.31. The computed q_r increases from zero at $x = 0$, becomes the maximum just above the crest of the bar and then gradually decreases as the roller moves landward. The computed q_r is larger for the plunging waves than that for the spilling waves shown in Fig. 4.18. The β_r plot can be used to infer the bottom slope S_b as $\beta_r = (0.1 + S_b) \geq 0.1$.

Fig. 4.32 shows the computed cross-shore variations of cross-shore radiation stress S_{xx} and bottom stress τ_{bx}. As with the spilling case, the roller effect in IROLL = 1 causes the increase and landward shift of S_{xx}. The increase of the onshore bottom shear stress $(-\tau_{bx})$ for IROLL = 1 can be attributed to the increased return current $\overline{U}$ due to the onshore volume flux q_r. The increase of $(-\tau_{bx})$ on the bar crest and near the shoreline is related to the cross-shore variation of $\overline{U}$.

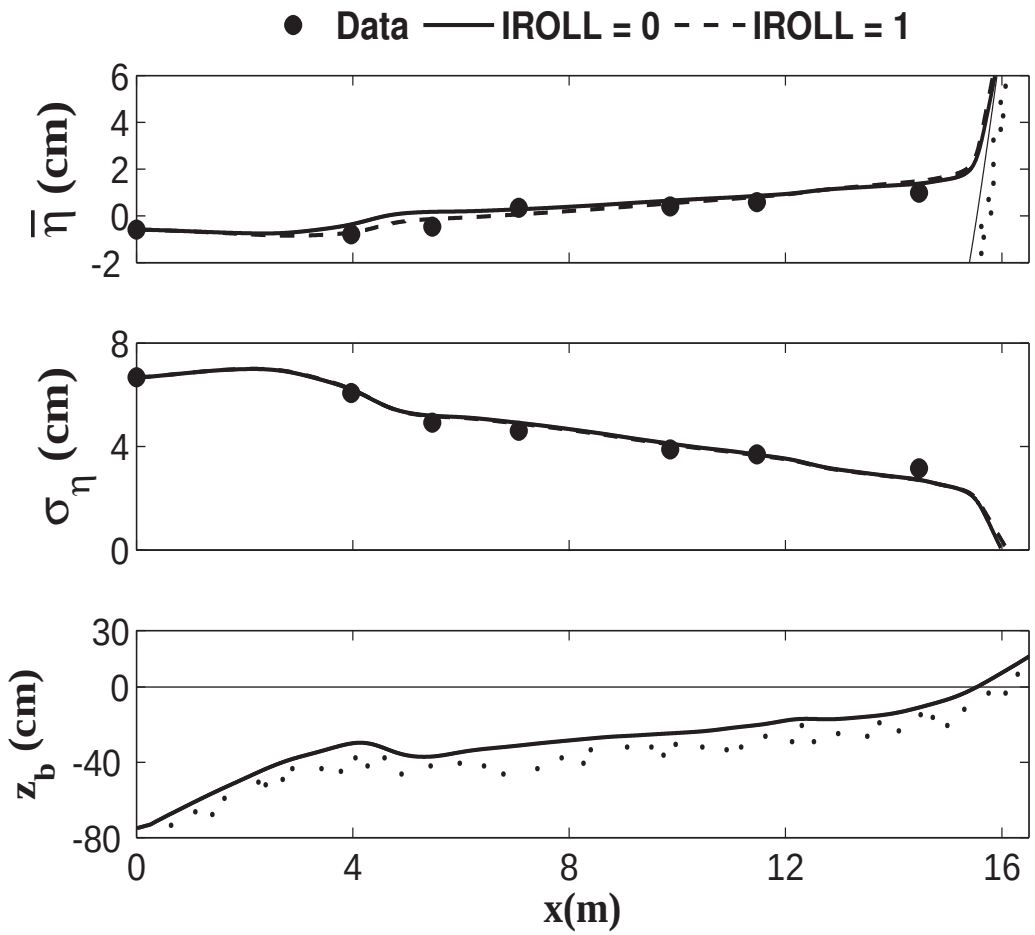

Figure 4.29: Measured and computed mean and standard deviation of η above bottom profile z_b for plunging wave test.

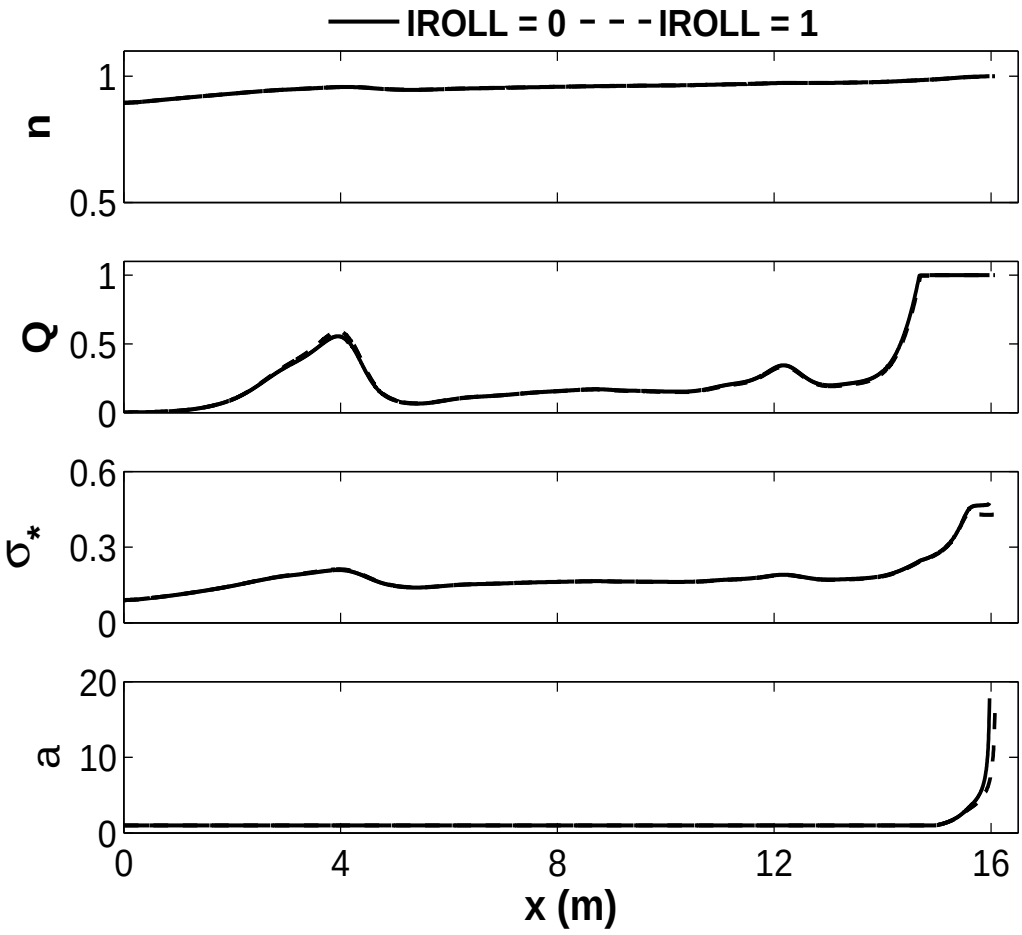

Figure 4.30: Computed cross-shore variations of n, Q, σ_* and a for plunging wave test.

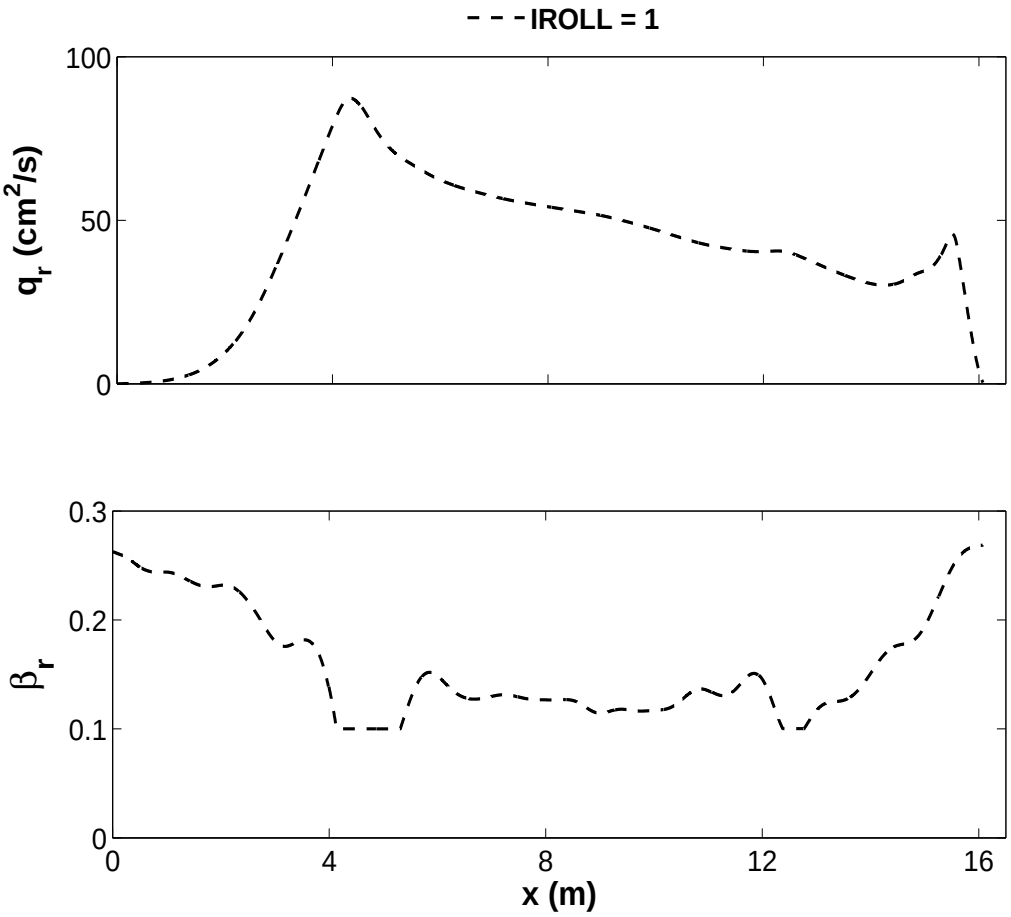

Figure 4.31: Computed roller volume flux q_r and roller slope β_r for IROLL = 1 for plunging wave test.

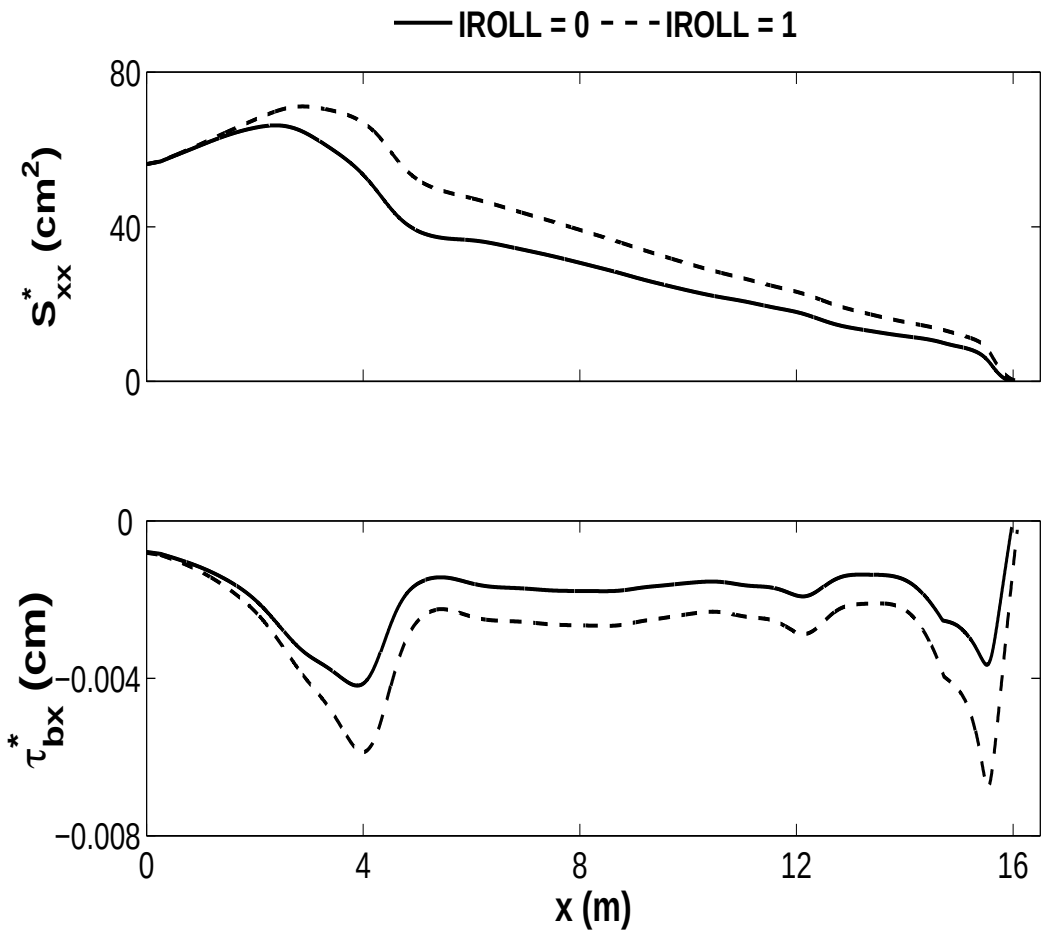

Figure 4.32: Computed cross-shore radiation stress $S_{xx} = \rho g S^*_{xx}$ and bottom shear stress $\tau_{bx} = \rho g \tau^*_{bx}$ for plunging wave test.

Fig. 4.33 shows the measured and computed cross-shore variation of undertow current $\overline{U}$ and the standard deviation of the cross-shore velocity U for the plunging wave test, where the measured $\overline{U} = 1.98$ cm/s at $x = 0$ m is not shown in the figure. The agreement for the plunging case is not as good as that for the spilling case. No velocity data was available near the still water shoreline where the computed undertow current velocity is maximum. The model overpredicts the σ_U for the plunging case as well.

Fig. 4.34 shows the computed cross-shore variations for G_{by}, S_{xy} and τ_{by} for the plunging wave test. As shown in Fig. 4.35 the dimensionless function G_{by} can be simplified as $G_{by} \approx 1.16\overline{V}/\sigma_T$ within as error of about 20% for both IROLL = 0 and 1 like the spilling case. The addition of roller effect increases the longshore radiation stress S_{xy}. The approximate expression for G_{by} indicates that the longshore bottom stress is approximately proportional to the longshore current $\overline{V}$. The value of τ_{by} for the plunging case is more than that in the spilling case which can be attributed to the larger longshore current $\overline{V}$ for the plunging case as shown in Fig. 4.36.

The measured and computed longshore currents are shown in Fig. 4.36. The computation with the roller effect gives a better agreement. Partly due to larger roller volume flux, the value of $\overline{V}$ for the plunging case tends to be larger that that of the spilling case. The landward decrease of σ_V with the decrease of $\sin\theta$ due to wave refraction is shown in Fig. 4.37 which is contrary to the measured increase of σ_V landward as explained for the spilling case.

The computed cross-shore variations of the energy flux F_x and energy dissipation rates D_B and D_f for the plunging wave test are shown in Fig. 4.38. F_x decreases landward due to wave energy dissipation. Majority of the energy dissipation due to wave breaking and bottom friction occurs over the bar and is larger than that for the spilling case. The computed D_f yields a turbulent velocity u'_f of approximately 8 cm/s as shown in Fig. 4.39 which is larger than the estimated

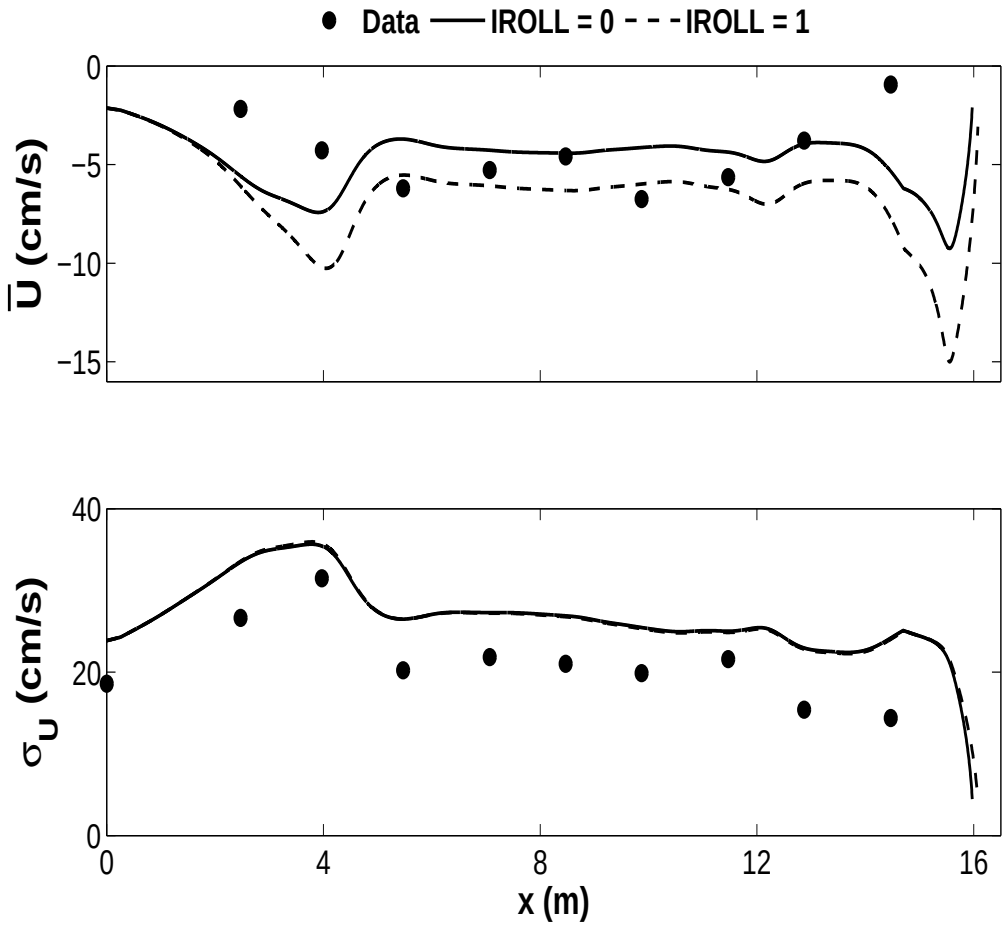

Figure 4.33: Measured and computed mean and standard deviation of U for plunging wave test.

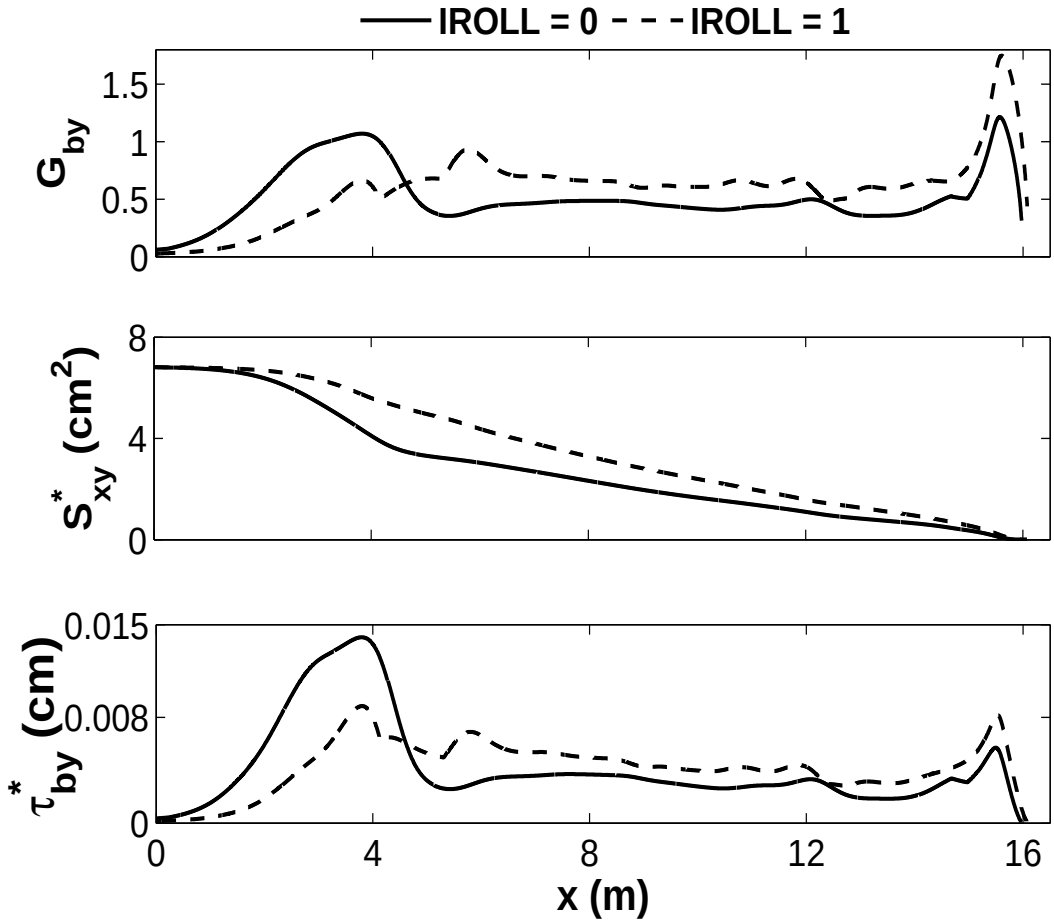

Figure 4.34: Computed dimensionless function G_{by}, longshore radiation stress $S_{xy} = \rho g S^*_{sy}$ and bottom shear stress $\tau_{by} = \rho g \tau^*_{by}$ for plunging wave test.

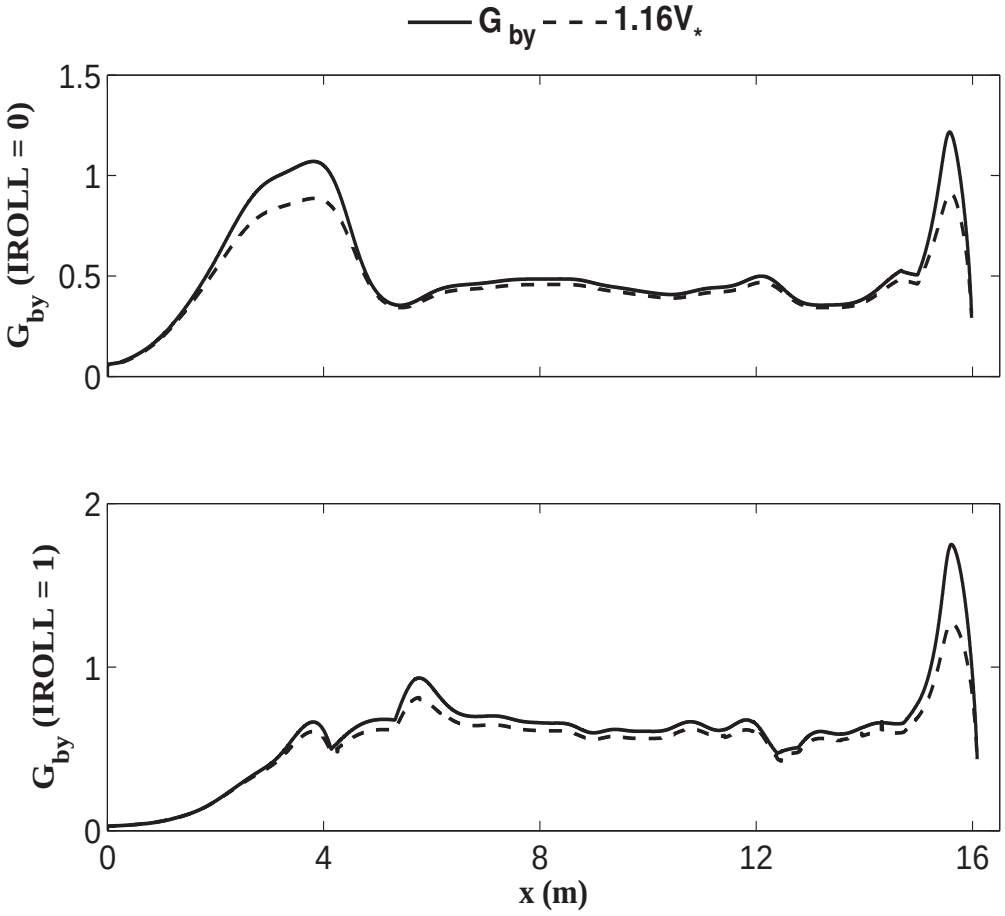

Figure 4.35: Dimensionless function G_{by} calculated by Eq. 2.34 and by approximate expression $1.16V^*$ where $V^* = \bar{V}/\sigma_T$ for IROLL = 0 (top) and 1 (bottom) for plunging wave test.

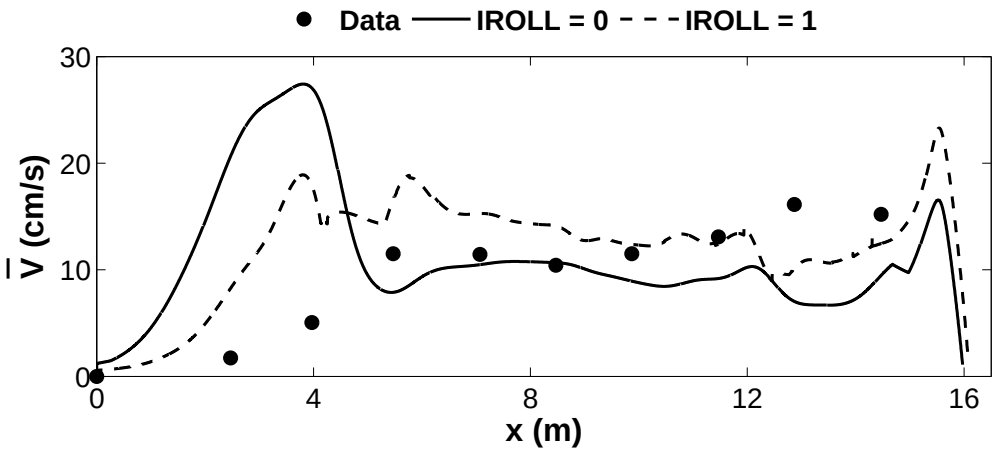

Figure 4.36: Measured and computed longshore current $\overline{V}$ for plunging wave test.

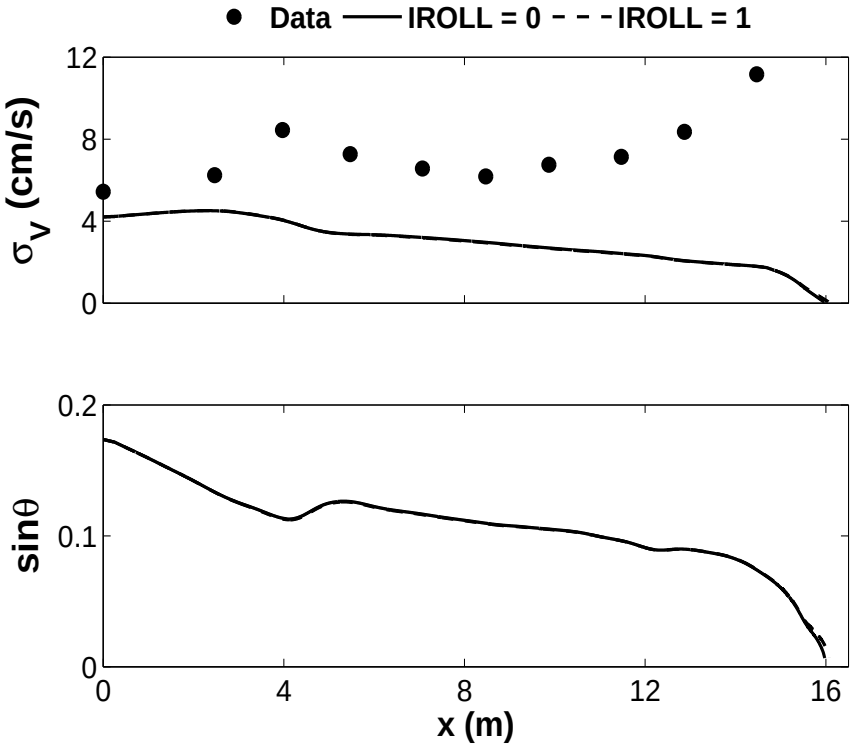

Figure 4.37: Measured and computed standard deviation of V as well as computed $\sin\theta$ for plunging wave test.

sediment fall velocity w_f, implying significant suspension of sediment.

Fig. 4.40 shows the measured and computed suspended sediment volume $\overline{V_c}$ per unit area. The computed value of $\overline{V_c}$ is roughly twice as large as that computed for the spilling case. Like the spilling case the cross-shore variation patterns of τ_{by}, $\overline{V}$ and $\overline{V_c}$ in Figs. 4.34, 4.36 and 4.40 respectively, appear very similar.

Fig. 4.41 compares the measured and computed offshore suspended sediment transport rate q_{off} due to undertow current. Comparing Figs. 4.28 and 4.41, the plunging waves increase q_{off} mostly because of the increase of $\overline{V_c}$.

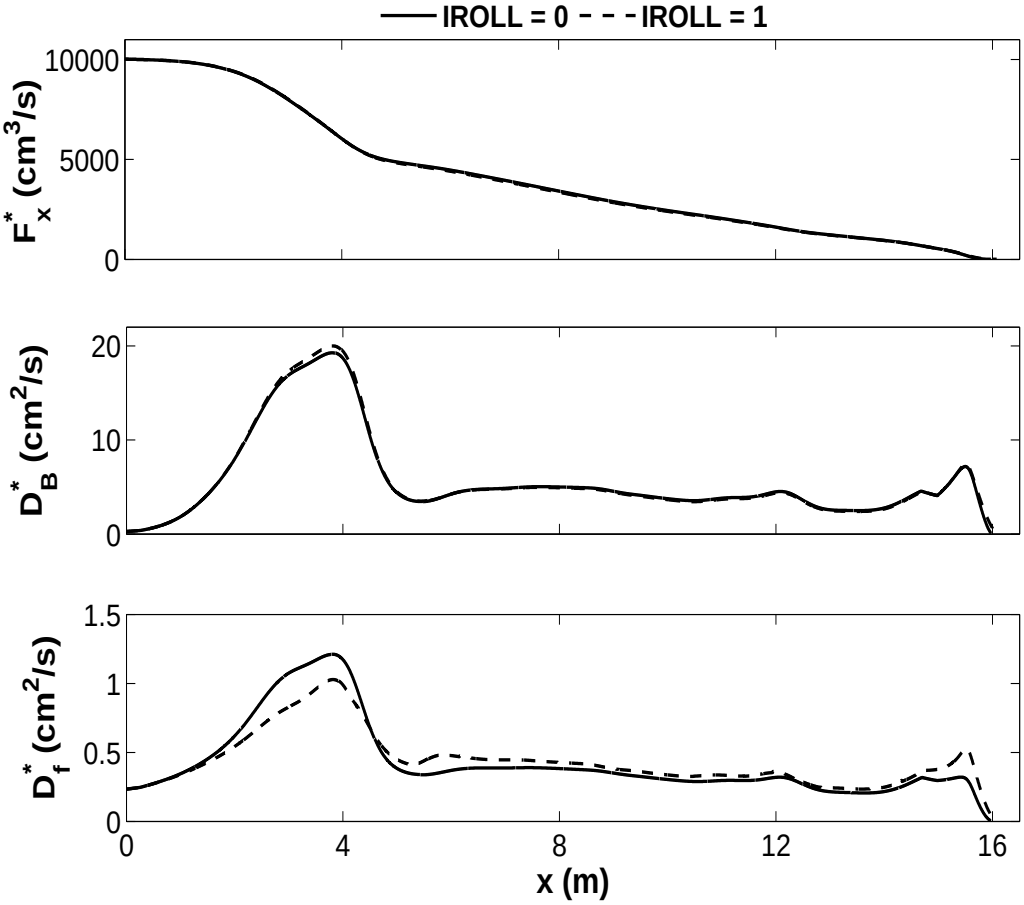

Figure 4.38: Computed cross-shore energy flux $F_x = \rho g F_x^*$, and energy dissipation rates $D_B = \rho g D_B^*$ and $D_f = \rho g D_f^*$ due to wave breaking and bottom friction for plunging wave test.

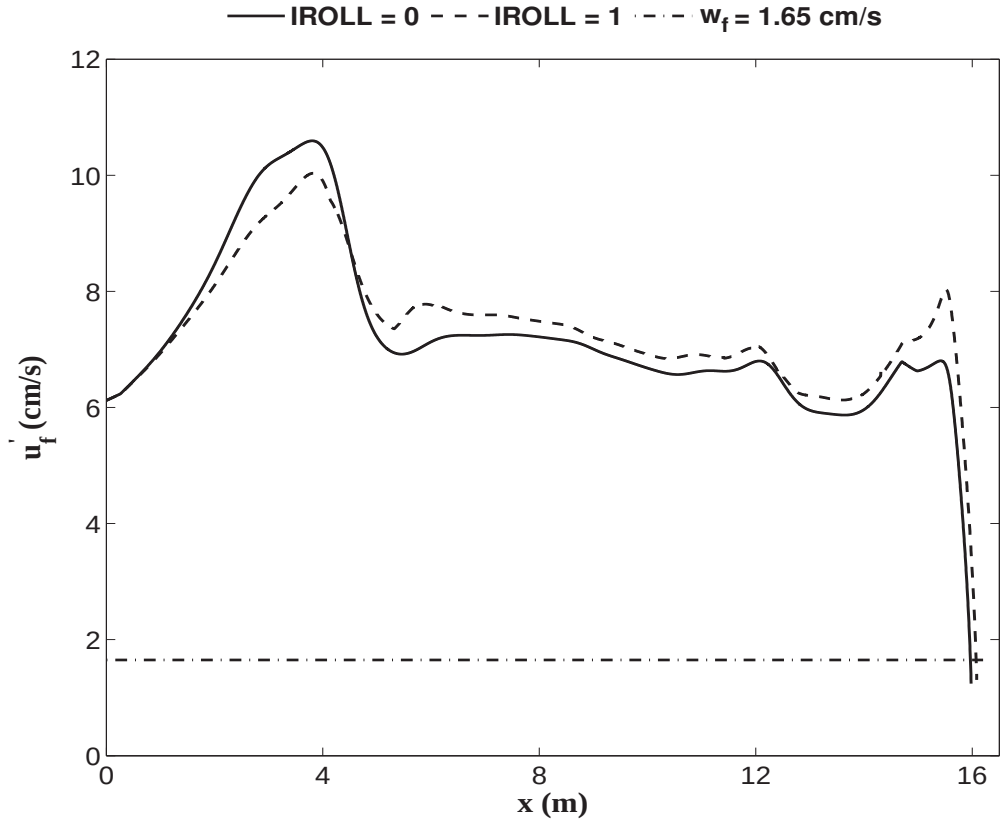

Figure 4.39: Computed turbulent velocity u'_f and estimated sediment fall velocity w_f for plunging wave test.

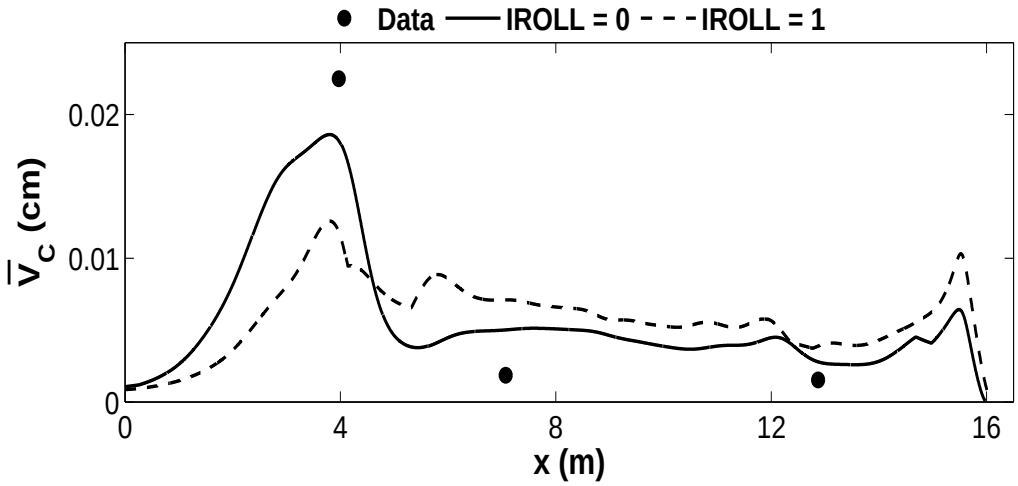

Figure 4.40: Measured and computed suspended sediment volume $\overline{V_c}$ per unit horizontal area for plunging wave test.

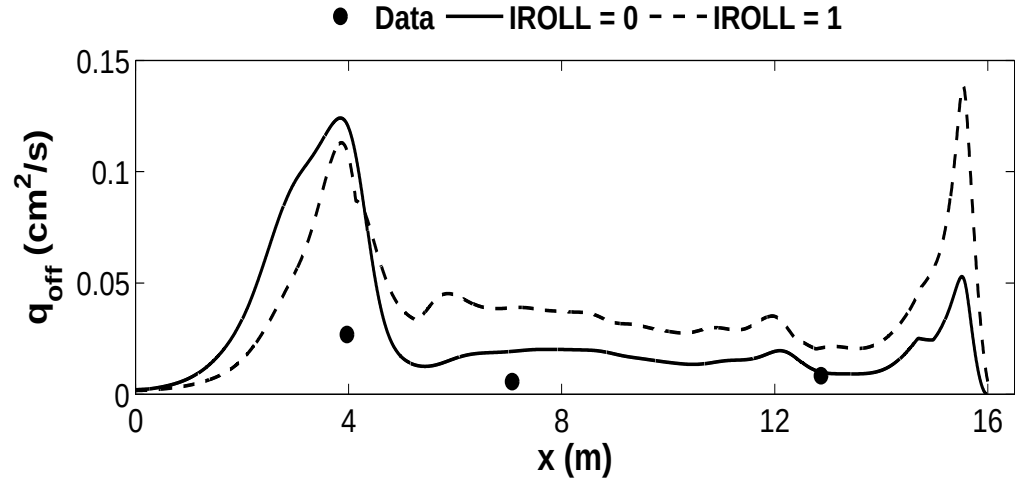

Figure 4.41: Measured and computed offshore suspended sediment transport rate q_{off} due to offshore current for plunging wave test.

Chapter 5

LONGSHORE SUSPENDED SEDIMENT TRANSPORT RATE

Figs. 5.1 and 5.2 compare the measured and computed longshore transport rates for the spilling and plunging wave tests. The measured longshore suspended sediment transport rate $q_{\ell s}$ given by Eq. 4.11 is obtained by integrating $(\bar{v}\bar{c})$ analytically from $z_m = z_a = 1$ cm to $z_m = \bar{h}$ using the fitted profiles of $\bar{v}$ and $\bar{c}$ in Eqs. (4.2) and (4.6) respectively. The measured longshore sediment transport rate $q_{\ell t}$ is obtained from the volume of sediment without any void collected in each of 20 downdrift bottom traps. Wang et al. (2002a) explained the difference between $q_{\ell s}$ and $q_{\ell t}$ because $q_{\ell t}$ was expected to be larger than $q_{\ell s}$ which does not include the transport rate within 1 cm from the bed. The computed suspended sediment transport rate q_s is simply estimated as $q_s = \overline{V}\ \overline{V_c}$ using the computed longshore current $\overline{V}$ and suspended sediment volume $\overline{V_c}$ per unit area. Figs. 5.1 and 5.2 show the computed q_s for IROLL = 0 and 1. IROLL = 1 yield better agreement mainly because of the better agreement for $\overline{V}$ shown in Figs. 4.23 and 4.36. The computed q_s using an approximate expression of $\overline{V_c}$ is discussed below. The time-averaged model cannot predict the transport rate in the upper swash zone unlike the time dependent model by Karambas and Karathanassi (2004).

The measured $q_{\ell t}$ and the computed q_s are integrated with respect to x to obtain the total transport rates $Q_{\ell t}$ and Q_s listed in Table 5.1.

Table 5.1: Total Sediment Transport Rates $Q_{\ell t}$ and Q_s for Spilling and Plunging Wave Tests

Breaker	Q_s (cm^3/s)		$Q_{\ell t}$
	IROLL = 0	IROLL = 1	(cm^3/s)
Spilling	56	56	51
Plunging	146	131	127

This numerical model predicts only the suspended sediment transport rate in the entire water column. Bed load might be neglected because the estimated turbulent velocity u'_f near the bed is significantly larger than the sediment fall velocity as shown in Figs. 4.26 and 4.39. The difference between Q_s and $Q_{\ell t}$ in Table 5.1 is less than about 10% even for IROLL = 0 which overpredicts q_s in the outer surf zone but underpredicts q_s in the inner surf zone. Wang et al. (2002b) compared the measured $Q_{\ell t}$ with existing formulas including the CERC formula. The agreement was not as good as that in Table 5.1 partly because e_B is calibrated here to obtain reasonable agreement for $\overline{V_c}$ in Figs. 4.27 and 4.40

Since Eq. (2.42) is fairly empirical and contains two empirical parameters, $(e_B D_r + e_f D_f) = e_c(D_r + D_f)$ is assumed where e_c = combined suspension efficiency which is taken as $e_c = (e_B + 0.001) = 0.003$ to account for the reduction of $e_f = 0.01$ to e_c. This approximation allows one to relate $\overline{V_c}$ to the combined energy equation which is the sum of the wave energy equation in Eq. (2.3) and the roller energy equation (2.11).

$$\frac{d}{dx}\left(F_x + \rho\, C_p^2\, q_r\, \cos\theta\right) = -e_c^{-1}\, \rho g(s-1) w_f \overline{V_c} \tag{5.1}$$

The left hand side of Eq. (5.1) can be shown to be the same as $d(S_{xy}/\alpha)/dx$ using Eqs. (2.5) and (2.7)–(2.10). Using the longshore momentum equation Eq. (2.2), Eq. (5.1) yields

$$\overline{V_c} = \frac{e_c \tau_{by}}{\alpha \rho g (s-1) w_f} \tag{5.2}$$

with

$$\tau_{by} = \frac{1}{2}\rho f_b \sigma_T \overline{V} \left[1.16^2 + \left(\frac{\overline{V}}{\sigma_T} \right)^2 \right]^{0.5} \tag{5.3}$$

where $\alpha = \sin\theta / C_p$ is constant due to Snell's law. Eqs. (5.2) and (5.3) explains the similarity of the cross-shore variation patterns of τ_{by} and $\overline{V_c}$ in Figs. 4.21 and 4.27 as well as in Figs. 4.34 and 4.40. Eq. (2.25) for τ_{by} combined with Eq. (2.34) is presented in Eq. (5.3) to show that τ_{by} is approximately proportional to the longshore current $\overline{V}$. Consequently, the longshore transport rate $q_s = \overline{V}\ \overline{V_c}$ is approximately proportional to the square of $\overline{V}$. The approximate computed q_s in Figs. 5.1 and 5.2 is based on $\overline{V_c}$ in Eq. (5.2) with $e_c = 0.003$. The agreement is similar for $\overline{V_c}$ given by Eqs. (2.42) and (5.2). Eq. (5.2) is convenient because it involves only the hydrodynamic variables included in longshore current models.

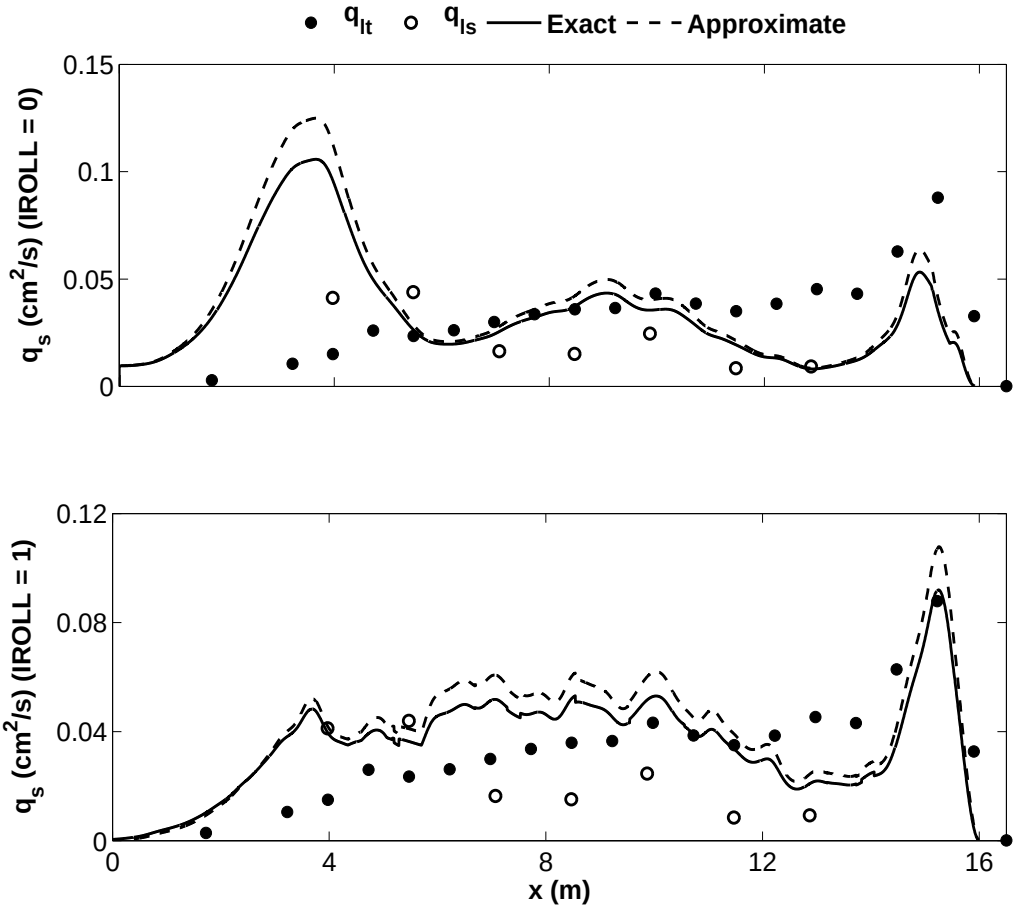

Figure 5.1: Computed and approximate suspended sediment transport rate q_s in comparison with measured longshore suspended ($q_{\ell s}$) and trapped ($q_{\ell t}$) sediment transport rates for IROLL = 0 (top) and 1 (bottom) for spilling wave test.

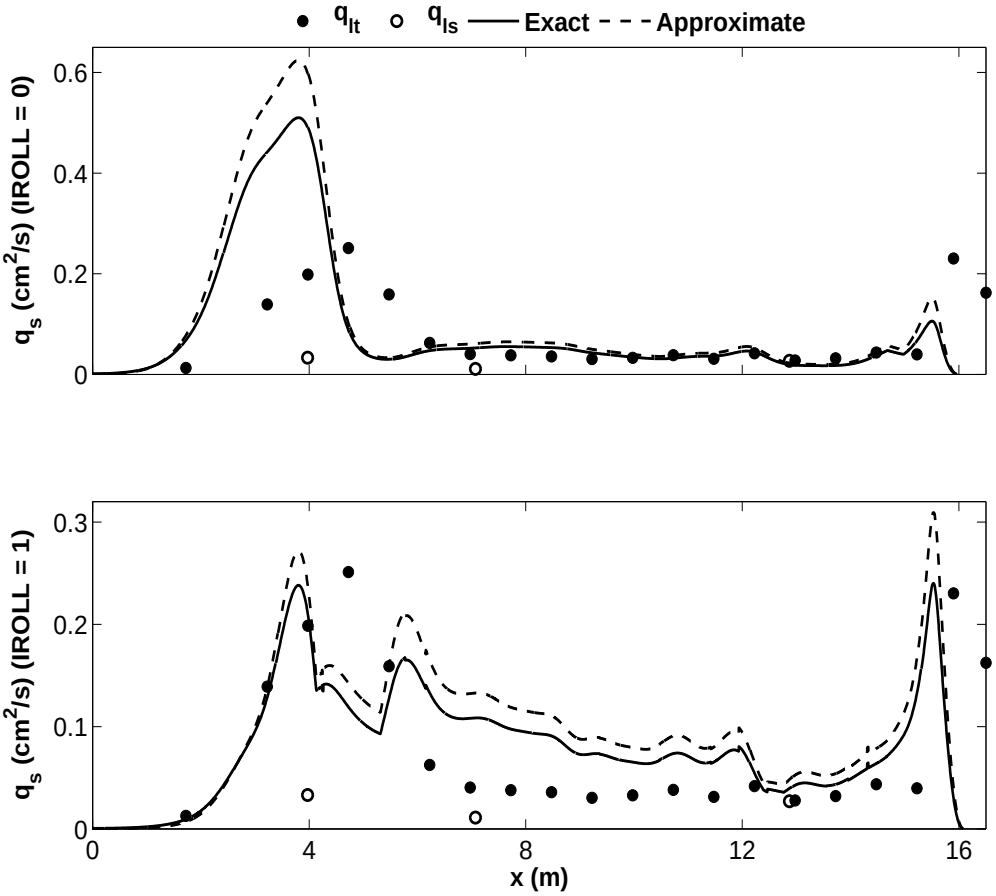

Figure 5.2: Computed and approximate suspended sediment transport rate q_s in comparison with measured longshore suspended ($q_{\ell s}$) and trapped ($q_{\ell t}$) sediment transport rates for IROLL = 0 (top) and 1 (bottom) for plunging wave test.

Chapter 6

CONCLUSIONS

A time-averaged model is developed for the prediction of longshore current and sediment transport on a sand beach of alongshore uniformity under unidirectional irregular breaking waves. The numerical model is based on the time-averaged continuity, cross-shore momentum, longshore momentum and energy equations coupled with the local use of linear shallow-water wave theory and the formula for local sediment suspension due to wave energy dissipation. The model predicts the cross-shore variations of the mean and standard deviation of the free surface elevation and depth-averaged cross-shore and longshore velocities as well as the time-averaged suspended sediment volume per unit horizontal area. These variables can be predicted from outside the surf zone to the lower swash zone.

The developed model is compared with limited field data and the comprehensive laboratory tests by Wang et al. (2002a, 2002b). The calibrated numerical model is in fair agreement with the data except that the time-averaged model cannot predict low frequency waves, shear waves, irregular wave runup and bed load. The breaker ratio parameter γ, the bottom friction factor f_b and the suspension efficiency e_B or e_c are calibrated for the cross-shore variations of the wave height, longshore current and suspended sediment volume, respectively. The calibrated range of these parameters are within a factor of about two. The model will need to be compared with other available laboratory and field data. The computational efficiency of this time-averaged model will facilitate extensive comparisons and calibrations of the empirical parameters.

The formula given by Eq. (5.3) for the suspended sediment volume indicates that the longshore sediment transport rate is approximately proportional to the square of the longshore current. This implies that an accurate longshore current model is required to predict the longshore sediment transport rate accurately. Longshore currents can be predicted fairly accurately now (Ruessink et al. 2001). As a result, the cross-shore variations of longshore sediment transport rates on various beaches may become predictable within a factor of about two. Empirical formulas for the total longshore sediment transport rate require the wave conditions at the breaker line which are generally computed using a wave propagation model for given offshore wave conditions. In the future, such a wave propagation model can be coupled with the present time-averaged model to extend the computation up to the lower swash zone and improve our capabilities in designing shoreline erosion mitigation measures.

REFERENCES

Baquerizo, A., Losada, M.A., Smith, J.M., and Kobayashi, N. (1997). "Cross-shore variation of wave reflection from beaches." *J. Waterw., Port, Coastal, Ocean Eng.*, 123(5), 274–279.

Battjes, J.A., and Janssen, J.P.F.M. (1978). "Energy loss and set-up due to breaking of random waves." *Proc., 16th Coastal Eng. Conf.*, ASCE. New York, N.Y., 1, 569–587.

Battjes, J.A., and Stive, M.J.F. (1985). "Calibration and verification of a dissipation model for random breaking waves." *J. Geophys. Res.*, 90(C5), 9159–9167.

Bodge, K.R., and Dean, R.G. (1987). "Short-term impoundment of longshore transport." *Proc. Coast. Sediments'87*, ASCE, Reston, Va., 139–155.

Coastal Engineering Manual. (2002). Part III: Coastal Sediment Processes, Coastal and Hydraulics Lab., US Army Engineer Research and Development Center, Vicksburg, Miss.

Cox, D.T., Kobayashi, N., and Kriebel, D.L. (1994). "Numerical model verification using SUPERTANK data in surf and swash zones." *Proc., Coast. Dynamics '94*, ASCE, New York, N.Y., 248–262

Cox, D.T., Kobayashi, N., and Wurjanto. A. (1991). "Computer Program for Spectral and Time-Series Analyses for Random Waves." *Research Rep. No. CACR-91-06*, Center for Applied Coastal Research, Univ. of Delaware, Newark, Del.

Dally, W.R., (1992). "Random breaking waves: Field verification of a wave-by-wave algorithm for engineering application." *Coast. Eng.*, 16, 369-397.

Feddersen, F., Guza, R.T., Elgar, S., and Herbers, T.H.C. (2000). "Velocity moments in alongshore bottom stress parameterizations." *J. Geophys. Res.*, 105(C4), 8673–8686.

Johnson, B.D., and Smith, J.M. (2005). "Longshore current forcing by irregular waves." *J. Geophys. Res.*, 110, C06006, doi:1029/2004JC002336

Kamphuis, J.W. (2002). "Alongshore transport rate of sand." *Coastal Engineering 2002*, Proc. 28th Coastal Engineering Conf., ASCE, Reston, Va., 2478–2490.

Karambas, T.V., and Karathanassi, E.K. (2004). "Longshore sediment transport by nonlinear waves and currents." *J. Waterw., Port, Coastal and Ocean Eng.*, 130(6), 277–286.

Kobayashi, N., DeSilva, G.S., and Watson, K.D. (1989). "Wave transformation and swash oscillation on gentle and steep slopes." *J. Geophys. Res.*, 94(C1), 951–966

Kobayashi, N., Herrman, M.N., Johnson, B.D., and Orzech, M.D. (1998). "Probability distribution of surface elevation in surf and swash zones." *J. Waterw., Port, Coastal, Ocean Eng.*, 124(3), 99–107.

Kobayashi, N., and Johnson, B.D. (1998). "Computer program CSHORE for predicting cross-shore transformation of irregular breaking waves." *Research Rep. No. CACR-98-04*, Center for Applied Coastal Research, Univ. of Delaware, Newark, Del.

Kobayashi, N., and Johnson, B.D. (2001). "Sand suspension, storage, advection, and settling in surf and swash zones." *J. Geophys. Res.*, 106(C5), 9363–9376.

Kobayashi, N., and Karjadi, E.A. (1996). "Obliquely incident irregular waves in surf and swash zones." *J. Geophys. Res.*, 101(C3), 6527–6542.

Kobayashi, N., and Wurjanto, A. (1992). "Irregular wave setup and run-up on beaches." *J. Waterw., Port, Coastal, Ocean Eng.*, ASCE, 118(4), 368–386.

Kobayashi, N., Zhao, H., and Tega, Y. (2005). "Suspended sand transport in surf zones." *J. Geophys. Res.* (in press).

Miller, H.C. (1999). "Field measurements of longshore sediment transport during storms." *Coastal Eng.*, 36, 301–321.

Noyes, T.J., Guza, R.T., Feddersen, F., Elgar, S., and Herbers, T.H.C. (2005). "Model-data comparisons of shear waves in the nearshore." *J. Geophys. Res.*, 110, C05019, doi:10.1029/2004JC002541.

Press, W.H., Flannery, B.P., Teukolsky, S.A., and Vetterling, W.T. (1989). *Numerical Recipes*, Cambridge Univ. Press, Cambridge, UK.

Raubenheimer, B., and Guza, R.T. (1996). "Observations and predictions of run-up." *J. Geophys. Res.*, 101(C10), 25575–25587.

Raubenheimer, B., Guza, R.T., Elgar, S., and Kobayashi, N. (1995). "Swash on a gently sloping beach." *J. Geophys. Res.*, 100(C5), 8751–8760.

Reniers, A.J.H.M., and Battjes, J.A. (1997). "A laboratory study of longshore currents over barred and non-barred beaches." *Coastal Eng.*, 30, 1–21.

Ruessink, B.G., Miles, J.R., Feddersen, F., Guza, R.T., and Elgar, S. (2001). "Modeling the alongshore current on barred beaches." *J. Geophys. Res.*, 106(C10), 22,451–22463.

Svendsen, I.A. (1984). "Wave heights and set-up in a surf zone." *Coastal Eng.*, 8, 303–329.

Thornton, E.B., and Guza, R.T. (1983). "Transformation of wave height distribution." *J. Geophys. Res.*, 88(C10), 5925–5938.

Thornton, E.B., and Guza, R.T. (1986). "Surf zone longshore currents and random waves: Field data and models." *J. Phys. Oceanogr.*, 16, 1165–1178.

van Rijn, L.C. (2002). "Longshore sand transport." *Coastal Engineering 2002*, Proc. 28th Coastal Engineering Conf., ASCE, Reston, Va., 2439–2451.

Wang, P. (1998). "Longshore sediment flux in water column and across surf zone." *J. Waterw., Port, Coastal, Ocean Eng.*, 124(3), 108–117.

Wang, P., Ebersole, B.A., Smith, E.R., and Johnson, B.D. (2002a). "Temporal and spatial variations of surf-zone currents and suspended sediment concentration." *Coastal Eng.*, 46, 175–211.

Wang, P., Smith, E.R., and Ebersole, B.A. (2002b). "Large-scale laboratory measurements of longshore sediment transport under spilling and plunging breakers." *J. Coastal Res.*, 18(1), 118–135.